MEDICAL ULTRASOUND ABERRATION CORRECTION VIA ACOUSTIC DROPLET VAPORIZATION AND TIME-REVERSAL ACOUSTICS

by

Kevin Joseph Haworth

A dissertation submitted in partial fulfillment
of the requirements for the degree of
Doctor of Philosophy
(Applied Physics)
in The University of Michigan
2009

Doctoral Committee:

Research Assistant Professor Oliver D. Kripfgans, Co-Chair
Professor Paul L. Carson, Co-Chair
Professor David R. Dowling
Professor J. Brian Fowlkes
Professor Jonathan M. Rubin

Research is what I'm doing when I don't know what I am doing.

Wernher Von Braun (1912-1977)

Dedicated to all those who have given their time as my teachers,

most especially my first teachers, Mom and Dad,

and for the one who continues to teach me about the joys of life everyday, Tricia.

ACKNOWLEDGMENTS

Anytime you spend over a fifth of your life working on something, it's likely that you have had some help along the way. That is certainly true of my doctoral dissertation work. It has been a labor (of mostly) love and a privilege to have the opportunity. Financially, I would like to acknowledge the Applied Physics Program and the Rackham Graduate School at the University of Michigan and the National Institutes of Health. It was through their funding that I have been able to carry out this work.

Directly concerning the work in this dissertation, I am most indebted to my advisor, Herr Doktor Professor Oliver D. Kripfgans. We have spent countless hours together discussing and carrying out the science presented within the following pages. Through that process I have gained an immense amount of knowledge. More than that however, Dr. Kripfgans has been a well-spring of support. He has pushed me when I have needed pushing and encouraged me when things looked down. It is a great honor to be his first doctoral son (as they say in German).

I have also gained a great deal from my co-advisor, Dr. Paul Carson. I have never met anyone who could come up new ideas so quickly and easily. He has been a source of inspiration and solid advice. In addition to Dr. Carson, I would like to thank Dr. Brian Fowlkes, whom I consider an unofficial advisor. He has been a wonderful example of leadership in the chaos of academia and can truly be described as a gentleman and scholar. Together, Drs. Kripfgans, Carson, and Fowlkes have made my work possible and formed me into the scientist that I am today. I would also like to acknowledge my other committee members, Dr. Jonathan Rubin, an MD

who is better at math than most PhDs, and Dr. David Dowling, who guided me on my first formal study of time-reversal acoustics.

There are many other individuals within the Basic Radiological Sciences Division, where I have worked for the past 5 years, who deserve mention. Drs. Jerry LeCarpentier, Michael Richards, Man Zhang, and Scott Swanson have all been an important part of my experience for both scientific, social, and philosophical discussions. My labmates, Dr. Andrea Lo and candidate Mario Fabiilli have been wonderful people to work with on a day-to-day basis. I have really appreciated the fun times we have spent in the lab working (or playing!). Dr. Tim Hall has been a wonderful sounding board for ideas and a great guide for the 'mental' phases of completing a doctorate. Sharon Karahan and Carol Cribbins have provided wonderful administrative support. I would also like to thank all of the other professors, post-docs, and graduate students that I've worked with in BRS.

My applied physics family also deserves acknowledgement. Dr. Brad Orr, Cynthia McNabb, and Charles Sutton have made me feel welcome ever since I first visited Michigan prior to enrolling. Cyndi and Charles really do feel like a mother and brother. There are many applied physics students who I have shared time with, but I would like to especially thank my classmates, Brenton Knuffman, Malavika Chandra, Eric Harding, Arthur McClelland, and Erik Kim. I spent most of my waking hours with them during my first year in graduate school and they have made it a wonderful experience. I am excited to see all that they will accomplish and look forward to many more years of friendship.

I would also like to acknowledge several friendships I continue to benefit from, my neighbors, the Hills and the Ryans, Tom Lee, Brad Susala, and all those I have taught confirmation classes with at St. Mary Student Parish, especially Sr. Dorothy Ederer and Fr. Tom McClain.

Finally, I would like to thank my entire family. They have been a fount of joy

and happiness. Most especially, I would like to thank my mom and dad, Karen and Bill. Everything I have achieved has been with their love and support, which means the world to me. I truly would not be the person I am today without them. Lastly, I would like to thank my wife-to-be, Tricia. She has stood by my side though all the ups and downs, and I can only hope that I can be as good to her as she has been to me.

Ann Arbor, Michigan

February, 2009

TABLE OF CONTENTS

LIST OF FIGURES

Figure

LIST OF APPENDICES

LIST OF ACRONYMS

ADV	acoustic droplet vaporization
SA	synthetic aperture
TRA	time-reversal acoustics
DORT	french acronym for decomposition of the time-reversal operator
TRCC	time-reversal chaotic cavity
IC	inertial cavitation
US	ultrasound
MRI	magnetic resonance imaging
SNR	signal-to-noise ratio
CV	coefficient of variance
SVD	singular value decomposition
IR	impulse response

LIST OF SYMBOLS

f	frequency
c	speed of sound
λ	wavelength
f #	transducer or array f-number
K	bulk modulus
$K(t)$	propagation matrix
ρ	density (chapter I) or correlation coefficient (chapter IV)
σ	standard deviation
α	exponential decay constant
$g(t)$	input function
$h(t)$	impulse response
$W(t)$	window function
Δt	width of window function
t_{on}	time window function begins being non-zero
t_{off}	time window function ends being non-zero
$r(t)$	time-reversal focused signal
$\otimes$	convolution operator

ABSTRACT

MEDICAL ULTRASOUND ABERRATION CORRECTION VIA ACOUSTIC DROPLET VAPORIZATION AND TIME-REVERSAL ACOUSTICS

by

Kevin Joseph Haworth

Co-Chairs: Oliver D. Kripfgans and Paul L. Carson

Time-reversal acoustics (TRA) is an alternative to standard focusing approaches in medical ultrasound. TRA records backscattered ultrasound and time-reverses it ($\psi(t) \rightarrow \psi(-t)$). Due to the time-reversal invariance of the lossless wave equation, a transmitted time-reversed signal will focus back to the scattering source. It has been proposed that acoustic droplet vaporization (ADV) can be used to generate point-scatterers for TRA focusing. ADV is a process where micron-sized liquid droplets are phase-transitioned into gas bubbles via an acoustic wave. The feasibility of performing medical ultrasound aberration correction using TRA and ADV is explored in three different contexts.

The first is transcranial transmit aberration correction. It is demonstrated that stable gas-bubbles can be produced transcranially. Additionally, it is demonstrated that time-reversal focusing can be used to correct for transcranial aberrations with a gas bubble. Aberration correction was performed using a synthetic aperture

approach. Under the conditions described, time-reversal aberration correction resulted in a linear gain of 1.9 ± 0.3. This demonstration is particularly relevant for therapeutic applications.

The second context is aberration correction on receive. A synthetic aperture algorithm is implemented with the decomposition of the time-reversal operator algorithm. It is shown that this combination can produce aberration corrected images with a clinically relevant ultrasound unit. Aberration is induced electronically to mimic a near-field aberrator. Various dependences on imaging parameters and reconstruction are explored. This demonstration is particularly relevant for diagnostic applications.

The third context is the development of a theoretical shot noise model to statistically describe the output of a multiple-scattering time-reversal experiment using arbitrary inputs and windowing. It is found that the largest noise contribution depends on the windowing and can occur at times outside the main lobe. A common set of parameters is applied to the general result and it is seen that as the duration of the input function increases, the signal-to-noise ratio (SNR) decreases (independent of signal bandwidth). It is also seen that longer persisting impulse responses result in increased main lobe amplitudes and SNR.

CHAPTER I

Introduction

As the title of this dissertation suggests, the focus of this work is the advancement of the use of time-reversal acoustics (TRA) and acoustic droplet vaporization (ADV) for aberration correction of medically relevant ultrasound (i.e. pressure waves in a frequency ranging from $10^5 - 10^8$ Hz). In the course of this description, three key terms are present that form the core of what is to follow and thus require careful definition and background. Those terms are aberration correction (in the context of medical ultrasound), time-reversal acoustics, and acoustic droplet vaporization. This introductory chapter will define these terms and their relevance.

1.1 Aberration Correction

1.1.1 Origin of Aberrations

In order to define aberration correction, it is first appropriate to begin with the definition of an aberration. An aberration is a perturbation of a substance or process from its assumed state. In standard medical ultrasound, the substance refers to the amplitude and phase modulations that define a propagating ultrasound wave (i.e. pressure wave). The assumed state is propagation in a homogeneous and isotropic medium where the Born approximation is valid. For this type of medium, the sourceless, lossless wave equation in a homogeneous and isotropic medium can be

used to describe the wave propagation [1]:

$$\frac{\partial^2 \psi(\vec{x},t)}{\partial t^2} - \left(\frac{K}{\rho}\right)^2 \nabla^2 \psi(\vec{x},t) = 0, \tag{1.1}$$

where $\psi(\vec{x},t)$ describes the pressure fluctuations about equilibrium, K and ρ are the bulk modulus and density of the medium, respectively. The wave velocity (also commonly referred to as the speed of sound) is given by $c = \sqrt{K/\rho}$. This equation makes it possible (and reasonable) to determine how to focus ultrasonic waves to a location in the body. The ability to focus ultrasound is critical to both diagnostic and therapeutic ultrasound. Thus an aberration, for the purposes of this dissertation, is a deviation from wave propagation according to equation 1.1, which then results in improper focusing. For medical ultrasound, there are three main sources of aberration: variations in the speed of sound of the material, attenuation, and multiple scattering from heterogeneities.

For many medical ultrasound applications, the medium being investigated is soft tissue which has a nominal speed of sound of 1540 ± 60 m/s [2]. This corresponds to an 8% variation in the speed of sound. For standard diagnostic beamforming, images are created by assuming a uniform speed of sound to determine how to focus the ultrasound to a particular location and to convert the received temporal data to spatial data to form an image. When the speed of sound varies, the acoustic beam is no longer focused properly and amplitudes at the desired locations will decrease and possibly increase at other locations. As a result, the backscatter received will contain less signal scattered from the desired location and more signal scattered from unintended locations. Upon reception, temporal data is then incorrectly assigned to a spatial location. In combination, this leads to contrast degradation and image artifacts. In cases where the speed of sound changes unevenly across broad areas (such as transmission through layers of uneven fat), it is possible for the variations in speed of sound to lead to refraction of the beam. This again will cause temporal

data to be incorrectly assigned to a spatial location.

Attenuation also leads to image degradation in multiple ways. First, attenuation in tissue is frequency dependent, higher frequencies are attenuated more rapidly than lower frequencies. As a result, the center frequency of a received signal decreases as it corresponds to deeper echos. This then increases the axial point-spread-function. In more extreme cases, such as focusing through the chest wall, the bone may completely attenuate parts of the signal, while diffracting/refracting other parts. This effectively reduces the aperture of the array, decreasing lateral resolution. Additionally, if the attenuation is very high, the signal corresponding to deeper portions of an image may fall into the noise making imaging impossible. Conversely, if the attenuation of a local object is very low (such as a cyst) tissue behind it will be enhanced.

Multiple scattering can create problems similar to those from variations in the speed of sound. For standard diagnostic imaging, it is assumed that the Born approximation holds (i.e. no multiple scattering). When this is not the case, signals that scatter multiple times will take longer to return to the array. Since they arrive later, it is assumed that they come from tissue that is deeper in the image than is true. As an example, strong scatterers can create mirror artifacts where aspects of an image will appear on both sides of the scatter. Finally, refraction and specular reflectors can cause whole areas of an image to be assigned to an incorrect spatial location.

1.1.2 Overview of Aberration Correction

The need for aberration correction can be seen by the extensive number of research publications on the topic. More specifically however, several studies have been performed outlining the degradation of the focal spot size and image quality under a variety of aberrations. Anderson *et al.* found that changes of $\pm 8\%$ in the speed of sound, reduced the peak echo amplitude of a wire scatterer embedded in tissue

mimicking material by 10.5 dB and increased the lateral beam width by up to 320% [3]. Computer simulations by Chen and Zagzebski confirmed the importance of sound speed errors in soft tissue mimicking materials and also found that to a lesser degree frequency dependent attenuation can broaden the lateral beam resolution [4]. More recently there has been a sharp increase in the amount of research being performed with transcranial ultrasound as a method of thermally ablating tumors [5] and opening the blood-brain barrier [6]. With the speed of sound in skull bone varying from 2000 to 4000 m/s [2], aberration correction is an essential part of any effective transcranial therapy.

The sheer number of publications concerning ultrasonic aberration correction is also a testament to the large number of algorithms and methods that can be envisioned [7–20]. Key points to note when assessing a particular technique is (1) whether the scheme corrects for pulse shape/frequency aberrations or if it only corrects time-shift aberrations, (2) whether the method is invasive, (3) whether the algorithm can correct distributed aberrations, and (4) whether the algorithm can be applied on transmit, receive, or both. Corrections on transmit focus the ultrasound more cleanly at the region-of-interest; minimizing side lobe interaction with off-axis scatterers and the width of the main lobe. Corrections on receive align wavefronts so that images can be formed more accurately and precisely. For therapeutic purposes, correction on transmit-only is tolerable. However, for diagnostic imaging and image-guided therapy, it is necessary for the correction to be performed in both directions. With this in mind, it is possible to broadly categorize aberration correction approaches based on their methodology and application.

Probably the most commonly used class of aberration correction methods is adaptive time-delay compensation. Maximum speckle brightness [7], time-shift compensation using back-propagation [8], and signal correlation [9] are all examples of this class. They all assume that the aberrations are well-described by a near-field

phase screen (i.e. time-delay). These algorithms compute estimates for the time-delay in the near-field of each transducer element. Then upon transmission and reception from that element, the signal is appropriately time-shifted. This class of algorithms is popular because the algorithms tend to be relatively simple to compute and implement, particularly for receive signals. However this class fails when the aberrations can no longer be well-described by a near-field phase screen.

A second related class of algorithms is multimodality aberration correction. Here the medium of interest is imaged using another modality such as x-ray computed tomography (CT) [10–12]. The CT image parameters are correlated to acoustic parameters. Wave propagation models are then used to determine what aberrations are induced and how to compensate for them. This method has been successful in correcting aberrations due to the skull. However it requires significant computation time and registration between the two modalities.

A third class of aberration correction algorithms is optimization of image parameters. This class of algorithms works by estimating and minimizing image artifacts. The parallel adaptive receive compensation algorithm [13; 14] and algorithms using a generalized coherence factor [15] are examples. These algorithms consist of post-processing data that has already been received and is therefore adequate for diagnostic purposes, but not for therapeutics. A final class of algorithms is based on time-reversal acoustics and will be discussed in more detail in the following section.

1.2 Time-Reversal Acoustics

Looking back at eqn. 1.1, if $\psi(\vec{x},t)$ is a solution, then $\psi(\vec{x},-t)$ is also a solution. This is the time-reversal invariance of the wave equation. A basic time-reversal experiment consists of a signal transmitted into a medium that scatters offof objects of interest. The scattered signal is recorded by the array, time-reversed and

retransmitted. Due to time-reversal invariance, the retransmitted waves refocus on the scattered objects. If a dominant point-scatterer is present, then the time-reversed signal will predominately focus on the point-scatterer and minimal energy will be transmitted to other locations.

Figure 1.1 shows this process explicitly applied to aberration correction. Suppose a set of transducers are arranged on an arc and all of the transducers are equidistant from a point-scatterer (note that this geometry is not required in general). If one of the transducers sends out a short pulse that scatters off the point-scatterer, all other transducers receive the signal at the same time. Conversely, if all but one of the transducers transmits a pulse at the same time, all of the signals would scatter off of the point target simultaneously and interfere constructively. A signal the same shape as the transmit signal would be recorded at the receive transducer (figure 1.1a). Now imagine placing a time-delay aberrator between the transducers and the point-scatterer (in practice the aberrator may be more complex). This is shown in figure 1.1 as a gray semicircle. Now when all of the transducers transmit, the aberrator will delay each signal differently and they will no longer interfere constructively. The signal received on the receive transducer will be smaller and will not have the shape of the transmit pulses (figure 1.1b). This process describes how standard diagnostic imaging is performed and how it suffers with simple aberrators. Now imagine again the first case where only one transducer transmits a pulse. The signal will scatter off of the point-scatterer and be received at each transducer at a different time (figure 1.1c). If these signals are time-reversed, the delays in the signals, obtained by time-reversal, will be exactly the delays needed to compensate for the aberrator time-delays. Upon transmission, the signals will all arrive at the point-scatterer in-phase and interfere constructively. The signal received by the receive transducer will be an amplified version of the pulses transmitted (figure 1.1d).

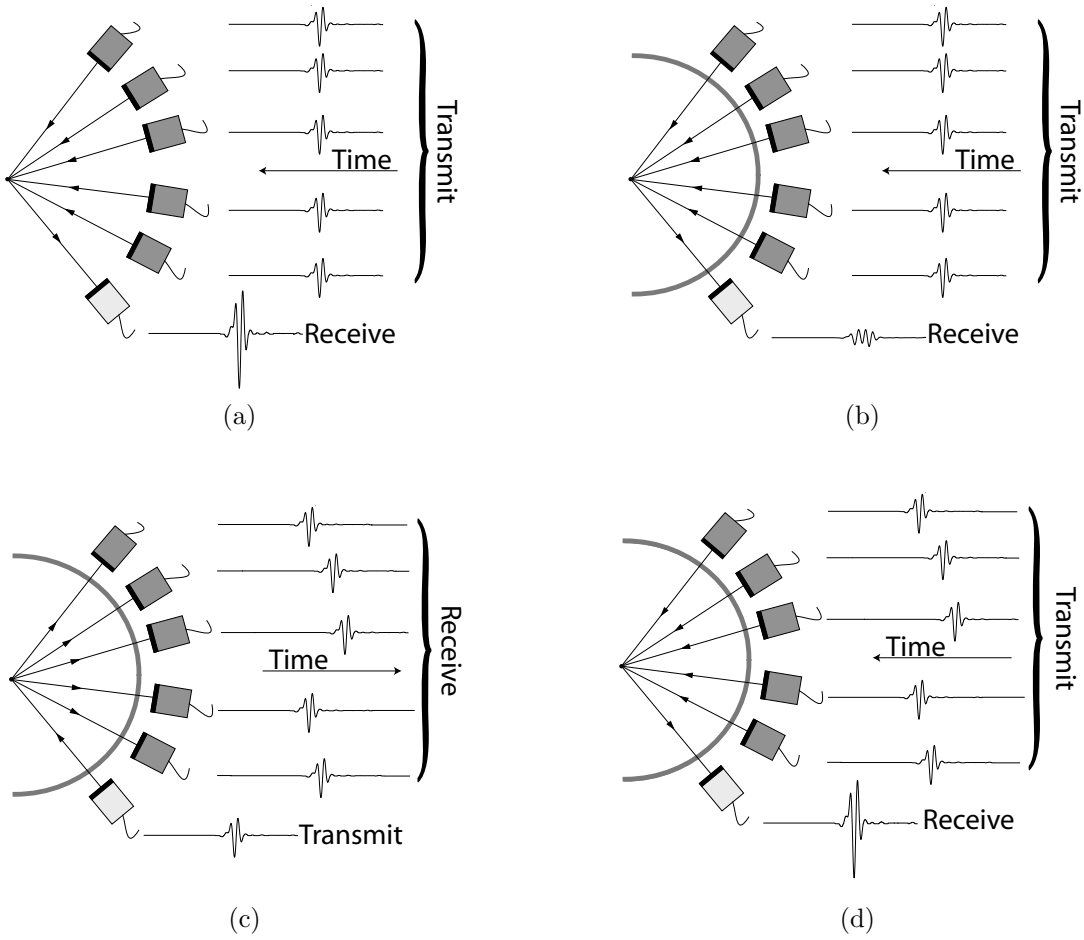

Figure 1.1: (a) Standard spherical focusing without any aberrtor results in constructive interference at the focus. (b) Standard spherical focusing in the presence of an aberrator results in signals that do not interfere constructively, resulting in a distorted signal on reception. (c) The first step in time-reversal focusing is to transmit a single pulse (bottom receiver) and record the scattered and aberrated waveforms (top receivers). Aberrations are shown as time-delays, though in practice the aberrations may be more complex. (d) The second step in time-reversal focusing is to transmit the time-reversed versions of the aberrated waveforms from each transducers. Due to time-reversal invariance, the time-reversed waveforms will directly compensate for the aberrator and the signals will interfere constructively, resulting in a undistorted signal.

1.2.1 Array-Based Time-Reversal

The first experiments involving time-reversal acoustics were performed in the early 1960s and involved a single source and a single receiver [21]. Later, the development of array-based time-reversal techniques were reported independently in both ultrasonics [16–18] and underwater acoustics [19]. Traditional time-reversal provides a robust method of focusing acoustic energy on a remote acoustic source without *a priori* knowledge of the source location, the array location, or the acoustic medium between them, as illustrated in figure 1.1. In addition, it produces optimum focusing in the presence of noise. While ambient noise unrelated to the static environment (e.g. electronic noise and not speckle) can degrade the time-reversal focusing, it has been shown that time-reversal acoustics is robust enough to still work successfully [22; 23]. For traditional time-reversal, an array of transducers receives an acoustic signal from a remote source, time-reverses it, and then broadcasts the time-reversed signal back into the acoustic environment. It has been shown that the environment must be at least moderately static (if the frequency of the environmental changes is $1/\Delta t$ then the experiment must be carried out in$\Delta\ t/2$) [24]. While traditional time-reversal is fairly robust, it does not provide any information about the location of the source nor any instructions for how to steer the focus to a new nearby spatial location.

One of the most robust methods for focusing on individual scatterers is DORT and related methods [20]. DORT is the French acronym for decomposition of the time-reversal operator (Décomposition de l'opérateur de retournement temporel). The idealized version of this method requires the reflectors to be point targets and to be well-resolved from each other, based on the diffraction limited focal spot size of the array. Here, an impulse is broadcast from a single element of the array and the backscattered signal is recorded by all of the array's elements (fig. 1.2a, assuming a seven element array). This process is repeated on the next element (fig. 1.2b) and

each subsequent element in the array until each element of the array has been used as a source. For n elements, there are now $n \times n$ signals, which can be viewed as a three-dimensional matrix (fig. 1.2c) where time is the third dimension. This matrix is often called the propagation matrix $K(t)$. The matrix is Fourier transformed (fig. 1.2d) and then multiplied by its Hermitian conjugate. The resulting matrix is called the time-reversal operator. The eigenvectors of the time-reversal operator (each which is a function of time) correspond to the element-by-element waveforms necessary to focus on each scatterer individually. The eigenvalues correspond to the relative backscatter amplitude of each scatterer based on its location in the medium and acoustic beam pattern. The eigenvectors and eigenvalues can be found using singular value decomposition (SVD).

If the acoustic inhomogeneities are modeled as a thin random-phase screen located a known distance from the transducer array, the focusing achieved with the DORT method can be manipulated to focus in a zone surrounding the point target using calculated Green's functions [25]. The calculated Green's function for focusing at a specific location near a point target is obtained by first estimating the distance between the array and the phase-screen. Then the measured Green's function at the array is computationally backpropagated from the transducer array to the phase screen (while assuming the medium between the array and phase-screen is known and homogenous). The signal computed at the phase screen via backpropagation is time-shifted to account for the aberration. Then it is geometrically steered (i.e. a spherical delay law is applied) to focus at the specific location near the original scatterer. The steered waveform is then forward-propagated from the phase-screen back to the transducer array. The resulting signal at the array is the calculated Green's function for focusing at the specific, desired location near the point target. Note, that the technique assumes that the distance from the actual point target location to the phase-screen and the calculated Green's function location to the

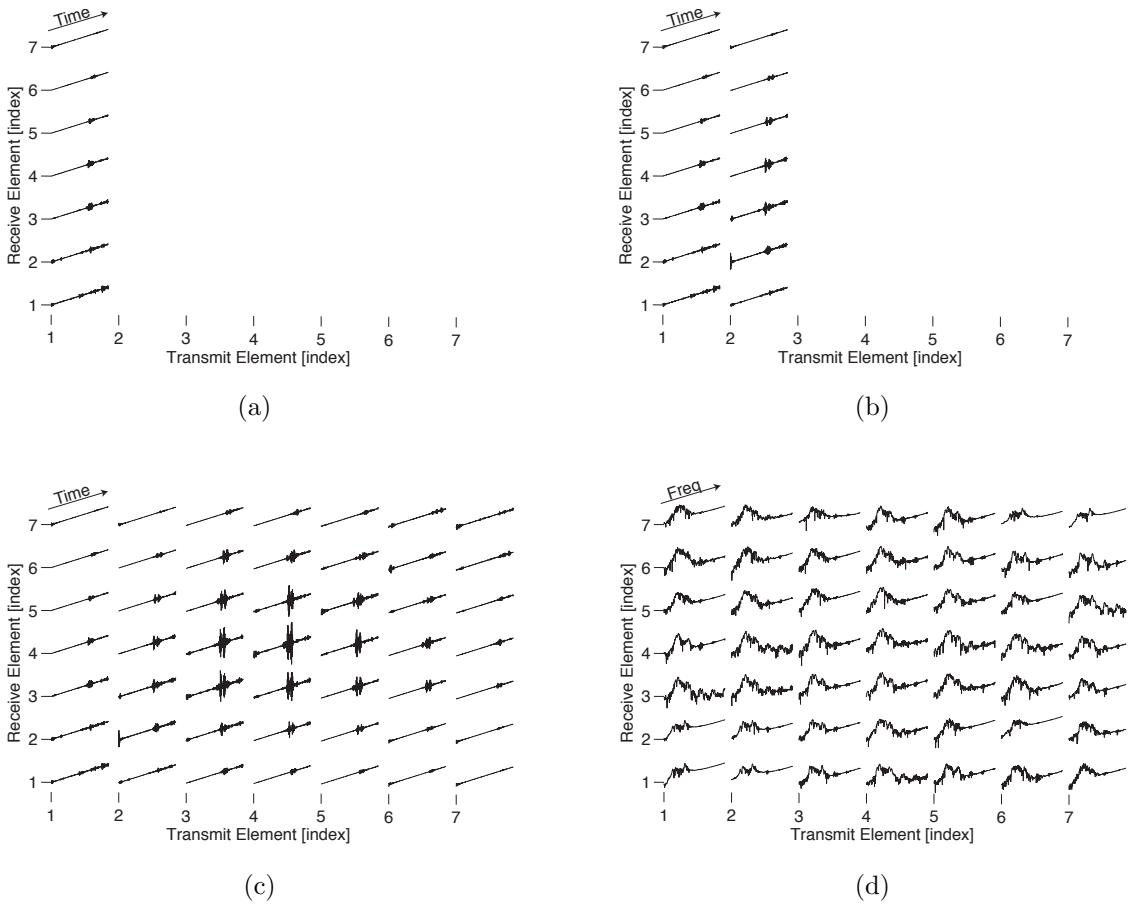

Figure 1.2: Demonstration of building a propagation matrix for a seven element array. (a) A pulse is transmitted from the first element of the array and the backscatter is recorded by all of the elements in the array. (b) This process is repeated for the next element. (c) The process continues until all of the elements have fired and the three-dimensional propagation matrix is built. (d) Each signal is Fourier transformed and all subsequent work performed in the frequency domain.

phase screen is assumed to be the same. When this assumption breaks down (i.e. moving beyond the isoplanatic patch), an accurately calculated Green's function is not obtainable.

1.2.2 Cavity-Based Time-Reversal

The requirements on element-size and spacing for array-based time-reversal focusing is the same as for standard ultrasound focusing. Thus, for medically relevant diagnostic linear arrays, 64 or more elements are needed. For 1.75D arrays that allow for modest elevational focusing and full 2D arrays that allow for 3D focusing throughout a volume, thousands of elements are needed. Since time-reversal focusing requires individually programable transmits, the hardware and software requirements to build time-reversal arrays is substantial. The desire to find a less expensive solution has led to the development of time-reversal chaotic cavities (TRCCs).

TRCCs were first introduced by Fink and colleagues [26–28]. Typical TRCC experiments work by having a transducer transmit an acoustic/elastic pulse into a solid (typically a metal). The sound reverberates within the cavity, reflecting offof the solid's walls. The acoustic signal at any point within the cavity quickly becomes a diffuse wave. If the diffuse wave is recorded, time-reversed, and retransmitted, the waves will approximately retrace their paths and focus at the transducer that originally transmitted the pulse. The diffuse wave is chaotic in origin and unique (to first-order) to each location in the cavity. The initial experiments by Draeger and Fink measured elastic waves in a 2D silicon wafer. Quieffin *et al.*[29] showed that this concept could be extended to 3D solids and more importantly that if the solid were put into contact with a water bath, signal would leak out of the solid and could be recorded with a hydrophone in the water. Then using spatial reciprocity, they showed that if the signal recorded by the hydrophone was time-reversed and retransmitted by the original transducer on the cavity, a pulse would focus on the hydrophone's location outside of the cavity. The location of the hydrophone could be

varied and thus it was found that TRCCs allowed focusing throughout a 3D volume with as few as one ultrasound transducer. Additional work by Fink and colleagues has led to prototypes for imaging devices [30] and high amplitude ultrasound therapy devices [31], among other applications. Since the initial development of TRCCs, Sarvazyan and colleagues have also made significant progress in understanding and utilizing TRCCs [32–34].

1.3 Acoustic Droplet Vaporization

When describing time-reversal acoustics, reflection off of a point-scatterer was often referred to. In the human body however, there are very few, if any, natural point-scatterers. In 1998, the late Dr. Robert Apfel posited that small microbubbles could be created in the body by phase-transitioning a superheated liquid droplet using ultrasound, a process termed acoustic droplet vaporization (ADV). He additionally proposed that these microbubbles can be used as point-scatterers (among other uses) [35]. Shortly after this, Kripfgans *et al.* demonstrated that it was possible to experimentally create micro-droplet emulsions that could be phase-transitioned into microbubbles using medically relevant ultrasound [36]. The micro-droplets are composed of a surfactant shell (typically either albumin or lipid) stabilizing a superheated perfluorocarbon. Typically dodecafluoropentane is the perfluorocarbon used because it has a boiling point of 29°C, which makes it possible to work with it as a liquid at room temperature, but is superheated as a liquid at body temperature (37°C). A detailed procedure for forming droplets can be found in [37]. Since 1998, significant work has been put into understanding and developing applications for ADV. Table 1.1 lists this published work.

To date, work has been published on four applications of ADV, aberration correction, occlusion therapy, drug delivery, and bubble-enhanced thermal high-intensity focused ultrasound therapy (HIFU). Discussion of ADV and aberration

Table 1.1: Published work on ADV and its application.

Citation	**Synopsis**
Apfel 1998 [35]	Initial proposal of ADV
Kripfgans *et al.* 2000 [36]	Initial demonstration and study of ADV
Kripfgans *et al.* 2002 [38]	*In vivo* demonstration of occlusion and creation of point targets
Giesecke and Hynynen 2003 [39]	US parameter and droplet composition effects on vaporization
Kripfgans *et al.* 2004 [40]	ADV mechanism
Psychoudakis *et al.* 2004 [41]	Theoretical study of ADV bubbles as point-scatterers
Kripfgans *et al.* 2005 [42]	*In vivo* renal rabbit occlusion
Kawabata *et al.* 2005 [43]	Droplet composition effects on vaporization
Lo *et al.* 2006 [44]	Impact of ADV bubbles on acoustic fields
Lo *et al.* 2007 [45]	Acoustic parameter and ultrasound contrast agent effect on vaporization
Fang *et al.* 2007 [46]	Drug delivery
Haworth *et al.* 2008 [47]	Transcranial aberration correction
Zhang *et al.* 2008 [48]	Selective renal tissue occlusion
Zhang and Porter 2008 [49]	HIFU enhancement
Kawabata *et al.* 2008 [50]	HIFU enhancement
Haworth *et al.* 2008 [51]	Initial Growth and Coalescence of ADV bubbles
Wong *et al.* 2008 [52]	Bubble growth evolution
Haworth *et al.* 2008 [53]	Monitoring ADV tissue occlusion
Fabiilli *et al.* 2009 [37]	Mechanism and relationship to inertial cavitation

correction is the focus of chapters II and III. Both drug delivery and bubble-enhanced thermal therapies are relatively new and indicate that both applications may be feasible pending more extensive and detailed studies. Bubble occlusion therapy is the most extensively studied application of ADV. Kripfgans *et al.* initially demonstrated that ADV could be performed *in vivo* and it was possible to achieve partial occlusions in canine brain tissue [38]. This was followed up by a second study where flow reductions of externalized rabbit renal tissue could be induced by vaporizing droplets in the left ventricle [42]. Perfusion reductions of greater than

90% were achieved and maintained at greater than 60% for more than one hour. More recently, studies in externalized large animal (canine) kidneys have shown highly-transient, but complete, flow reductions using intra-arterial injections. More modest efficiency has been observed for intravenous injections and transcutaneous vaporization [48].

1.4 Overview of Dissertation

The following chapters of this dissertation will delve more deeply into the possibilities of using TRA and ADV to perform aberration correction. In particular, two chapters will discuss the use of array-based TRA in conjunction with ADV to perform aberration correction. A third chapter will focus on the ability of cavity-based (and more generally, high-order multiple-scattering) TRA to focus arbitrary waveforms (such as long pulses or coded-signals). A fourth chapter will discuss a variety of supplemental results that provide additional motivation and support for the previous chapters. Finally, the work will be summarized and directions for possible future work will be addressed. Each chapter will contain an introductory section to provide the necessary background material such that the chapter can be read independently of the rest of the dissertation. A more detailed outline of the dissertation is given below.

Chapter II provides proof-of-principle for transcranial transmit aberration correction via TRA and ADV. Low-frequency (512 kHz) ADV is demonstrated transcranially. This indicates the feasibility of creating point targets through the skull. Separately, it is shown that using a synthetic aperture setup it is possible to realign waveforms aberrated by an *ex vivo* skull using time-reversal acoustics and the echo off of a single bubble. This work was published in the journal 'Ultrasound in Medicine and Biology' [47].

Chapter III compliments chapter II by demonstrating receive aberration

correction. Initially, a synthetic aperture imaging algorithm is implemented and studied. Then an aberration correction algorithm based on time-reversal acoustics is described and implemented to create aberration corrected images. Aberrations are induced electronically.

Chapter IV provides the background and develops an extension of the shot noise model for multiple-scattering time-reversal acoustics developed by Derode *et al.* [54]. Their model statistically predicts the signal and noise levels of a time-reversal focused signal when the system is initially excited with an impulse. Here, the basic model is extended to allow for arbitrary input functions. This work provides insight into the feasibility of using long and/or coded signals (as would be necessary for acoustic radiation force work or coded-excitations). This work has been accepted for publication in the 'Journal of the Acoustical Society of America' [55].

Chapter V describes a variety of additional experiments that have been performed to provide support and motivation for the previous chapters. This includes experimental results of focusing with TRCCs and high-speed camera images of droplet vaporization. Appropriate citations for this work are Haworth and Kripfgans [51], Haworth *et al.* [53], and Haworth *et al.* [56].

Chapter VI provides a summary of the results contained in the previous chapter and discusses ideas for future work.

REFERENCES

[1] T. L. Szabo, *Diagnostic Ultrasound Imaging: Inside Out*. Academic Press Series in Biomedical Engineering, 200 Wheeler Road, 6th Floor, Burlington, MA 01803, USA: Elsevier Academic Press, 1 ed., 2004.

[2] F. A. Duck, *Physical Properties of Tissue: A Comprehensive Reference Book*. Academic Press Limited, 24-28 Oval Road, London NW1 7DX: Academic Press Inc., 1990.

[3] M. E. Anderson, M. S. McKeag, and G. E. Trahey, "The impact of sound speed errors on medical ultrasound imaging," *Journal of the Acoustical Society of America*, vol. 107, pp. 3540–3548, June 2000.

[4] Q. Chen and J. A. Zagsebski, "Simulation study of effects of speed of sound and attenuation on ultrasound lateral resolution," *Ultrasound in Medicine and Biology*, vol. 30, pp. 1297–1306, July 2004.

[5] M. Pernot, J.-F. Aubry, M. Tanter, A.-L. Boch, F. Marquet, M. Kujas, D. Seilhean, and M. Fink, "*In vivo* transcranial brain surgery with an ultrasonic time reversal mirror," *Journal of Neurosurgery*, vol. 106, pp. 1061–1066, June 2007.

[6] N. Vykhodtseva, N. McDannold, and K. Hynynen, "Progress and problems in the application of focused ultrasound for blood-brain barrier disruption," *Ultrasonics*, vol. 48, pp. 279–296, 2008.

[7] L. Nock and G. E. Trahey, "Phase aberration correction in medical ultrasound using speckle brightness as a quality factor," *Journal of the Acoustical Society of America*, vol. 85, no. 5, pp. 1819–1833, 1989.

[8] D. L. Liu and R. C. Waag, "Correction of ultrasonic wavefront distortion using backpropagation and a reference waveform method for time-shift compensation," *Journal of the Acoustical Society of America*, vol. 96, no. 2, pp. 649–660, 1994.

[9] S. Flax and M. O'Donnell, "Phase-aberration correction using signals from point reflectors and diffuse scatterers: Basic principles," *IEEE Transactions on Ultrasonics, Ferroelectrics, and Frequency Control*, vol. 35, no. 6, pp. 758–767, 1988.

[10] G. T. Clement and K. Hynynen, "A non-invasive method for focusing ultrasound through the human skull," *Physics in Medicine and Biology*, vol. 47, pp. 1219–1236, April 2002.

[11] J. F. Aubry, M. Tanter, M. Pernot, J. L. .Thomas, and M. Fink, "Experimental demonstration of noninvasive transskull adaptive focusing based on prior computed tomography scans," *Journal of the Acoustical Society of America*, vol. 113, pp. 84–93, January 2003.

[12] K. Hynynen, N. McDannold, G. T. Clement, F. A. Jolesz, E. Zadicario, R. Killiany, T. Moore, and D. Rosen, "Pre-clinical testing of a phased array ultrasound system for MRI-guided noninvasive surgery of the brain - a primate study," *European Journal of Radiology*, vol. 59, pp. 149–156, 2006.

[13] S. Krishnan and M. O'Donnell, "Transmit aperture processing for nonlinear contrast agent imaging," *Ultrasonic Imaging*, vol. 18, pp. 77–105, 1996.

[14] S. Krishnan, K. W. Rigby, and M. O'Donnell, "Efficient parallel adaptive aberration correction," *IEEE Transactions on Ultrasonics, Ferroelectrics, and Frequency Control*, vol. 45, no. 3, pp. 691–703, 1998.

[15] P. C. Li and M. L. Li, "Adaptive imaging using the generalized coherence factor," *IEEE Transactions on Ultrasonics, Ferroelectrics, and Frequency Control*, vol. 50, no. 2, pp. 128–141, 2003.

[16] M. Fink, C. Prada, F. Wu, and D. Cassereau, "Self focusing with time reversal mirror in inhomogeneous media," *IEEE Ultrasonics Symposium*, vol. 2, pp. 681–686, 1989.

[17] M. Nikoonahad and T. L. Pusateri, "Ultrasonic phase conjugation," *Journal of Applied Physics*, vol. 66, no. 1, pp. 4512–4513, 1989.

[18] O. Ikeda, "An image reconstruction algorithm using phase conjugation for diffraction-limited imaging in an inhomogeneous medium," *Journal of the Acoustical Society of America*, vol. 85, pp. 1602–1606, 1989.

[19] D. R. Jackson and D. R. Dowling, "Phase conjugation in underwater acoustics," *Journal of the Acoustical Society of America*, vol. 89, pp. 171–181, January 1991.

[20] C. Prada, S. Manneville, D. Spoliansky, and M. Fink, "Decomposition of the time reversal operator: Detection and selective focusing on two scatterers," *Journal of the Acoustical Society of America*, vol. 99, pp. 2067–2076, April 1996.

[21] A. Parvulescu and C. S. Clay, "Reproducibility of signal transmissions in the ocean," *The Radio and Electronic Engineer*, vol. 29, pp. 223–228, April 1965.

[22] S. R. Khosla and D. R. Dowling, "Time-reversing array retrofocusing in noisy environments," *Journal of the Acoustical Society of America*, vol. 109, no. 2, pp. 538–546, 2001.

[23] K. G. Sabra, S. R. Khosla, and D. R. Dowling, "Broadband time-reversing array retrofocusing in noisy environments," *Journal of the Acoustical Society of America*, vol. 111, no. 2, pp. 823–830, 2002.

[24] S. R. Khosla and D. R. Dowling, "Time-reversing array retrofocusing in simple dynamic underwater environments," *Journal of the Acoustical Society of America*, vol. 104, no. 6, pp. 3339–3350, 1998.

[25] M. Fink and C. Dorme, "Aberration correction in ultrasonic medical imaging with time-reversal techniques," *International Journal of Imaging Systems and Technology*, vol. 8, no. 1, pp. 10–25, 1997.

[26] C. Draeger and M. Fink, "One-channel time reversal of elastic waves in a chaotic 2D-silicon cavity," *Physical Review Letters*, vol. 79, pp. 407–410, July 1997.

[27] C. Draeger and M. Fink, "One channel time-reversal in chaotic cavities: Theoretical limits," *Journal of the Acoustical Society of America*, vol. 105, pp. 611–617, February 1999.

[28] C. Draeger, J.-C. Aime, and M. Fink, "One-channel time-reversal in chaotic cavities: Experimental results," *Journal of the Acoustical Society of America*, vol. 105, pp. 618–625, February 1999.

[29] N. Quieffin, S. Catheline, R. K. Ing, and M. Fink, "Real-time focusing using an ultrasonic one channel time-reversal mirror coupled to a solid cavity," *Journal of the Acoustical Society of America*, vol. 115, pp. 1955–1960, May 2004.

[30] G. Montaldo, N. Perez, C. Negreira, and M. Fink, "The spatial focusing of a leaky time reversal chaotic cavity," *Waves in Random and Complex Media*, vol. 17, pp. 67–83, February 2007.

[31] G. Montaldo, P. Roux, A. Derode, C. Negreira, and M. Fink, "Ultrasound shock wave generator with one-bit time reversal in a dispersive medium, application to lithotripsy," *Applied Physics Letters*, vol. 80, pp. 897–899, February 2002.

[32] A. Y. Sutin, E. Roides, and A. P. Sarvazyan, "Damage detection in composites using the time-reversal acoustics method," *Journal of the Acoustical Society of America*, vol. 116, p. 2567, October 2004.

[33] Y. D. Sinelnikov, A. Y. Sutin, and A. P. Sarvazyan, "Time-reversal acoustic focusing with liquid resonator for medical applications," *6th International Symposium on Therapeutic Ultrasound*, vol. 911, pp. 82–86, 2006.

[34] L. Fillinger, A. Y. Sutin, and A. P. Sarvazyan, "Time reversal focusing of short pulses," *IEEE Ultrasonics Symposium*, pp. 220–223, October 2007.

[35] R. E. Apfel, "Activatable infusable dispersions containing drops of a superheated liquid for methods of therapy and diagnosis," Patent 5,840,276, Apfel Enterprises, Inc., November 1998.

[36] O. D. Kripfgans, J. B. Fowlkes, D. L. Miller, O. P. Eldevik, and P. L. Carson, "Acoustic droplet vaporization for therapeutic and diagnostic applications," *Ultrasound in Medicine and Biology*, vol. 26, no. 7, pp. 1177–1189, 2000.

[37] M. L. Fabilli, K. J. Haworth, N. H. Fakhri, O. D. Kripfgans, P. L. Carson, and J. B. Fowlkes, "The role of inertial cavitation in acoustic droplet vaporization," *IEEE Transactions on Ultrasonics, Ferroelectrics, and Frequency Control*, vol. Accepted, 2009.

[38] O. D. Kripfgans, J. B. Fowlkes, M. Woydt, O. P. Eldevik, and P. L. Carson, "*In vivo* droplet vaporization for occlusion therapy and phase aberration correction," *IEEE Transactions on Ultrasonics, Ferroelectrics, and Frequency Control*, vol. 49, no. 2, pp. 726–738, 2002.

[39] T. Giesecke and K. Hynynen, "Ultrasound-mediated cavitation thresholds of liquid perfluorocarbon droplets *In Vitro*," *Ultrasound in Medicine and Biology*, vol. 29, no. 9, pp. 1359–1365, 2003.

[40] O. D. Kripfgans, M. L. Fabilli, P. L. Carson, and J. B. Fowlkes, "On the acoustic vaporization of micrometer-sized droplets," *Journal of the Acoustical Society of America*, vol. 116, pp. 272–281, July 2004.

[41] D. Psychoudakis, J. B. Fowlkes, J. L. Volakis, and P. L. Carson, "Potential of microbubbles for use as point targets in phase aberration correction," *IEEE Transactions on Ultrasonics, Ferroelectrics, and Frequency Control*, vol. 51, pp. 1639–1648, December 2004.

[42] O. D. Kripfgans, C. M. Orifici, P. L. Carson, K. A. Ives, O. P. Eldevik, and J. B. Fowlkes, "Acoustic droplet vaporization for temporal and spatial control of tissue occlusion: A kidney study," *IEEE Transactions on Ultrasonics, Ferroelectrics, and Frequency Control*, vol. 52, pp. 1101–1110, July 2005.

[43] K.-I. Kawabata, N. Sugita, H. Yoshikawa, T. Azuma, and S.-I. Umemura, "Nanoparticles with multiple perfluorocarbons for controllable ultrasonically induced phase shifting," *Japanese Journal of Applied Physics*, vol. 44, no. 6B, pp. 4548–4552, 2005.

[44] A. H. Lo, O. D. Kripfgans, P. L. Carson, and J. B. Fowlkes, "Spatial control of gas bubbles and their effects on acoustic fields," *Ultrasound in Medicine and Biology*, vol. 32, no. 1, pp. 95–106, 2006.

[45] A. H. Lo, O. D. Kripfgans, P. L. Carson, E. D. Rothman, and J. B. Fowlkes, "Acoustic droplet vaporization: Effects of pulse duration and contrast agent," *IEEE Transactions on Ultrasonics, Ferroelectrics, and Frequency Control*, vol. 54, pp. 933–946, May 2007.

[46] J.-Y. Fang, C.-F. Hung, M.-H. Liao, and C.-C. Chien, "A study of the formulation design of acoustically active lipospheres as carriers for drug

delivery," *European Journal of Pharmaceutics and Biopharmaceutics*, vol. 67, pp. 67–75, 2007.

[47] K. J. Haworth, J. B. Fowlkes, P. L. Carson, and O. D. Kripfgans, "Towards aberration correction of transcranial ultrasound using acoustic droplet vaporization," *Ultrasound in Medicine and Biology*, vol. 34, pp. 435–445, March 2008.

[48] M. Zhang, K. J. Haworth, J. B. Fowlkes, M. L. Fabilli, O. D. Kripfgans, W. W. Roberts, and P. L. Carson, "Superselective tissue occlusion by acoustic droplet vaporization (ADV)," *8th International Symposium on Therapeutic Ultrasound*, September 2008.

[49] P. Zhang and T. Porter, "Ultrasound-induced thermal lesion formation with phase shift emulsion," *8th International Symposium on Therapeutic Ultrasound*, September 2008.

[50] K.-I. Kawabata, R. Asami, T. Azuma, H. Yoshikawa, and S.-I. Umemura, "Cavitation assisted HIFU with phase-change nano droplet," *IEEE Ultrasonics Symposium*, vol. 1, 2008.

[51] K. J. Haworth and O. D. Kripfgans, "Initial growth and coalescence of acoustically vaporized perfluorocarbon microdroplets," *IEEE Ultrasonics Symposium*, vol. 1, 2008.

[52] Z. Z. Wong, O. D. Kripfgans, J. B. Fowlkes, and J. L. Bull, "Microbubble evolution due to acoustic droplet vaporization: Observation via ultra-high speed imaging," *61st Annual Meeting of the American Physical Society Division of Fluid Dynamics*, vol. 2008, 2008.

[53] K. J. Haworth, M. L. Fabilli, J. B. Fowlkes, M. Zhang, O. D. Kripfgans, W. W. Roberts, and P. L. Carson, "Mean echo power as a measure of flow reduction for bubble occlusion therapy," *IEEE Ultrasonics Symposium*, vol. 1, 2008.

[54] A. Derode, A. Tourin, and M. Fink, "Ultrasonic pulse compression with one-bit time reversal through multiple scattering," *Journal of Applied Physics*, vol. 85, pp. 6343–6352, May 1999.

[55] K. J. Haworth, J. B. Fowlkes, P. L. Carson, and O. D. Kripfgans, "Generalized shot noise model for time-reversal acoustics in multiple-scattering media," *Journal of the Acoustical Society of America*, Accepted.

[56] K. J. Haworth, O. D. Kripfgans, D. D. Steele, and S. D. Swanson, "Acoustically induced tissue displacement for shear wave elasticity imaging using MRI," *Journal of the Acoustical Society of America*, vol. 118, p. 1942, September 2005.

CHAPTER II

Transcranial Acoustic Droplet Vaporization and Transmit Aberration Correction

2.1 Introduction

Transcranial ultrasound imaging and therapy are severely limited by the aberration caused by the skull. Several noninvasive techniques have been proposed to correct for this aberration. Transcranial aberration correction techniques can be grouped into four broad categories. The first category uses relatively low transmit frequencies (circa 250 kHz) where the aberration effects are minimal [1]. This technique was demonstrated successfully, however the low frequency limited the resolution that could be achieved for imaging and also the heating that could be achieved for thermal therapy. The second grouping uses an alternative modality (magnetic resonance imaging (MRI) or x-ray computed tomography (CT)) to obtain information about the skull and uses this information to compute the expected aberrations. Hynynen *et al.* initially proposed that sufficient aberration correction could be obtained using the skull thickness, as measured by MRI, and a uniform speed of sound, based on the weighted average of the speed of sound in each of the 3 layers of the skull (outer layer, diploë, and inner layer) [2; 3]. This approach improved transcranial focusing, however, significant sidelobes were still present. It also suggested that significant improvement in correcting aberrations could be achieved by using different speeds of sound for the different bone densities within the skull. This led to the use of

CT instead of MRI due to its ability to measure both skull thickness and density. Clement and Hynynen [4] and Aubry *et al.* [5] both subsequently reported on the acoustic properties of skull bone based on CT imaging. Clement and Hynynen [6] took the next step to perform three-dimensional aberration correction through ten *ex vivo* human skulls based on the acoustic properties derived from CT images. Hynynen *et al.* [7] have pursued this work further, recently demonstrating the ability to transcranially produce lesions in primates. While this appears to be a very successful technique, it requires the use of a second (ionizing) modality and the accompanying registration between the modalities. A third technique has been proposed by Vignon *et al.* [8] that approximates transcranial aberration using two arrays placed on opposing sides of the skull (one on each of the parietal (or temporal) bones). All of the element-to-element responses are obtained between the two arrays to create propagation matrices. The matrices can then be manipulated to isolate the approximate effects of only one side of the skull. This technique suffers from the requirement of using two identical arrays on either side of the skull. This eliminates the ability to use a hemispherical array, which currently appears to be necessary to achieve therapeutic pressures in the brain without overheating the skull and skin [7].

The fourth noninvasive transcranial focusing approach is point-target based aberration correction. Several different point-target based algorithms have been proposed [9–11]. All point-target techniques rely on the existence of sparsely distributed point scatterers/point sources in the region of interest. For the vast majority of biomedical applications, there are few, if any (e.g. pineal gland, kidney or gall bladder stones), point-targets available. Recently, Pernot and others have demonstrated the feasibility of using ultrasound induced cavitation bubbles as point-targets [12; 13]. However, to achieve cavitation bubbles, non-diagnostic pressures must be reached, which may be difficult in a severely aberrating and attenuating medium. Additionally, cavitation bubbles are highly transient, making

it difficult to apply many of the proposed multistage focusing algorithms. While there may be some circumstances where transient point-targets are suitable and/or desirable, stable bubbles could be advantageous in several ways. In particular, stable bubbles that last for tens of seconds should allow for more robust and time-consuming point-target aberration correction algorithms, and they may also be used for subsequent therapy when produced in appropriate concentrations [14; 15].

In this chapter, an alternative means of achieving a point-target by using acoustic droplet vaporization (ADV) is presented. ADV is a technique whereby liquid droplets are phase transitioned into gas bubbles using an acoustic disturbance [16]. The liquid droplets employed and their manufacturing are described in detail elsewhere [17]. The droplets' core, dodecafluoropentane (DDFP) (CAS: 678-26-2, Strem Chemicals, Newburyport, MA, USA), has a bulk fluid boiling point of 29 °C, which is less than normal body temperature (37 °C). The DDFP droplet is stabilized in a superheated state by an albumin shell. *In vitro* studies have elucidated the values of parameters (such as pulse length, pulse amplitude, presence of nucleation sites) for controlling ADV [17–21]. Of these, it has also been found that the vaporization threshold decreases with increasing insonification frequency for short insonification pulses. It is also known that the unaberrated point-spread function's width decreases with increasing frequency, allowing for better localization of vaporization. These both indicate that high frequencies are more suitable. Unfortunately, transcranial aberration and attenuation increase with increasing insonification frequency. This will require a trade-off between minimizing aberration and minimizing the vaporization threshold and spot size. It has also been found that acoustic pressure amplitudes from some diagnostic ultrasound systems are sufficient to phase-transition an ADV droplet [14].

Preliminary animal studies have shown the *in vivo* applicability of ADV [14; 22]. Specifically, DDFP droplets have been vaporized at particular locations in the canine

brain after a standard bilateral craniotomy. The resulting isolated single ADV bubbles had a +23 dB backscatter relative to surrounding brain tissue. Additionally, numerical simulations have yielded an appropriate ratio for bubble-size to acoustic wavelength (i.e. *ka*-value) for spherical ADV bubbles to be considered point-targets [15]. These values depend on the array dimensions and orientation relative to the bubble. From these results, it was hypothesized that ADV bubbles could provide an *in situ* point-target for aberration correction.

Below, the ability to perform ADV transcranially at relatively low frequencies, where the aberrations are minimized, will be demonstrated. Additionally, it will be demonstrated that transmit aberration correction using a time-reversal focusing algorithm [11] and a single microbubble is possible. Focusing in this case should be associated with waveform alignment at the focus on transmit, rather than receive focusing for image formation.

2.2 Materials and Methods

2.2.1 Transcranial Insertion Loss

Prior work has shown that skull preparation affects the acoustic properties of an *ex vivo* human skull [23–25]. Therefore, prior to performing transcranial ADV and aberration correction, the effects of skull hydration and the gas content of the hydrating water on the ultrasound transmission were studied. An *ex vivo* human skull was obtained from, and experiments approved by, the Anatomical Donations Program within the University of Michigan Medical School. The skull, which was dry from storage in air, was placed in a water tank with gas-saturated water at 22±2 °C. A transcranial pulse-echo signal was measured as a function of hydration time using a 1 MHz, 3.8 cm diameter, unfocused Panametrics V392 immersion transducer (Olympus, Waltham, MA, USA). The echo was obtained off a 10.1 cm diameter, 2.7 cm thick brass plate, which acts as a reference reflector that is -0.6 dB

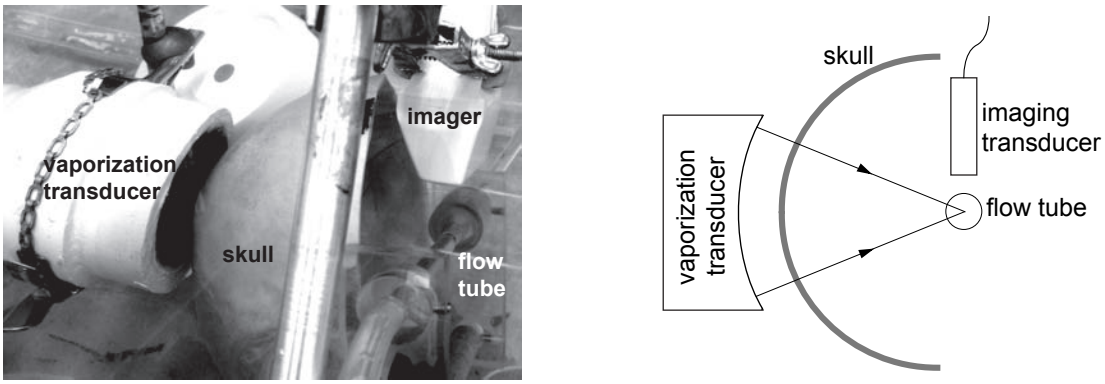

(a) (b)

Figure 2.1: (a) Photo and (b) schematic of the experimental setup used for transcranial acoustic droplet vaporization. The vaporization transducer can be seen to the left of the skull. A flow tube (right of the skull), carries the DDFP droplet-UCA-saline mixture. A linear array (top right) was used to observe ADV.

from a perfect reflector assuming an acoustic impedance of 40.6 MRayl [26]. After the fiftieth hour of hydration, degassing of the water was initiated. Degassing was performed using the multiple pinhole method described by Kaiser *et al.* [27].

2.2.2 Transcranial ADV

Figure 2.1 shows the setup used to perform transcranial ADV. The procedure for creating droplets for vaporization has been described by Kripfgans *et al.* [17]. Droplets were vaporized using a 550 kHz, 70 mm diameter, 100 mm focal-length, air-backed, lead zirconate titanate (PZT-4) transducer (Channel Industries, Santa Barbara, CA, USA). The vaporization pulse was a 1000 cycle, 550 kHz tone burst generated with an HP33120A function generator (Agilent, Palo Alto, CA, USA) and amplified using an ENI A-300 power amplifier (Rochester, NY, USA). The long pulse length was chosen to lower the vaporization threshold as demonstrated by Giesecke and Hynynen [19] and Lo *et al.* [20]. A cellulose flow tube (Spectra/Por 8 mm flat width, Spectrum Laboratories Inc., Rancho Dominguez, CA, USA) oriented 45° relative to the direction of gravity was filled with saline (0.9% Sodium Chloride Irrigation, USP, Abbott Laboratories, North Chicago, IL, USA) and 50×10^3 DDFP

droplets per mL of saline. Additionally, 600×10^3 ultrasound contrast agent (UCA) microspheres (Definity, DuPont Pharmaceuticals Company, Billerica, MA, USA) per mL of saline were added to further reduce the vaporization threshold [20]. Note that a standard dose of Definity results in approximately 2×10^6 UCA bubbles per mL of blood. The flow tube was part of a closed system (with a trap for vaporized ADV bubbles, which have a much greater buoyancy than UCA bubbles) with the saline, UCA, and DDFP droplets being continuously recirculated from a reservoir used for stirring the fluid at room temperature (22±2 °C). A 10 MHz linear array connected to a Diasonics VST Master Series clinical ultrasound scanner (GE Medical Systems, Milwaukee, WI, USA) was placed perpendicular to the axial direction of the vaporization transducer and parallel to the flow tube to acoustically observe the creation of ADV bubbles with B-mode images. The lowest transmit power was used to prevent the 10 MHz array from vaporizing DDFP droplets, and this was verified by a lack of echogenicity in B-mode images. An *ex vivo* human skull was placed between the vaporization transducer and flow tube. The particular orientation through the parietal bone of the skull was chosen to mimic the projected orientation that would be used in future *in vivo* work.

2.2.3 Single Bubble Production and Detection

Following the demonstration of transcranial ADV, single bubbles are created and detected for later use in performing aberration correction. The bubbles were created using the following setup, which was different than the transcranial ADV setup to ensure that only a single bubble was present.

Bubble Production

Two different methods of producing and isolating single bubbles were employed. To keep the bubbles from moving, cellulose dialysis tubing (Spectra/Por 14.6 mm flat width, Spectrum Laboratories Inc., Rancho Dominguez, CA, USA) was filled with

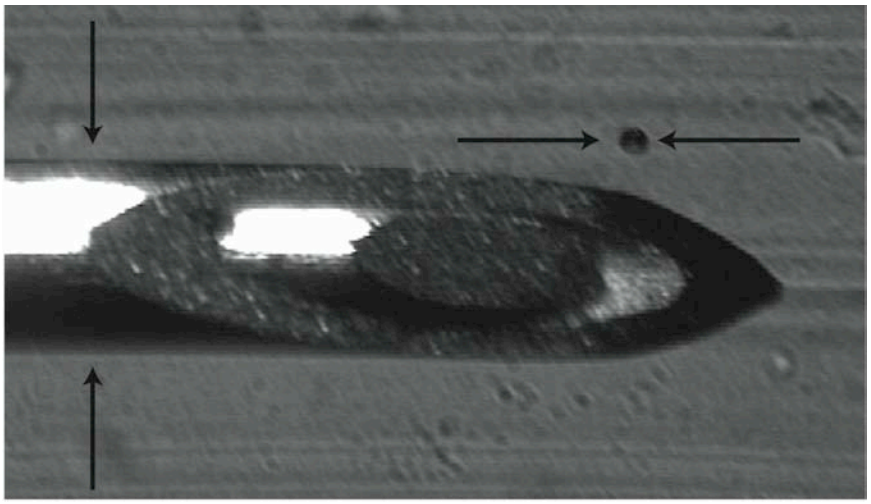

Figure 2.2: Sample image of an air bubble (104 μm $\pm$ 11 μm) and 22 gauge needle (705 μm $\pm$ 5 μm diameter). The needle was used as the reference scale when determining bubble sizes and then removed for experiments.

LithoClear ultrasound gel (Sonotech Inc., Bellingham, WA, USA), which is free of micro- and macro-bubbles. Dialysis tubing was used because of its relatively low echogenicity. The high viscosity of LithoClear significantly reduced bubble motion due to buoyancy. The dialysis tubing was held taut, reducing lateral motion due to water currents. As a result, microbubbles could be suspended, without axial, lateral, or elevational motion, for tens of minutes. A stereo-microscope (Nikon SMZ-U, Nikon, Melville, NY, USA) was used to observe changes in bubble diameter due to bubble dissolution or gas uptake (fig. 2.2).

The initial method used to create air bubbles was direct injection of air using a 25-gauge quincke-type spinal needle (Becton, Dickinson and Company, Franklin Lakes, NJ, USA). Bubbles were created by partially withdrawing the stylet in air. Then the tip of the needle was placed at the desired location for the bubble in the LithoClear. The stylet was then fully inserted in the needle. The air in the hollow of the needle was displaced into the gel and formed a bubble. The size of the bubble could be varied based on how much the stylet was initially withdrawn. Bubbles could be removed from the gel by placing the needle tip near the bubble

and removing the stylet partially to create a vacuum. These techniques allowed for the precise positioning of bubbles within the dialysis tube and the removal of any bubbles introduced when injecting the LithoClear into the dialysis tubing. All bubbles created in this manner will hereafter be referred to as air bubbles. Air bubbles under 150 μm were found to be particularly susceptible to dissolution. The smaller the bubble size, the larger the Laplace pressure acting on the relatively highly diffusible gas (air).

The second method devised to create bubbles was direct injection of DDFP droplets into the LithoClear gel. Droplets were vaporized using the above described 10 MHz Diasonics linear array but this time operating at high transmit power. In the case of multiple droplets vaporizing, the spinal needle was used to remove all but one of the bubbles. All bubbles created in this manner will hereafter be referred to as ADV bubbles. These bubbles were found to be more stable and did not change diameter over the course of a single experiment (approximately ten minutes). The stability is primarily ascribed to the relatively high molecular weight of DDFP (C_5F_{12}), the approximate steady state between the infusing ambient gasses and the outfusing DDFP, and the Laplace pressure. This second method was used to ensure the results would be as close as possible to future *in vivo* work with ADV bubbles. However, the initial method of injecting air bubbles had the advantage of easier to control bubble size.

Bubble Detection

Figure 2.3 is a schematic of the setup used for acoustic detection of a single bubble. Initial alignment was performed with the skull removed. A diplexer (RDX-6, Ritec Inc., Warwick, RI, USA) allowed a 1 MHz, 38.1 mm diameter, unfocused Panametrics V392 transducer to be used in pulse-echo mode. The transmit pulse was created with an HP33120A arbitrary function generator and amplified with an ENI A-300 power amplifier. The receive signal was recorded with a Lecroy 9314L

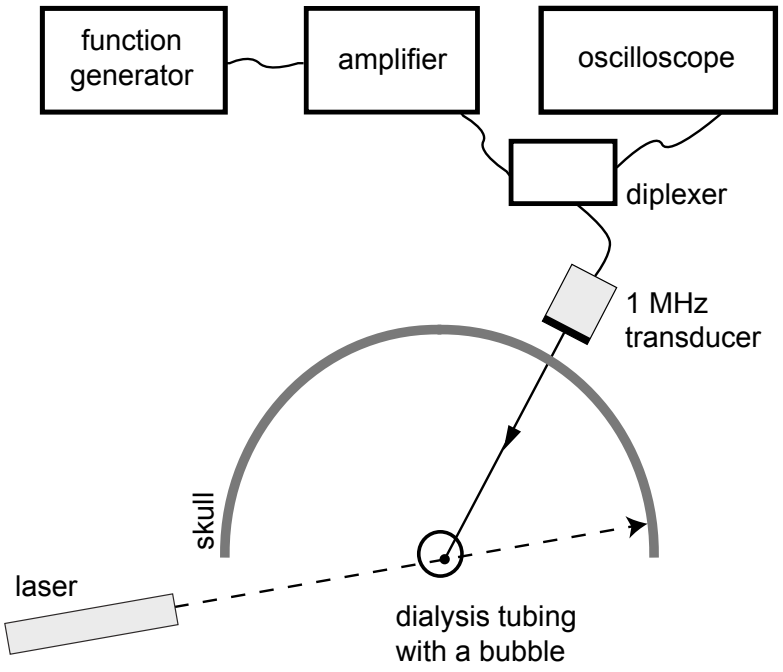

Figure 2.3: Schematic of setup used for single bubble acoustic detection.

oscilloscope (Chestnut Ridge, NY, USA). The transducer orientation was then adjusted by hand until the echo strength was maximized. The skull was then placed between the transducer and dialysis tubing. Following alignment, a laser beam perpendicular to the axis of the dialysis tube was used to mark the approximate location of the bubble. This allowed bubbles to be quickly placed in the correct position in subsequent experiments, which was important for small bubbles that dissolved quickly.

As the size of the bubble decreases, it becomes increasingly difficult to isolate the bubble-produced echo from reverberations due to the skull and echoes off the dialysis tubing. To reduce this problem, signal subtraction was used, where waveforms were obtained with and without extraction or dissolution of the bubble and then subtracted.

2.2.4 Time-Reversal Focusing

After detecting a single bubble transcranially, a synthetic aperture technique was used to perform aberration correction with time-reversal focusing. The synthetic aperture (fig. 2.4) was formed using two single-element, 1 MHz, 38.1 mm diameter V392 Panametrics transducers. One transducer was connected to a rotational stage to simulate elements of a curved aperture array. The center of rotation was approximately coincident with the center of the dialysis tubing.

Time-reversal focusing was initially performed by transmitting a short (3-7 cycle) 1 MHz burst from the stationary transducer with no bubble in place. The moving transducer then recorded the pitch-catch signal at N angles. Typically 60-150 temporal waveforms were averaged at each angle to minimize electronic noise. Next, a bubble was produced and the process repeated. Signal subtraction was performed at each angle i to yield: $r_i(t) = s_{i,\,bubble}(t) - s_{i,\,no\ bubble}(t)$, where $s_i(t)$ is the echo recorded at the i^{th} angle. These N waveforms were then time-reversed, $r_i(t) \rightarrow r_i(-t)$, and the amplitude of each waveform was normalized to its maximum absolute value: $u_i(t) = r_i(-t) \,/\, max_{(time)}[|r_i(t)|]$. Each waveform $u_i(t)$ was then retransmitted from the *moving* transducer at the i^{th} angle. The stationary transducer recorded the echo corresponding to each $u_i(t)$ transmitted. The bubble was then removed and the time-reversed waveforms were again retransmitted and the pitch-catch signal recorded at the appropriate angles again. Signal subtraction was again performed to remove signals not from the bubble (i.e. the skull and flow tube walls). This process demonstrates the ability to focus on transmit by having all transmitted signals arrive at the bubble at the same time and thus all echoes arrive at the receiving transducer at the same time. The entire process required approximately 10 minutes, primarily due to mechanical transducer motion and signal averaging. Future use of parallel acquisition with a more sensitive array can significantly reduce this time by eliminating the time due to motion and decreasing

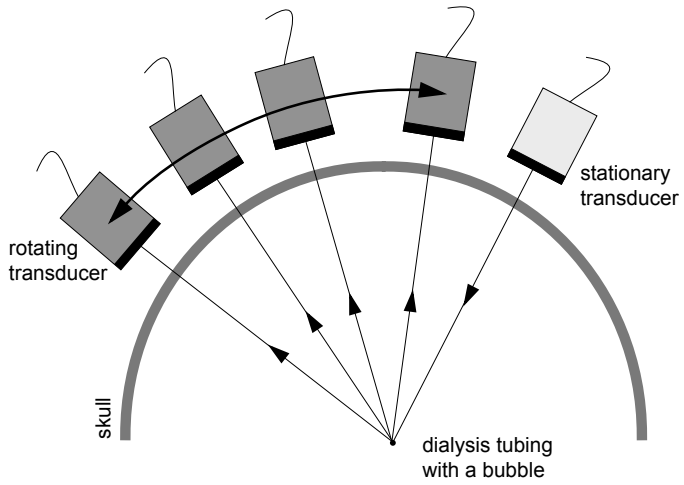

Figure 2.4: Schematic of the synthetic aperture setup used.

the required number of averages.

Spatial Reciprocity

To simplify and decrease the time needed to perform the aberration correction experiments it was desirable to transmit both the original pulse and the time-reversed waveform from the stationary transducer. This relies on spatial reciprocity since the source and receiver locations are switched when transmitting the time-reversed waveform. There may be multiple reasons for a violation of spatial reciprocity, for example mode conversion in the skull [28]. To test reciprocity, a synthetic aperture experiment was performed as described earlier using a 100 μm diameter wire as a target (for increased echogenicity and stability of the target). A second synthetic aperture experiment was performed with the stationary transducer transmitting both the initial pulse and the time-reversed signals. The corresponding waveforms were compared.

2.3 Results

2.3.1 Transcranial Insertion Loss

Hydration of the skull decreased the insertion loss (i.e. losses observed due to the insertion of the skull, as defined by Fry and Barger [24]) as shown during hours zero to forty-eight in the top plot of fig. 2.5. Initially, the transmission amplitude increased rapidly. After approximately 15 hours, the change in the signal decreased and the amplitude appeared to saturate. A $\lambda/4$ shift in the arrival time corresponding to a decrease in the average speed of sound was also observed during hydration. The decrease in speed of sound with hydration has been reported by others for other bones [23; 25; 29]. Since the arrival time and transmission appear to reach a steady state, it was assumed that the skull was fully hydrated after 48 hours. Data during degassing can be seen to the right of the vertical lines in figure 5. After 48 hours of degassing, the transmission amplitude had linearly increased from a normalized value of 0.6 to 1. The shift of the arrival time decreased in a manner similar to the change in expected gas content based on the multiple pinhole degassing technique.

For the set of experiments to follow, the absolute value of the insertion loss and speed of sound is not as important as maintaining constant values over the duration of the experiment. This is due to the extended time needed to perform each experiment as described above (approximately 10 minutes). As a result, all the following experiments will employ a skull that was hydrated in gas-saturated water for at least 48 hours.

Additionally it should be noted that several factors suggest that the experimental setup used will have an insertion loss equal to or greater than the insertion loss that would be experienced due to the skull only in an *in vivo* experiment. This is not described as a "worst-case" scenario (i.e. highest possible insertion loss) for measuring the echo from a micron-size air bubble because of the large variability in

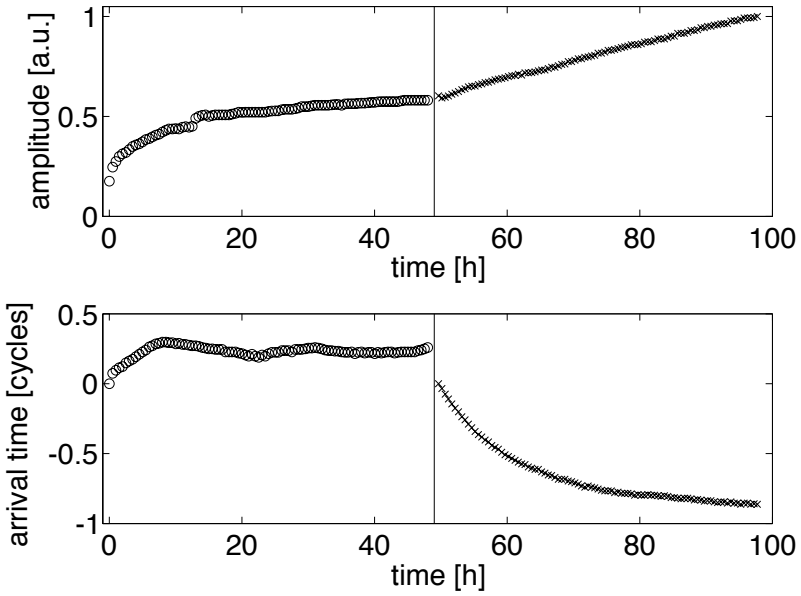

Figure 2.5: Transcranial pulse-echo amplitude (top) and arrival time (bottom) as a function of hydration and degassing time. All data points to the left of the vertical divider were taken during hydration of the skull; points to the right were taken for continued hydration and also degassing of the hydrating water.

attenuation from point-to-point on a skull and from skull to skull [30]. First, Fry and Barger[24] found that the insertion loss of formalin-fixed skulls was 3 dB greater than a fresh skull on average, indicating that in *in vivo* experiments, the skull bone insertion loss will decrease. Second, transmission was through the parietal bone approximately 3.5 cm posterior of the coronal suture, as opposed to the thinner and more acoustically transparent temporal bone. Finally, the aperture size of the transducers used likely increases the observed insertion losses due to phase averaging across the face of the transducer [29].

2.3.2 Transcranial ADV

Transcranial ADV, pre-, during, and post-vaporization can be seen in the left, middle, and right B-mode images respectively of fig. 2.6a. The increase in echogenicity during vaporization and persisting afterwards indicates the transcranial production of stable ADV bubbles and not the illumination of UCA and/or DDFP droplets.

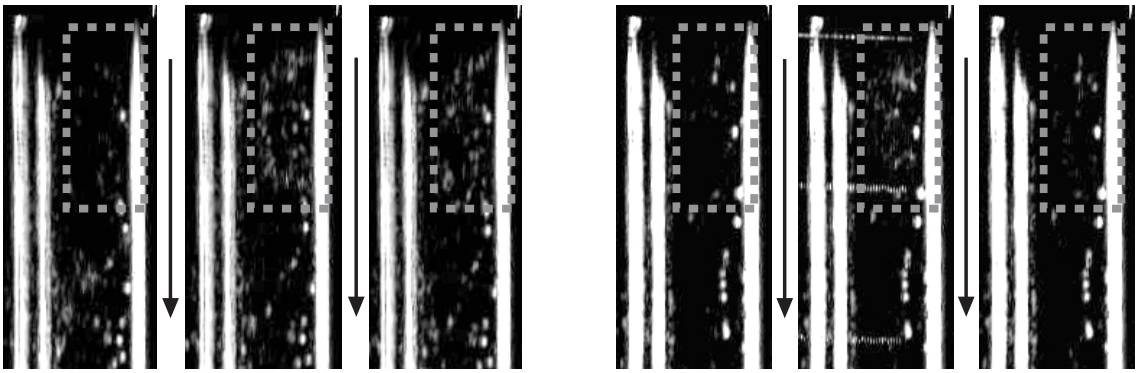

(a) (b)

Figure 2.6: Each image shows the flow tube either before the vaporization pulse (left), during the vaporization pulse (middle), or after the vaporization pulse (right). Flow is in the direction of the arrows. The gray dashed box indicates the approximate focus of the vaporization transducer. (a) A 1000 cycle vaporization pulse caused ADV with the increased echogenicity persisting after the pulse. (b) A 400 cycle pulse just illuminated the droplets and contrast agent during the pulse with no echogenicity persisting (b).

For comparison, sham experiments were performed with both high-amplitude, long duration (1000 cycle) vaporization pulses focused on a UCA/saline mixture (no DDFP droplets) in the flow tube and with high-amplitude but relatively short (400 cycle) vaporization pulses with the UCA/DDFP droplets/saline mixture. The first sham demonstrates the necessity of DDFP droplets. The second sham demonstrates that a threshold exists for being able to perform ADV. Figure 2.6b shows the B-mode images for the 400 cycle sham. In this case the pulse is too short to cause ADV at this amplitude [20] and as a result, the echogenicity increases only during the pulse as a result of the high amplitude illumination of UCA and DDFP droplets. A similar illumination result was seen when DDFP droplets were not in the flow mixture and long (1000 cycle), high amplitude vaporization pulses were used.

2.3.3 Single Bubble Production and Detection

The production of a single air bubble is seen optically in fig. 2.2. When detecting the bubble transcranially, signal subtraction increased the relative bubble echo

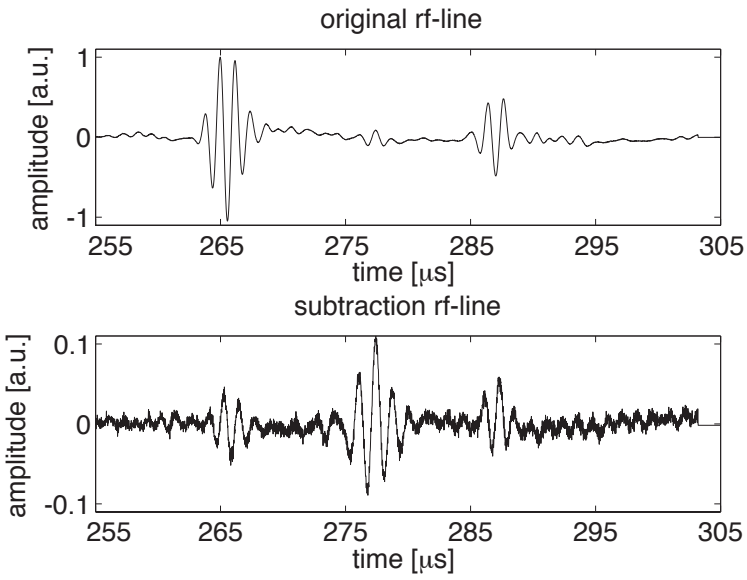

Figure 2.7: A waveform using a 118 μm bubble before subtraction (top) and, on the same time scale, after subtraction (bottom). The echo at 22 μs is from the bubble, while the echoes at 10 μs and 32 μs are from the dialysis tube walls. Both plots use the *same* arbitrary units, so the magnitudes of the waveforms can be directly compared.

amplitude as compared to other echoes and reverberations by an order of magnitude or more (fig. 2.7). Note that signal subtraction did not entirely eliminate echoes from the wall and reverberations related to the skull. This is likely due to unintended motion, such as the diameter of the dialysis tube wall increasing as the LithoClear hydrates. This will introduce errors in the later time-reversal experiments. Future *in vivo* work could employ similar techniques by recording waveforms before and after vaporization using array technology. Since this can be accomplished in a few milliseconds, suppression of non-bubble signals are anticipated to be greater, and most motion associated with the patient would not result in significant problems.

2.3.4 Time-Reversal Focusing

Waveforms testing spatial reciprocity in the configuration of fig. 2.4 can be seen in fig. 2.8. The significant decrease in amplitude after signal subtraction indicates that spatial reciprocity holds substantially for the experimental conditions.

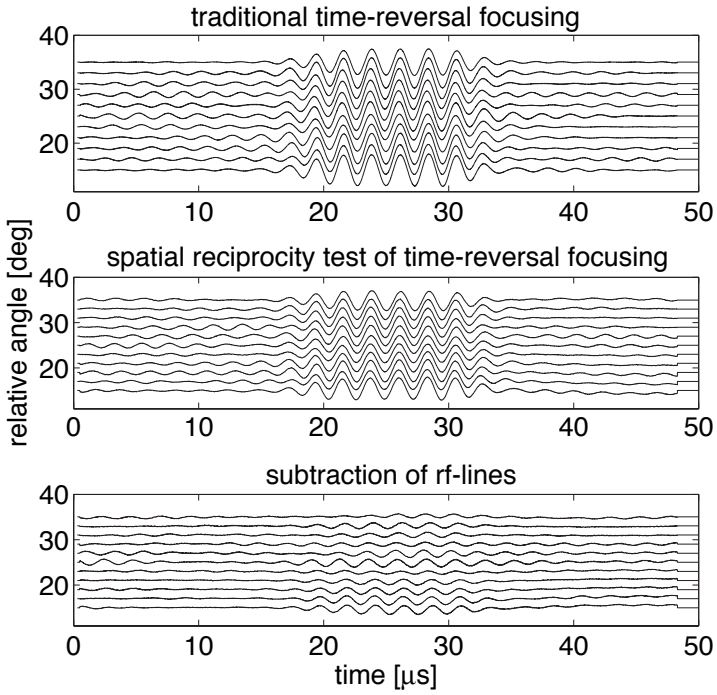

Figure 2.8: Series of sequential transcranial pitch-catch waveforms as a function of the angular position of the moveable transducer in fig. 2.4 for traditional time-reversal focusing (top), employing spatial reciprocity for time-reversal focusing (middle), and subtracting the two sets of waveforms to determine their similarity (bottom).

Quantitatively, the pulses for the subtracted waveforms have approximately 10% of the energy of the original waveforms. The incomplete subtraction may be due to small effects related to mode conversion, phase cancellation across the apertures, or possibly movement of the wire due to currents in the tank. All subsequent experiments transmit from the stationary transducer.

An example of transcranial time-reversal focusing with signal subtraction using an ADV bubble can be seen in fig. 2.9. The top plot shows amplitude normalized waveforms with skull-induced aberrations for various angular positions of the moveable transducer setup (fig. 2.4) with a maximum relative phase shift of nearly $\lambda/2$. The bold lines follow constant phase (based on the maximum amplitude of each waveform). Following time-reversal focusing, the waveforms are aligned with a maximum relative shift of only $\lambda/10$, which is primarily attributed to noise in the

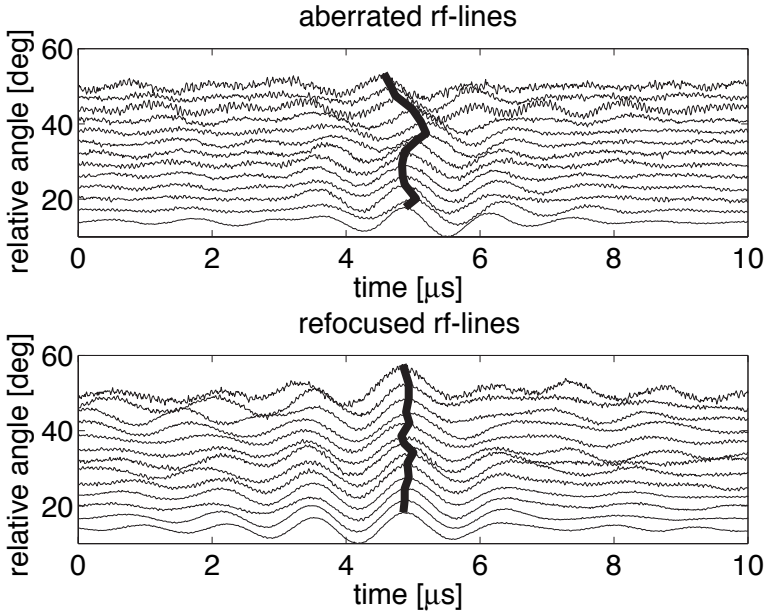

Figure 2.9: Transcranial waveforms for the synthetic aperture using a 118±24 μm ADV bubble before (top) and after time-reversal focusing (bottom). Each waveform amplitude has been individually normalized to unity to emphasize the (mis)alignment of phase.

waveforms, as can be seen most strongly in the large angle rf-lines. Additionally, the standard deviation of the phase shifts for the aberrated case is three and a half times greater than the corrected case (0.135λ and 0.038λ respectively). The waveforms that were transmitted at the relative angles of 47° and 50° appear to contain more noise and off-peak oscillations. For the particular orientation of the skull, the waveforms at larger angles were more significantly attenuated. As a result, after subtracting the original waveforms at this angle there was a relatively larger contribution from the incomplete subtraction of non-bubble related echoes and reverberations. The amplitude correction scheme employed in these experiments normalized the amplitude of all time-reversed waveforms to be transmitted to a peak-to-peak value of unity, thus accentuating these errors and causing the poorer results.

To quantify the effectiveness of the time-reversal focusing method, a focusing

factor F, similar to that defined by Mallart and Fink [31], was defined.

$$F = \frac{1}{N} \frac{\int \left(\sum_{i=1}^{N} \psi_i(t) \right)^2 dt}{\sum_{i=1}^{N} \int \psi_i^2(t) dt}, \tag{2.1}$$

where $\psi_i(t)$ refers to the i^{th} waveform with N waveforms recorded. The denominator of equation 2.1 is directly proportional to the total energy received by the aperature. The numerator is directly proportional to the energy received taking into account the interference caused by a misalignment of the phases of each waveform. In other words (with the proportionality constants canceling), equation 2.1 is the energy of the coherently summed waveforms divided by the sum of the energy of each individual waveform, normalized to unity. Focusing factors were computed for aberrated and corrected waveforms for seven bubbles ranging from approximately 35 μm to 1 mm (fig. 2.10a). Note that all of the bubbles are significantly above the bubble resonance diameter at 1 MHz (6 μm). Therefore the scattering amplitude should be linear at modest amplitudes. $F_{aberrated}$ ranged from 0.25 to 0.45 (except for one case discussed later), and $F_{corrected}$ ranged from 0.5 to 0.8. For reference, the focusing factor obtained when testing spatial reciprocity with the wire target was 0.95 (see previous discussion of spatial reciprocity as to why the focusing factor is not unity). This sets an upper bound for the expected values of F under more ideal circumstances.

Figure 2.10b shows the focusing factor ratio for each bubble ($F_{corrected}/F_{aberrated}$). The experiments were all performed through a similar portion of the skull (i.e. there was only minimal relative movement between the transducers, skull, and bubble for the various trials). The movable transducer traveled over an arc length of approximately 13 cm (35°), which is approximately 3.3 times the transducer diameter. Excluding the 360 μm bubble, which had a gain of 10.5, the gain from

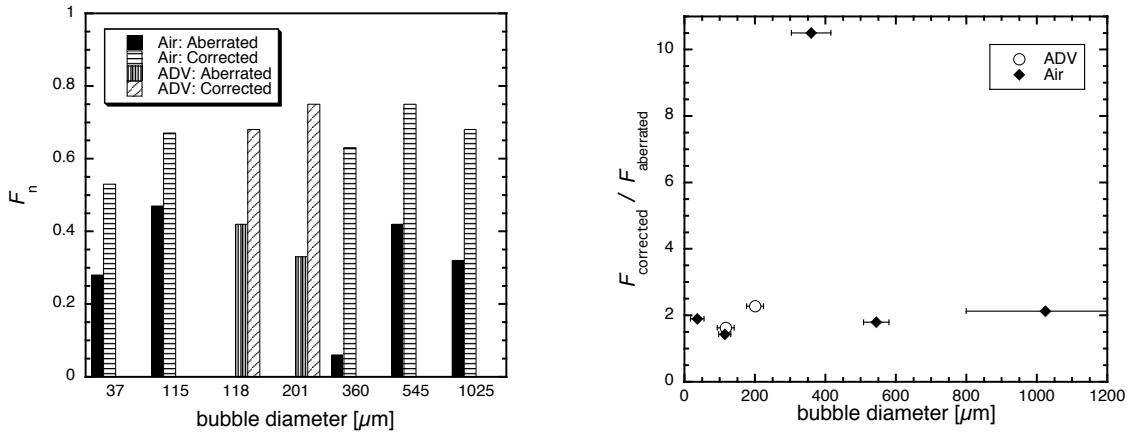

(a) (b)

Figure 2.10: (a) The focusing factor for seven bubbles before (gray) and after (black) aberration correction. (b) The gain in the focusing factor: $F_{corrected}/F_{aberrated}$. Uncertainty in bubble diameter is the result of blurring due to refraction in the optical imaging of the bubbles.

time-reversal focusing using a bubble is 1.9 ± 0.3 . For the 360 μm bubble, the aberration for the particular transducer-skull orientation was such that it resulted in nearly maximal destructive interference between the waveforms. This reduced $F_{aberrated}$ more significantly than in the other cases. In general, the variation of $F_{aberrated}$ is highly dependent on the skull location and can significantly affect the focusing factor ratio. For this reason, one should not assume that the gains reported here are the gains that will be observed in general for this approach to aberration correction. Rather these gains demonstrate that the technique yields improvements in focusing. The gains may also reflect a lower bound for what would be expected through this portion of the skull with more sophisticated array electronics, transmitters, and receivers (see below). Due to the larger variability of the skull, one should expect these gains to change as different portions of the skull are traversed, however these results show that one should expect there to be gains due to this process if there is any aberration of the beam. The use of 38.1 mm diameter transducers minimized and smoothed the aberration fluctuations across the skull because of phase averaging over the face of the transducer. Future work with

smaller transducer elements ($\lambda/2$ to λ in diameter) will result in significantly less phase averaging and thus more variation. It is hypothesized that this will lead to even smaller focusing factors in the aberrated case. Work done at higher frequencies is also be expected to decrease $F_{aberrated}$ due to the frequency dependence of human skulls [24]. More sophisticated electronics with lower capacitive losses and a better signal to noise ratio will also yield better sensitivity to small acoustic amplitudes and thus better alignment of phases, increasing $F_{corrected}$.

2.4 Discussion and Summary

The demonstration of transcranial ADV was provided as a proof-of-concept. No effort was placed in determining the minimum pulse-lengths or pressure amplitude needed to cause ADV. It has been seen that there are multiple regimes for inducing ADV when using different values for variables such as frequency, pulse-length, pressure amplitude, and UCA [14; 19; 20]. Further study of these mechanisms and their corresponding thresholds should be performed to see which ones will be most amenable to achieving transcranial ADV with conditions that would be acceptable for *in vivo* studies. Additionally, the design of future arrays will play a role in determining the pulse-lengths and transmit amplitudes needed based on the relationship between the array's spatial extent and the corresponding degree of aberration. This in turn will be subject to skull heating limitations (for therapeutic arrays). Here it is merely demonstrated that transcranial ADV is achievable.

In addition to transcranial ADV, the above experiments have demonstrated the ability to perform transcranial aberration correction on transmit with a single ADV bubble using time-reversal focusing. It is acknowledged that this approach was limited since it employed a synthetic aperture (with an unfocused element), rather than a full one-dimensional or two-dimensional aperture as would be ideal. It was however, a simple and effective means of demonstrating the effect. The

use of a synthetic aperture does not allow one to perform the typical spatial lateral-elevational focusing based on interference of multiple simultaneously fired waveforms. Without being able to fire multiple waveforms simultaneously, one does not achieve the "null" spots in the field where the waveforms interfere destructively and thus would not produce an echo if a scatterer were placed there. With a synthetic aperture the "null" does not exist and thus one does receive scattering from the location prior to summing individual receive signals. The synthetic aperture does allow the temporal (axial) focusing that was achievable with a single ADV bubble to be described. Having seen that temporal focusing is possible, one can expect spatial (lateral-elevational) focusing will be achieved with a full one-dimensional or two-dimensional array in future work. A parallel between these results and those achieved by Pavulescu and Clay [32] can be drawn. Both used unfocused sources in time-reversal experiments, in comparison to the more recent time-reversal experiments which have verified that spatial focusing does occur when directional arrays are used. Pavulescu and Clay [32] also demonstrate how this approach, using non-directional (unfocused) transmitters, takes into account multiple paths and thus differentiates itself from merely adjusting the phases of the waveforms based on arrival times. If multiple paths are not significant, then the two methods become essentially degenerate.

Additionally, these experiments and results point towards a possible *in vivo*, ultrasound-only based transcranial aberration correction scheme for therapeutic ultrasound. First, a patient would receive an intravenous injection of micron-size, transpulmonary DDFP droplets and UCA. A few circulated droplets would then be vaporized in and near the region-of-interest using geometrical (spherical) focusing as aberrated by the skull. This can be done at low frequencies (500 kHz or less) to minimize the aberration of the beam and allow for vaporization only in or near the desired region. As Yin and Hynynen [1] showed numerically at 250 kHz, the foci

were only shifted by 1.6 $\pm$ 0.8 mm and the -3 dB beam width and length were 4.3 $\pm$ 1.0 mm and 7.7 $\pm$ 1.8 mm, respectively. This should allow for vaporization localization within these limits. The resulting sparse array of ADV bubbles could be used as point-scatterers for aberration correction, leading to higher-resolution and higher-intensity focused ultrasound therapy. If the vaporization is not close enough to the desired region, the aberration information obtained from the created bubbles may be used to more accurately steer the beam towards the desired location. ADV can be performed iteratively stepping towards the desired region, until it is reached. If tumor targeting is performed, using the technique described above, with an ultrasound array, preferably a two-dimensional array with independently addressable transmit and receive channels on every sub-wavelength element, aberration correction could be performed for high-resolution diagnosis, targeting, and treatment assessment, with the resolution approaching the value obtained in a water-path only experiment. Based on the experiments reported here, and those previously reported by others within the Basic Radiological Sciences Division at the University of Michigan, which demonstrate *in vivo* intravenous injections and vaporization of DDFP droplets, there is a high probability of realizing the ultrasound-only based transcranial aberration correction scheme just outlined for focusing on transmit.

The next step will be to use one- or two-dimensional arrays to induce ADV and then perform aberration correction with the newly created ADV bubbles. As part of this work, a study of the effect of more closely spaced bubbles and the ability to chose which bubble to focus on should be done. The ability to create an appropriately sparse distribution of bubbles should be demonstrated for focusing throughout a region-of-interest. Additionally, more sophisticated amplitude correction schemes should yield additional improvements to the focusing [33; 34].

Currently, the techniques that have been reported only demonstrate temporal waveform realignment on transmit, as could be recorded *in vivo* for therapy.

Image formation however requires focusing on transmit and receive. Focusing on transmit is essentially concerned with minimizing the spatial extent of the focal spot and minimizing sidelobes. Both of these are done so that all returning echos can be associated as coming from the same location (as described above). Focusing on receive is concerned with properly associating the returning echos with a grayscale value at a particular known location, i.e. creating an actual image from the received data. Knowledge of the precise location of the bubbles is, however, currently unknown, thus making image formation problematic. One might be able to circumvent this problem by obtaining the approximate location of the bubbles from a poor resolution unaberrated image using low frequencies. The aberration corrected data could then be registered to the low frequency image. Alternatively, one could perform matched-filter processing based reconstruction. In this technique, one would use the scatter from individual scatterers to get the correct delays for summing the waveforms appropriately. However to determine the location of the scatterers, the scattered waveforms can be fitted to spherical delays. This technique would clean-up an image by focusing on transmit and receive correctly, but would also result in warping due to the determination of scatterer location from a best-fit to cylindrical delays. A second technique that can be envisioned is transmitting at low frequencies to vaporize and produce echoes from the bubble. Then filtering the receive signal for the second (or higher) harmonic and retransmitting the time-reversed harmonic to focus with greater precision. The filtering may be done individually on each waveform to create a 'boot-strapping' technique to focus on the bubbles at higher frequencies iteratively or as a step in the DORT method [35]. This process could be iterated. More sophisticated receive focusing algorithms may be developed in the future.

2.5 Acknowledgements

This work was supported in part by NIH grants R01EB000281 and R21CA116043.

REFERENCES

[1] X. Yin and K. Hynynen, "A numerical study of transcranial focused ultrasound beam propagation at low frequency," *Physics in Medicine and Biology*, vol. 50, pp. 1821–1836, April 2005.

[2] J. Sun and K. Hynynen, "Focusing of therapeutic ultrasound through a human skull: A numerical study," *Journal of the Acoustical Society of America*, vol. 104, pp. 1705–1715, September 1998.

[3] J. Sun and K. Hynynen, "The potential of transskull ultrasound therapy and surgery using the maximum available surface area," *Journal of the Acoustical Society of America*, vol. 105, pp. 2519–2527, April 1999.

[4] G. T. Clement and K. Hynynen, "Correlation of ultrasound phase with physical skull properties," *Ultrasound in Medicine and Biology*, vol. 28, no. 5, pp. 617–624, 2002.

[5] J. F. Aubry, M. Tanter, M. Pernot, J. L. .Thomas, and M. Fink, "Experimental demonstration of noninvasive transskull adaptive focusing based on prior computed tomography scans," *Journal of the Acoustical Society of America*, vol. 113, pp. 84–93, January 2003.

[6] G. T. Clement and K. Hynynen, "A non-invasive method for focusing ultrasound through the human skull," *Physics in Medicine and Biology*, vol. 47, pp. 1219–1236, April 2002.

[7] K. Hynynen, N. McDannold, G. T. Clement, F. A. Jolesz, E. Zadicario, R. Killiany, T. Moore, and D. Rosen, "Pre-clinical testing of a phased array ultrasound system for MRI-guided noninvasive surgery of the brain - a primate study," *European Journal of Radiology*, vol. 59, pp. 149–156, 2006.

[8] F. Vignon, J. F. Aubry, M. Tanter, and M. Fink, "Adaptive focusing for transcranial ultrasound imaging using dual arrays," *Journal of the Acoustical Society of America*, vol. 120, pp. 2737–2745, November 2006.

[9] S. Flax and M. O'Donnell, "Phase-aberration correction using signals from point reflectors and diffuse scatterers: Basic principles," *IEEE Transactions on Ultrasonics, Ferroelectrics, and Frequency Control*, vol. 35, no. 6, pp. 758–767, 1988.

[10] D. Zhao and G. E. Trahey, "Comparisons of image quality factors for phase aberration correction with diffuse and point targets: Theory and experiments," *IEEE Transactions on Ultrasonics, Ferroelectrics, and Frequency Control*, vol. 38, pp. 125–132, March 1991.

[11] M. Fink, "Time-reversal of ultrasonic fields - Part I: Basic principles," *IEEE Transactions on Ultrasonics, Ferroelectrics, and Frequency Control*, vol. 39, pp. 555–566, September 1992.

[12] M. Pernot, G. Montaldo, M. Tanter, and M. Fink, ""Ultrasonic stars" for time-reversal focusing using induced cavitation bubbles," *Applied Physics Letters*, vol. 88, no. 034102, pp. 1–3, 2006.

[13] J. Gateau, L. Marsac, M. Pernot, J.-F. Aubry, M. Tanter, and M. Fink, "Reaching the optimal focusing and steering capabilities of transcranial hifu arrays based on time reversal of acoustically induced cavitation bubble signature," *IEEE Ultrasonics Symposium*, vol. 1, 2008.

[14] O. D. Kripfgans, J. B. Fowlkes, M. Woydt, O. P. Eldevik, and P. L. Carson, "*In vivo* droplet vaporization for occlusion therapy and phase aberration correction," *IEEE Transactions on Ultrasonics, Ferroelectrics, and Frequency Control*, vol. 49, no. 2, pp. 726–738, 2002.

[15] D. Psychoudakis, J. B. Fowlkes, J. L. Volakis, and P. L. Carson, "Potential of microbubbles for use as point targets in phase aberration correction," *IEEE Transactions on Ultrasonics, Ferroelectrics, and Frequency Control*, vol. 51, pp. 1639–1648, December 2004.

[16] R. E. Apfel, "Activatable infusable dispersions containing drops of a superheated liquid for methods of therapy and diagnosis," Patent 5,840,276, Apfel Enterprises, Inc., November 1998.

[17] O. D. Kripfgans, M. L. Fabilli, P. L. Carson, and J. B. Fowlkes, "On the acoustic vaporization of micrometer-sized droplets," *Journal of the Acoustical Society of America*, vol. 116, pp. 272–281, July 2004.

[18] O. D. Kripfgans, J. B. Fowlkes, D. L. Miller, O. P. Eldevik, and P. L. Carson, "Acoustic droplet vaporization for therapeutic and diagnostic applications," *Ultrasound in Medicine and Biology*, vol. 26, no. 7, pp. 1177–1189, 2000.

[19] T. Giesecke and K. Hynynen, "Ultrasound-mediated cavitation thresholds of liquid perfluorocarbon droplets *In Vitro*," *Ultrasound in Medicine and Biology*, vol. 29, no. 9, pp. 1359–1365, 2003.

[20] A. H. Lo, O. D. Kripfgans, P. L. Carson, E. D. Rothman, and J. B. Fowlkes, "Acoustic droplet vaporization: Effects of pulse duration and contrast agent," *IEEE Transactions on Ultrasonics, Ferroelectrics, and Frequency Control*, vol. 54, pp. 933–946, May 2007.

[21] M. L. Fabilli, K. J. Haworth, N. H. Fakhri, O. D. Kripfgans, P. L. Carson, and J. B. Fowlkes, "The role of inertial cavitation in acoustic droplet vaporization," *IEEE Transactions on Ultrasonics, Ferroelectrics, and Frequency Control*, vol. Accepted, 2009.

[22] O. D. Kripfgans, C. M. Orifici, P. L. Carson, K. A. Ives, O. P. Eldevik, and J. B. Fowlkes, "Acoustic droplet vaporization for temporal and spatial control of tissue occlusion: A kidney study," *IEEE Transactions on Ultrasonics, Ferroelectrics, and Frequency Control*, vol. 52, pp. 1101–1110, July 2005.

[23] S. B. Lang, "Ultrasonic method for measuring elastic coefficients of bone and results on fresh and dried bovine bones," *IEEE Transactions on Biomedical Engineering*, vol. BME-17, pp. 101–105, 1970.

[24] F. J. Fry and J. E. Barger, "Acoustical properties of the human skull," *Journal of the Acoustical Society of America*, vol. 63, pp. 1578–1590, May 1978.

[25] S. Lees, P. F. Cleary, J. D. Heeley, and E. L. Gariepy, "Distribution of sonic plieso-velocity in a compact bone sample," *Journal of the Acoustical Society of America*, vol. 66, pp. 641–646, September 1979.

[26] K. Erikson, R. Banjavic, and P. L. Carson, "Standard methods for testing single-element pulse-echo ultrasonic transducers," tech. rep., American Institue of Ultrasound in Medicine, August 1981.

[27] A. R. Kaiser, C. A. Cain, E. Y. Hwang, and J. B. Fowlkes, "A cost effective degassing system for use in ultrasonic measurements: The multiple pinhole degassing system," *Journal of the Acoustical Society of America*, vol. 99, pp. 3857–3860, June 1996.

[28] P. J. White, K. Hynynen, and G. T. Clement, "Longitudinal and shear mode ultrasound propagation in human skull bone," in *Therapeutic Ultrasound: 5th International Symposium on Therapeutic Ultrasound*, vol. 5, pp. 251–255, International Symposium on Therapeutic Ultrasound, American Institute of Physics, 2006.

[29] F. A. Duck, *Physical Properties of Tissue: A Comprehensive Reference Book*. Academic Press Limited, 24-28 Oval Road, London NW1 7DX: Academic Press Inc., 1990.

[30] H. Theismann and F. Pfander, "Über die durchlässigkeit des knochens für ultraschall," *Strahlentherapie*, vol. 80, pp. 607–610, 1949.

[31] R. Mallart and M. Fink, "Adaptive focusing in scattering media through sound-speed inhomogeneities: The van cittert zernike approach and focusing criterion," *Journal of the Acoustical Society of America*, vol. 96, pp. 3721–3732, December 1994.

[32] A. Parvulescu and C. S. Clay, "Reproducibility of signal transmissions in the ocean," *The Radio and Electronic Engineer*, vol. 29, pp. 223–228, April 1965.

[33] M. Pernot, J. F. Aubry, J. L. Thomas, and M. Fink, "High power transcranial beam steering for ultrasonic brain therapy," *Physics in Medicine and Biology*, vol. 48, pp. 2577–2589, 2003.

[34] J. White, G. T. Clement, and K. Hynynen, "Transcranial ultrasound focus reconstruction with phase and amplitude correction," *IEEE Transactions on Ultrasonics, Ferroelectrics, and Frequency Control*, vol. 52, pp. 1518–1522, September 2005.

[35] C. Prada, S. Manneville, D. Spoliansky, and M. Fink, "Decomposition of the time reversal operator: Detection and selective focusing on two scatterers," *Journal of the Acoustical Society of America*, vol. 99, pp. 2067–2076, April 1996.

CHAPTER III

Receive Aberration Correction with Synthetic Aperture Imaging

3.1 Introduction

Among the results presented in the previous chapter, it was seen that bubbles created via ADV can be used to focus a transmitted signal. For therapeutic applications, this encompasses all of the aberration correction that is needed. However for imaging applications, it is important to focus on both transmit *and* receive. Focusing on transmit (using a standard beamforming approach) minimizes the scatter that comes from objects away from the desired location (i.e. the focus). Focusing on receive properly aligns the scattered waveforms so that they can be summed correctly to form a sharper, higher-contrast image. Over the course of the chapter, it will be seen that ADV bubbles can be used to focus a signal on receive. The aim is to show that with a given aberration correction algorithm, it is possible to perform aberration correction on receive and thus form an aberration corrected image using an ADV bubble as a point target.

3.2 Background

As described earlier, a basic time-reversal experiment consists of a signal transmitted into a medium that scatters off objects of interest. The scattered signal is recorded by the array, time-reversed, and retransmitted. Due to time-reversal invariance

the retransmitted waves refocus on the scattered objects. If a dominant scatterer is present, then the time-reversed signal will predominately focus on the scatterer and minimal energy will be transmitted elsewhere. If the dominant scatterer is a point-scatterer in an otherwise homogenous medium, then the signal that would be received without aberration is a spherical wave. Any deviations of the wavefront from sphericity would be the aberrations due to inhomogenity of the medium. By comparing the wavefront to a spherical wavefront, it is possible to measure the aberration and apply this aberration to future transmitted and received signals to correct for the aberrations. Chapter I listed a variety of point-target based methods. For the following work, the decomposition of the time-reversal operator method (known by its acronym in french, Décomposition de l'opérateur de retournement temporel, DORT) will be used.

3.2.1 Decomposition of the Time-Reversal Operator

The DORT method was discovered by Prada *et al.* after studying the iterative time-reversal method of focusing [1]. The iterative time-reversal method is described by the transmission of an acoustic wave into a region of interest. Supposing that the region is homogenous except for two point-scatterers of differing scattering strength, the received signal would be two superimposed spherical waves. The amplitudes of the waves would depend on the amplitude of the initial interrogating wave at each scatterer and the scattering cross-section. If one of the scattered spherical waves is larger, then upon time-reversal more of the acoustic energy will be transmitted to the corresponding scatterer and less to the other scatterer. The backscattered amplitude difference between the two scattered waves will increase further. With each iteration, the spherical wave from the originally stronger scattering object will grow and the spherical wave from the weaker scatterer will diminish. Eventually the time-reversed signal will only effectively focus on the strong scatterer. At this point, the signals transmitted and received will not change any more. From a linear algebra

perspective, if the propagation is treated as a matrix and the transmitted signals as a vector, this describes an eigenmode problem [2; 3].

To develop this process mathematically [1; 2], it is necessary to create a matrix that describes how the signal from any element will interact with the medium and then be received by any other element. This information is the inter-element impulse response for all combinations of element transmits and receives. The easiest (though not necessarily best) way to obtain this information is to transmit a short pulse from a single element and receive the scattered signal on all of the elements (including the one that just transmitted). This process can be repeated until all of the elements have fired. This process will result in an $N \times N \times n_t$ matrix, where N is the number of elements and n_t is the number of digitized samples in each recorded rf-signal. This 3D matrix is often called the propagation matrix or transfer matrix, $\bar{K}(t)$. The first step of the iteration process would result in a received signal of $\bar{K}(t) \otimes e(t)$, where $\otimes$ denotes the convolution operation and $e(t)$ is the set of waveforms transmitted on each element. It is common to work in the frequency domain so that the convolutions become multiplications. The functional dependence on frequency ω will be dropped in all that follows. The time-reversed signal is then given by $\bar{K}^* e^*$, where * denotes taking the Hermitian conjugate of the matrix/vector at all frequencies. The signal received after transmitting the time-reversed signal is $\bar{K}\bar{K}^* e^*$. Based on the earlier discussion, rather than time-reversing and retransmitting this signal and repeating the process to arrive at the scatter from a single source, the eigenmodes of $\bar{K}\bar{K}^*$ can be computed directly. (Note that $\bar{K}\bar{K}^*$ is known as the time-reversal operator.) For any matrix times its own Hermitian conjugate, the eigenmode decomposition is equivalent to a singular value decomposition (SVD), except for scaling factors [3]. The SVD is easily implemented in MATLAB (The Mathworks, Inc., Natick, MA, USA). The SVD will give N eigenvectors and eigenvalues. If there are $m < N$ scatterers, then there will be m eigenvalues that are significantly larger than the rest

of the eigenvalues. These eigenvalues correspond to the relative scattering strength of each of the m scatterers. The corresponding eigenvectors are the waveforms corresponding to the signals that need to be transmitted from each element to focus on the particular scatterer.

Thus, given the propagation matrix $\bar{K}$, it is possible to obtain the scattered signal from a point target with no *a priori* knowledge of the medium. Figure. 3.1 demonstrates DORT using Field II [4; 5]. Figure 3.1a shows the maximum pressure at each field point from the cumulative illumination of each step of building $\bar{K}$. The asterisks show the location of three simulated point-scatterers. The DORT algorithm was run and three significant eigenvalues were found. Figure 3.1b shows the pressure field that results from transmitting the waveforms in the first 'temporal eigenvector' (see section 3.3.2 for the definition of a 'temporal eigenvector'). It is seen that the pressure field is focused on one of the scatterers. Figure 3.1c shows the pressure field that results from transmitting the summation of the waveforms in the second and third eigenvector. Thus using DORT, it can be seen that it is possible to focus on any individual scatterer or combination of scatterers in this simple situation.

3.2.2 Synthetic Aperture Imaging

In order to perform DORT, the propagation matrix $\bar{K}$ must be obtained. Conveniently, $\bar{K}$ is also the data set needed to perform synthetic aperture (SA) imaging. Thus by collecting a single data set, it is possible to create an image and determine the waveforms needed to focus on a point target.

SA imaging works by associating each pixel in an image with the time it would take for an element i to transmit a signal, for the signal to reach the pixel location and scatter to element j. A very low quality image is then formed by assigning each pixel amplitude based on the amplitude in the rf-line corresponding to transmitting on element i and receiving on element j. The image at this stage is an rf-image and has not been envelope detected. If the elements have a transmit or receive beam

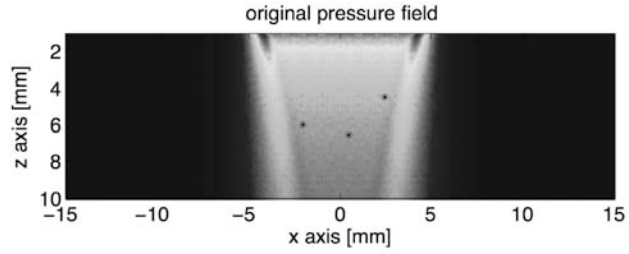

(a)

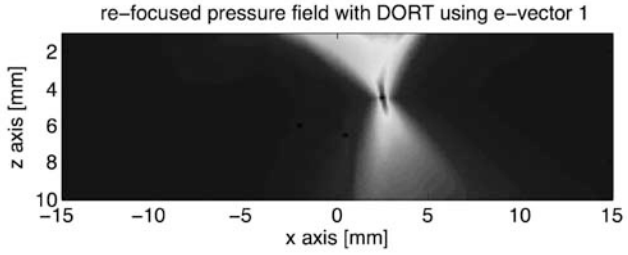

(b)

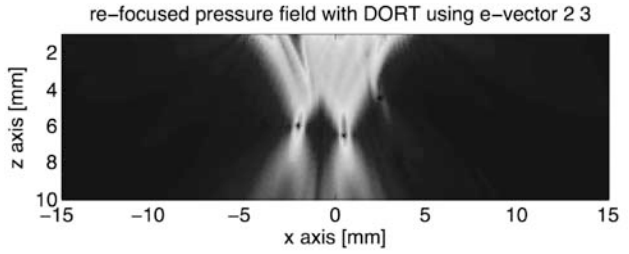

(c)

Figure 3.1: (a) The cumulative pressure field after firing each element of the array. (b) The pressure field obtained by transmitting the waveforms of the first eigenvector of $\bar{K}\bar{K}^*$. (c) The pressure field obtained by transmitting the summation of the waveforms of the second and third eigenvector of $\bar{K}\bar{K}^*$.

pattern, the beam pattern should be used as an apodization factor when creating the images. Assuming that the transmit and receive beam patterns are the same, the pixel amplitude at the location (x, y) in the rf-based image for transmitting from element i and receiving on element j is [6]:

$$I^{rf}_{(i,j)}(x,y) = a_i(x,y) \cdot a_j(x,y) \cdot r_{(i,j)}\left(t = \frac{\sqrt{(x-x_i)^2+y^2}}{c} + \frac{\sqrt{(x-x_j)^2+y^2}}{c}\right), \quad (3.1)$$

where $a_i(x, y)$ is the beam pattern for element i at the location (x, y), and $r_{(i,j)}(t)$ is the rf-line corresponding to transmitting from element i and receiving on element j. Note that $t = \frac{\sqrt{(x-x_i)^2+y^2}}{c} + \frac{\sqrt{(x-x_j)^2+y^2}}{c}$ corresponds to the time taken for the signal to transmit from element i to the location (x, y) and scatter to element j. The speed of sound in the material is c. Here it has been assumed that all of the elements are located at $y = 0$. Note that this equation makes the assumption of a homogenous, isotropic medium in converting temporal data to spatial data.

If there are N transmit and receive elements, there will be $N \times N$ images that can be created. Each of these rf-based images can be summed to create a high-quality image [6].

$$I(x,y) = \mathfrak{B}\left\{\sum_{i=1}^{N}\sum_{j=1}^{N} I^{rf}_{(i,j)}(x,y)\right\}, \quad (3.2)$$

where $\mathfrak{B}$ is the operator that envelope detects the summed signal (e.g. standard IQ basebanding or the magnitude of the Hilbert transform). Figure 3.2 shows an image created from the echo off of a 110 μm thread with and without using the field pattern of a single element for apodization.

3.2.3 Aberration Corrected SA Imaging

For a heterogenous (albeit lossless) medium that obeys the Born weak scattering approximation, the conversion between temporal and spatial data must be modified to account for a varying speed of sound along the propagation paths (which

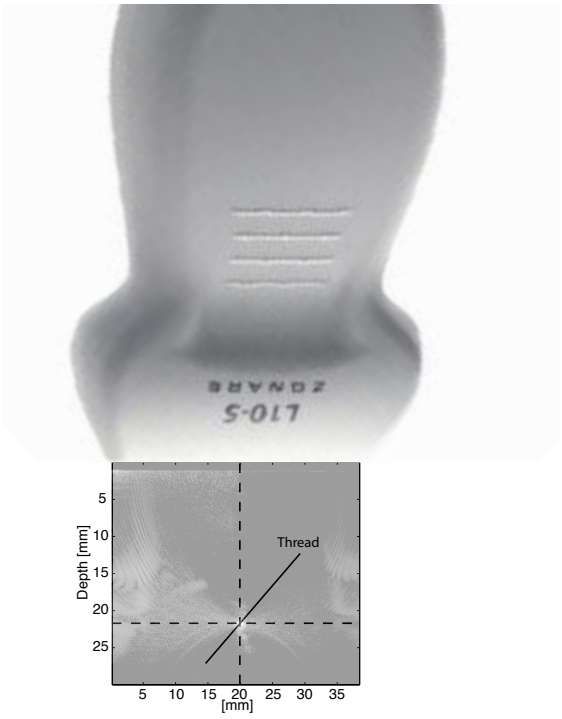

(a)

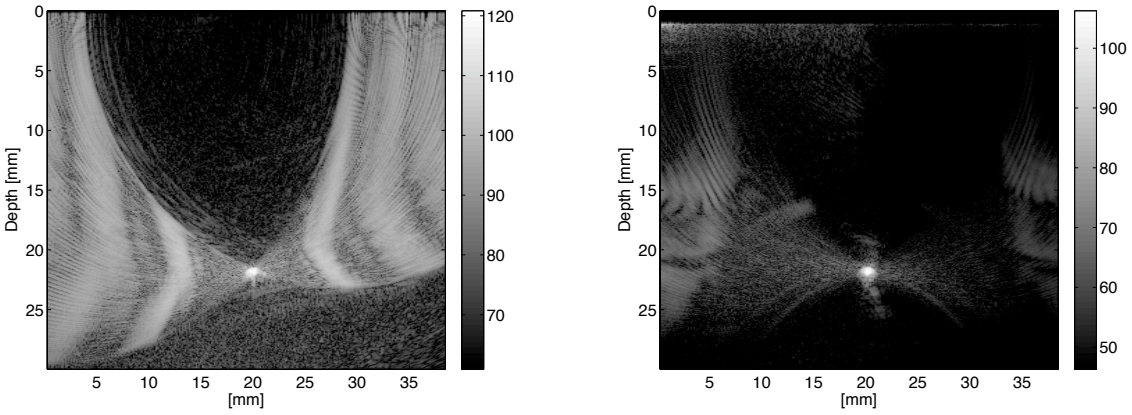

(b) (c)

Figure 3.2: (a) Schematic showing L10-5 transducer and the relative orientation of the thread passing perpendicularly through the axial-lateral plane. (b) A synthetic aperture image created without beam pattern apodization. (c) A synthetic aperture image created with beam pattern apodization. Note the reduction of artifacts. The grating lobe artifacts are due to the array being undersampled relative to $\lambda/2$.

themselves may no longer be straight lines). If the aberration can be modeled as a thin near-field phase screen, then the temporal to spatial conversion can be modeled as:

$$t_{i,j}(x,y) = \frac{\sqrt{(x-x_i)^2+y^2}}{c} + \tau_i(x,y) + \frac{\sqrt{(x-x_j)^2+y^2}}{c} + \tau_j(x,y), \tag{3.3}$$

where τ_i is the time-delay associated with the aberration in the thin near-field phase screen in front of element i.

The DORT algorithm can be used to determine $\tau_i(x,y)$ and $\tau_j(x,y)$. Suppose the medium being imaged contains only a single point-scatterer. When DORT is applied to the time-reversal operator, the first eigenvector will be the set of waveforms necessary to focus on the single point-scatterer. Without a thin near-field phase screen, the wavefront of these waveforms should be spherical. Whatever the wavefront deviation from spherical is, will be τ_i. In this manner the time-delays can be computed and taken into account to form an aberration corrected SA image.

3.3 Implementation

The above sections provided the conceptual outline for the following work. In order to perform this work, SA IQ data was captured using a z.one *ultra* system with an L10-5 transducer (Zonare Medical Systems, Inc., Mountain View, CA, USA). The z.one was controlled through both the standard user interface and a research platform. The research platform allowed for control using a PC connected via a serial port. SA IQ data acquisition on the z.one *ultra* allows for every other element in the array (excluding the first and last elements) to be fired sequentially (this corresponds to 63 transmits). For each firing, all 128 of the elements recorded the backscattered signal. Frequency compounding was turned off for each data collection. The transmit frequency, transmit delays, imaging depth, and time-gain compensation were all controlled. The collected SA IQ data was extracted and processed in MATLAB.

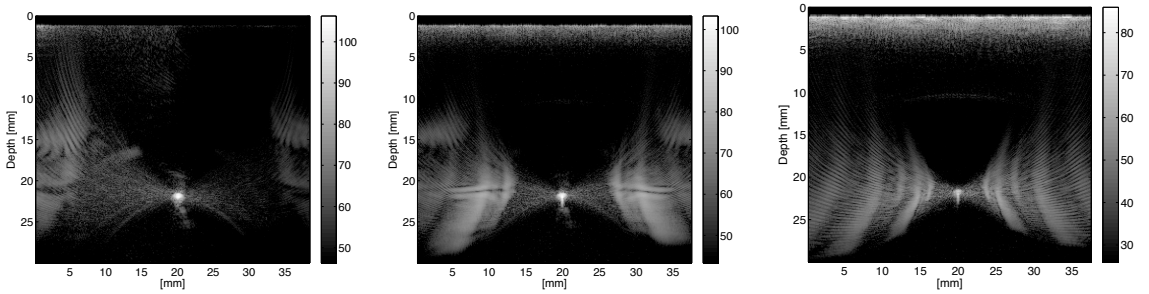

(a) (b) (c)

Figure 3.3: (a) Image reconstruction using all 63 transmit channels and 128 receive channels. (b) Image reconstruction using all 63 transmit channels but only receiving on the 63 elements that could transmit. This is the combination that can be used for DORT. (c) Image reconstruction using only the rf-lines that correspond to receiving on the same element that transmitted for a given firing. This increased the reconstruction speed by a factor of 63 compared to (b), but also introduced significant grating lobes.

3.3.1 Standard SA Image Reconstruction Parameters

Initially, a variety of image reconstruction (with no aberration correction) parameters were investigated to determine the practical limits of image formation. First, the impact of upsampling the IQ data for its conversion to rf-data was investigated. It was found that if the IQ data was not upsampled to approximately five times the transmit frequency or greater, a bright artifact would extend axially from any small targets (such as bubbles or thin wires) for several wavelengths do to inadequate recovery of signal bandwidth. Additionally, if the sampling frequency was not at least twice the transmit frequency, the speckle did not appear to fully develop and small targets became blurry. Thus, for all of the following work, all IQ data was upsampled to 50 MHz using cubic Hermite interpolation in MATLAB. With the data upsampled appropriately, the impact of speed of sound was assessed. The artifacts were found to be the same as with standard sum-and-delay beamforming.

Images were also created using different subsets of the receive transducers. Note that the pitch on the L10-5 is 300 μm. However since only every other element could be used on transmit, the effective transmit pitch is 600 μm. Both the receive and

transmit pitches are greater than a wavelength at the typical transmit frequencies of the L10-5 ($f = 6$ MHz $\rightarrow \lambda = 257\mu$m and $f = 8.5$ MHz $\rightarrow \lambda = 181\mu$m for $c = 1540$ m/s). Therefore the array is undersampled and grating lobes are expected. Figure 3.3a is formed using 63 transmit elements and all 128 receive elements, using the same setup shown in fig. 3.2a. Using the maximum number of elements creates the most well defined image with fewer grating lobes, as expected. The grating lobes occur at 32°, which is close to an expected location of 37° relative to the scatterer, transducer, and axial direction. For the DORT algorithm however, aberration can only be directly estimated for the 63 elements that transmit and receive signals. It may be that an interpolation between elements may allow for reasonable estimates of the aberration for the elements that only receive, but there is no direct method to obtain these aberrations. Therefore, aberration corrected images were created using the 63×63 rf-lines where the transducers both transmitted and received. A sample image is seen in fig. 3.3b. It is seen that the SNR is not as large, in addition to the increased grating lobes. The grating lobes occur at their expected location of 17°. Finally, an image was created using only the 63 rf-lines corresponding to transmitting and receiving on the same element. This image reconstruction method was approximately 63 times faster than the 63×63 method. It also maintained reasonable image quality because the majority of the acoustic energy was transmitted in this direction due to the element's beam pattern. As might be expected however, the grating lobes were even more prominent. In general, data sets were initially tested using the 63 rf-line reconstruction algorithm. High quality final images could then be created using the 63×63 or 63×128 methods.

A final reconstruction issue was the conversion of the rf-based images to envelope-detected images. This can be performed using a traditional basebanding approach [7]. However MATLAB has built in Hilbert transforms, which can be used to achieve the same result. The Hilbert transform computes the analytic signal of

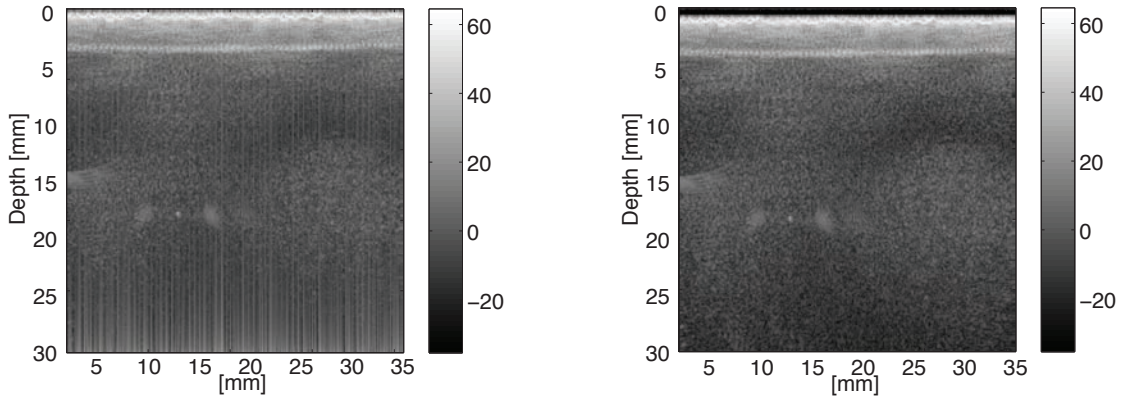

Figure 3.4: (a) Image created using `hilbert.m`. (b) Image created using a Hilbert filter built using the Remex exchange algorithm with Chebyshev approximation theory.

a given real signal. The analytic signal is composed of the original signal and an imaginary component that is 90° out of phase with the original signal. Thus the magnitude of the analytic signal directly gives the enveloped signal. The Hilbert transform should be performed along the axial lines. For cases where the peak amplitudes change greatly (approximately a factor of 1000) as one moves down an axial line, artifacts will appear when using `hilbert.m`. These artifacts can manifest themselves as increasing signal amplitude with depth that is not correlated to neighboring axial lines (fig. 3.4a).

This artifact is due to `hilbert.m` being a frequency sampling filter. Frequency sampling filters assume the signal is periodic and smoothly goes to zero at the beginning and end of the signal. As can be seen in the images, the initial portion of each axial line is very large, while the end of the signals is very small (recalling that the images are on a dB scale, the differences are up to a factor of 1000 or more). By assuming periodicity, the large signals skew the magnitude of the envelope at the end of the actual signal. This effect can be seen in simulated noise-free data (fig. 3.5). A sample rf-line was created at 7 MHz from $\sin(\omega t) \cdot e^{-\alpha t}$ (fig. 3.5a). The decay constant α was chosen so the signal would decay by a factor of 1000 across the axial

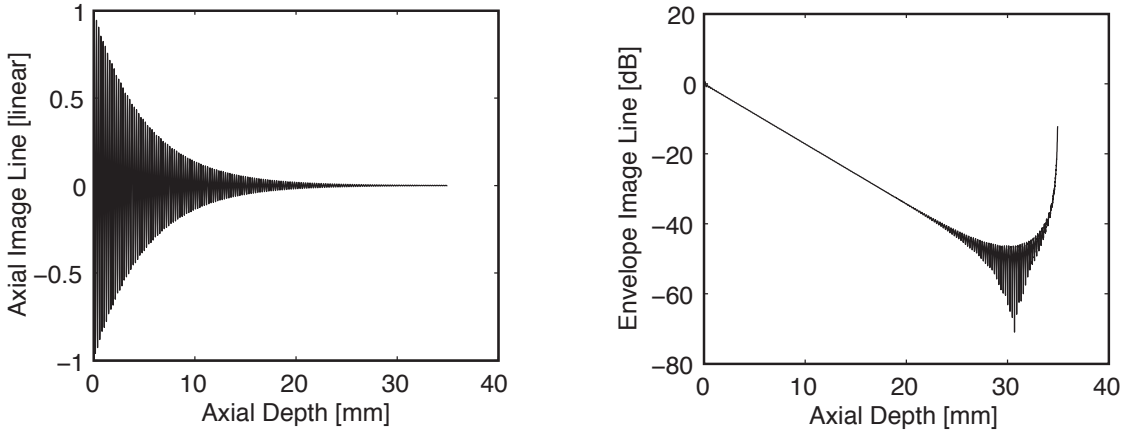

(a) (b)

Figure 3.5: (a) A simulated single axial line to be envelope detected that was created from: $\sin(\omega t) \cdot e^{-\alpha t}$, where α was chosen so the signal would decay by a factor of 1000 across the entire rf-line. (b) Hilbert transform of (a) using `hilbert.m`. The ringing at the end of the signal is Gibbs phenomena, while the frequency sampling artifact can be seen as the 30 dB increase over the last 5 mm of the rf-line

line. The Hilbert transform was obtained using MATLAB's `hilbert.m` and plotted (fig. 3.5b). Two artifacts appear. The first, which is most prominent around 30 mm is ringing due to Gibbs phenomenon (i.e. sharp truncation of the signal creating frequency components greater than half the sampling frequency, and thus beyond the Nyquist criterion). Note however, that at its largest amplitude, the ringing is still 40 dB or more below peak amplitudes, and thus not a significant concern. The second artifact is seen as the 30 dB increase in the signal over the last 5 mm of the enveloped line.

One adjustment that can be made to effectively remove this problem is to zero pad the end of the axial lines. Now the artifactual increase will occur in the zero padded region, which can then be cropped out of in the image. Zero padding the data can be done automatically with `hilbert.m` by using `hilbert(x, 2*length(x))` rather than just `hilbert(x)`. If artifacts persist (because of large echogenicity changes within the middle of the image) or zero padding is undesirable, an alternative method of performing the Hilbert transform is to create a filter using

the Remez exchange algorithm with Chebyshev approximation theory (REACAT) (see `firpm.m` in Matlab). A simple way to do this is:

```
function [xa] = remezhilbert(x, n)
% X is the signal you want the hilbert transform of
% N is the number of taps to use
% XA is the hilbert transform of X
if rem(n,2) == 0
     h = firpm(n,[0.1 0.9],[1 1],'hilbert');
     xh=filter(h,1,x);
     xd = [zeros(n/2,1); x(1:length(x)-n/2)];
     xa = xd + i*xh;
else
     sprintf('n must be even')
     xa = [];
end
xa = circshift(xa, n/2);
```

where `firpm()` is the MATLAB function for building a finite impulse response filter using REACAT. By using this approach, the artifacts associated with the frequency sampling method are removed (fig. 3.4b).

The primary differences between the two approaches is that frequency sampling allows the frequency to be specified precisely at a finite number of locations, but no specification is made about the amplitude and phase at the frequencies between the finite locations [8]. For many applications, a frequency sampling filter will have smooth change between the specified frequencies, particularly when the earlier mentioned assumptions are true. REACAT instead designs the filter by approximating the desired frequency response at all frequencies below the Nyquist criteron. The exact filter response at the frequencies specified in the frequency sampling method is not obtained, but the best possible response at all frequencies is obtained [8]. In practice, the Hilbert transform built into MATLAB may be used unless artifacts are suspected. Then zero padding can be added to the end of the rf-line until the artifact disappears. If this requires too much computational memory or is undesirable for other reasons, REACAT can be used. It should be noted that

REACAT is computationally slower and as with all finite impulse response filters, it induces a delay in the signal.

3.3.2 Implementation of the DORT algorithm

The basic implementation of the DORT algorithm is relatively simple: Fourier transform the RF data and apply the SVD to compute the eigenvectors. However, there are three points worth discussing. First, how to successfully transform from the frequency-domain back to the time-domain (recalling that the SVD is performed in the frequency domain). Second, how to preferentially select scatterers for DORT. Third, the importantance of symmetry in the data.

Single versus Multiple Frequency DORT

The initial algorithm proposed for DORT called for choosing a particular frequency at which to work [1; 2]. Since the phase in the Fourier transform is restricted to $[-\pi,\pi]$, it was assumed that the phase could be unwrapped and converted to a time-shift to obtain the aberration. This however limits the magnitude of the aberrations that can be corrected. The standard method for unwrapping the phase makes the assumption that the phase change between consecutive elements is not larger than a particular value, typically $\pm\pi$. When the jump is larger than the tolerance set, $\mp 2\pi$ is added to the data to unwrap it. If however, the element-to-element aberration is greater than the tolerance, unwrapping will occur when it should not. The occurrence of this problem is realistic. It has been reported that breast tissue can induce aberrations consisting of 100 ns time-shifts [9–12]. This is an $8\pi/5$ phase shift at 8 MHz.

Alternatively, the SVD at each discrete frequency from the Fourier Transform can be used. Several methods have been proposed to do this. Burcher *et al.* proposed unwrapping the phase at all frequencies, converting the phases to time-delays (by multiplying by $1/f$), and taking the average of the time-delays [13]. This method may be an improvement over the single frequency case, but it can still suffer from

improper unwrapping. Also, since a weighted average was not proposed, it can preferentially apply the time-delays corresponding to small frequency components within the rf-signals relative to the dominant (i.e. transmit) frequency. Prada *et al.* proposed a similar method, except rather than unwrapping the phase directly, the eigenvectors at each frequency were backpropagated to form an image. Then, the images at each frequency were averaged to form the final image [14]. Again this method will suffer from improper weighting of frequency components, as the SVD eigenvectors are orthonormal vectors. Additionally, this approach does not directly give the aberration in a suitable form for the aberration correction method proposed here. It may of course be an alternative method to be explored in the future. A third method was proposed by Kerbrat *et al.* [15]. Recall that an eigenvector is formed at every frequency and there are N components in the eigenvector. Each component corresponds to the a particular element used in the DORT algorithm. Kerbrat *et al.* state that "the first 'temporal eigenvector' $v_1(t)$ is obtained by inverse Fourier transform of [the first eigenvector] $V_1(\omega)$ [at each of the N components]." It is important to recall that all of the eigenvectors are orthonormal and thus have the same magnitude. Therefore it is assumed (though not explicitly stated in [15]) that each frequency of the i^{th} eigenvector was scaled by the i^{th} eigenvalue at the corresponding frequency. If this is not done, then the 'temporal eigenvector' will not appropriately reconstruct the waveform needed to focus at the i^{th} scatterer. This 'temporal eigenvector' was then backpropagated for image formation. For determining aberrations, the N waveforms associated with the i^{th} "temporal eigenvector" were shifted by the temporal location of the maximum of each of the N waveforms. This final approach will be the method followed hereinafter.

A final reason for computing the SVD at all frequencies is that it has been predicted that non-point-scatterers can be characterized by the frequency distribution of the eigenvalues. It has also been predicted that a non-point-scatterer may have

more than one eigenmode associated with it [16; 17].

Isolating Scatterers

For N elements used in DORT, N eigenmodes are obtained. Suppose an image is obtained with a large number of scatterers, or many of the scatterers have multiple eigenmodes. In this case it may be desirable to obtain more than N eigenmodes or it may be that the eigenmode corresponding to the desired scatterer has an eigenvalue smaller than the N^{th} eigenvalue. Methods must be implemented to obtain these additional eigenmodes. For the latter case, one possibility is to apply a time-gain compensation (TGC) or spatial weighting to the rf-data prior to performing DORT. Recall for DORT, the eigenvalues are a product of the scattering amplitude of the object and the amplitude of the insonation frequency. Adjusting the amplitudes of rf-signals is equivalent to changing the insonation beam profile/apodizing the data. The time-gain compensation can be used to emphasize scatterers from a particular depth in the image. Spatial weighting can be applied by proportionally increasing the segments of the rf-lines that correspond to transmitting or receiving nearest the desired lateral location. Since the data is aberrated, the segments that are emphasized need to be sufficiently large to ensure they include the echo from the point-scatterer.

A second approach was proposed by Robert *et al.* [18]. They demonstrate that using just a portion of the data can help to isolate the signal from a particular eigenvector. In doing this, they also show that this can help find eigenmodes that may otherwise be interpreted as noise due to their correlation with neighboring speckle and/or reverberations. In reality, this method is the extreme case of the prior method where the amplitude scaling is either 0 or 1. Figure 3.6b shows the first 'temporal eigenvector' when then entire image data-set is used (fig. 3.6a). Figure 3.6d shows the first 'temporal eigenvector' when only a subset of the data-set is used (fig. 3.6c). While artifacts remain in fig. 3.6d, they are significantly less prominent

than fig. 3.6b.

Spatial Reciprocity

Spatial reciprocity states that the rf-line recorded from transmitting on element i and receiving on element j should be the same as transmitting on element j and receiving on element i. A violation of spatial reciprocity would imply a violation of time-reversal invariance. Therefore, before applying the DORT algorithm, the symmetry in the propagation matrix $\bar{K}(t)$ associated with spatial reciprocity should be checked. This can be done by obtaining the cross-correlation of matrix element $K_{(i,j)}(t)$ with matrix element $K_{(j,i)}(t)$. Figure 3.7a shows the the magnitude of the cross-correlation for each element for the echo from an ADV bubble. Figure 3.7b shows the the magnitude of the cross-correlation for each element for the echo from the same ADV bubble when a physical aberrator is placed between the array and the bubble. The aberrator is a 2D undulating rubber phase screen designed to mimic the aberrations found in the breast and is described in detail by Kruecker *et al.* [19]. It is seen that without the aberrator, there is a high degree of symmetry in the data, though it drops off as the element separation increases. With the aberrator in place however the symmetry is very low. Therefore it might be expected that DORT can be successfully performed on the unaberrated data set but not on the physically aberrated data set.

Figures 3.7c and 3.7d show the synthetic aperture images formed from the data sets analyzed in 3.7a and 3.7b respectively. The reconstructed images used 63 receive channels for each of the 63 transmits for reconstruction. It is clear that the bubble is still seen in the aberrated image, though it's magnitude is diminished and blurred. After applying the DORT algorithm to both data sets, figs. 3.7e and 3.7f show the waveforms associated with the first 'temporal eigenvector'. In the unaberrated case, the waveforms display standard spherical focusing as expected. Although a reverberation-like artifact appears at approximately 18 and 42 μs. The

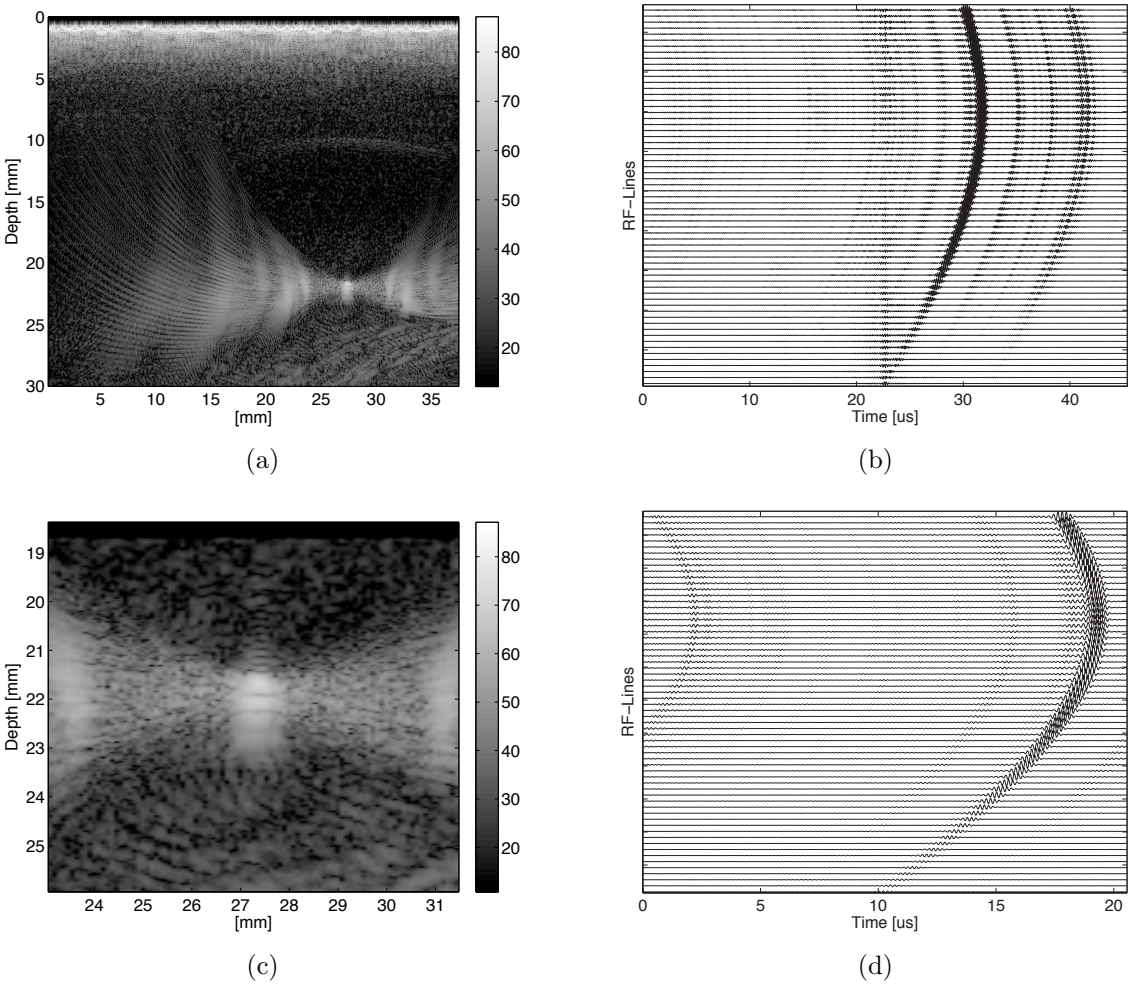

Figure 3.6: (a) SA image of a 110 μm thread in a water tank. (b) The waveforms associated with the first 'temporal eigenvector'. Note that reverberation-like artifacts and noise are present. (c) SA image using a truncated (temporally) data set (that still includes the echo from the thread). Variations in brightness are seen with depth through the echo from the thread. This is due to the thread producing not only a simple reflection, but also echos likely corresponding to additional wave modes of the one-dimensional thread. These waves arrive slightly later in time and thus are reconstructed as echos from deeper in the image. (d) The waveforms associated with the first 'temporal eigenvector' of the subset of the rf-data. Most of the artifacts have been removed. Note also that the additional echos seen in (c) do not appear in the 'temporal eigenvector' (d).

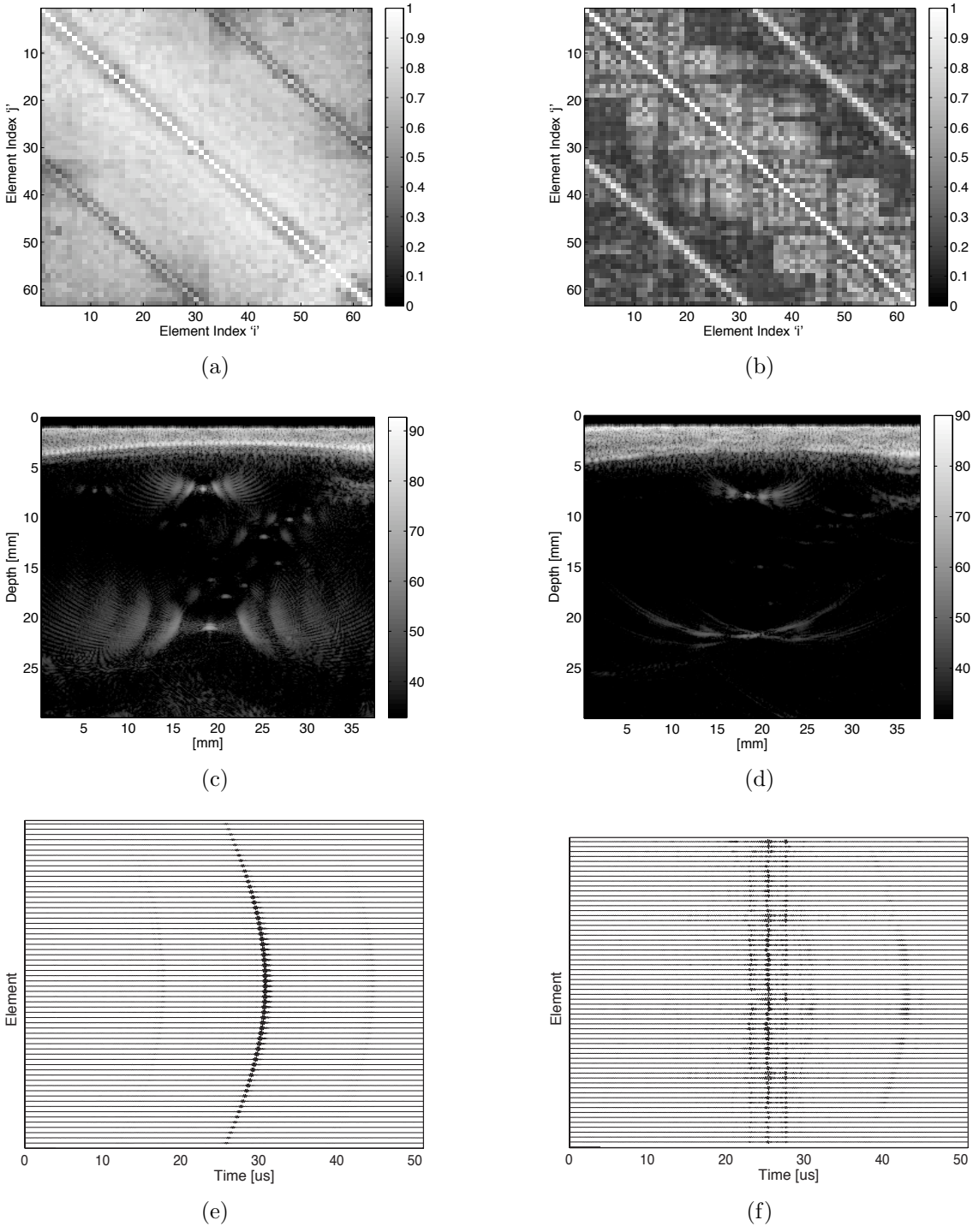

Figure 3.7: Magnitude of the normalized cross-correlation between rf-lines (i,j) and (j,i) from a bubble at a 20 mm depth without an aberrator (a) and with a physical aberrator (b). (c) and (d) are the synthetic aperture reconstructions for the respective data sets (using 63×63 rf-lines for reconstruction). (e) and (f) are the respective waveforms in the first 'temporal eigenvector' of the respsective data sets.

origin of these small artifacts are as yet unknown. In the aberrated case however, the majority of the signal is noise in the form of a flat 'wavefront' halfway through the data. Around 42 μs, the reverberation-like artifact, similar to the unaberrated case, can be seen. This indicates that the DORT algorithm did incorporate the echo from the bubble, but it did so incorrectly. This procedure was repeated for several additional data sets with similar results. This provides evidence that for DORT to run successfully, the data needs to be symmetric with respect to spatial reciprocity.

In an effort to decrease electronic noise, which may be a source for the violation of spatial reciprocity, the rf-data for several frames was averaged together. It was possible to do this because of the static nature of the setup. For a data set composed of three frames, averaging appeared to increase the symmetry slightly, but not significantly. This indicates that it may be a useful solution for future work when the memory capacity of the z.one can be increased to store more IQ data.

An additional step taken to increase the symmetry of the data sets was to decrease the transmit frequency so that the frequency dependent attenuation in the aberrator would be minimized. Using this approach, it was found that DORT could successfully be performed through the aberrator with a 6 MHz transmit frequency, but not at 8.5 MHz, using a 110 μm thread as the scatterer.

3.4 Aberration Corrected Imaging

Due to the acoustic output and frequency limitations of the z.one operating with the L10-5, it is currently not possible to perform aberration correction with the relatively attenuating physical aberrator available. The attenuation destroys the symmetry in the data expected due to spatial reciprocity. Instead, it will be shown that using the previously described methods, it is possible to correct electronic, rather than physically generated, aberrations using an ADV bubble. The electronic aberrations do not produce the SNR reductions that are associated with the attenuating physical

aberrator. Two different setups were employed. In the first setup, polyacrylamide gels with ADV droplets were created according to the specifications of Lo *et al.* [20]. Then using either an imaging transducer with control over acoustic output, or a separate single element transducer, a single bubble was vaporized and used as a point target. In the second setup, a vessel was made from a section of PVC tubing. The open sides of the tube were covered over with plastic wrap (Saran Wrap, S.C. Johnson & Son, Inc, Racine, WI, USA) that is stretched and taped to the sides of the PVC. A hole was drilled into part of the tube to provide access to the vessel. The vessel was then carefully filled with LithoClear ultrasound gel (Sonotech Inc., Bellingham, WA, USA), which is free of micro- and macro-bubbles. A spinal needle was then used to inject droplets into the LithoClear. The droplets were then vaporized and the access port allowed for additional droplets to be added or unwanted ADV bubbles to be removed as described in chapter II.

Synthetic aperture data was collected from the polyacrylamide gel or LithoClear vessel with one or a few ADV bubbles present. The collected data was then processed as described earlier. The DORT algorithm was run and the eigenmode associated with a bubble found. Next, a random time-delay was assigned to each element. The corresponding rf-lines were then shifted based on the time-delays associated with the elements that were used to transmit and receive the particular rf-line. In this manner, a thin near-field phase-screen could be modeled. The DORT algorithm was run on the aberrated data to obtain the eigenmode associated with the bubble. The time-shifts between the unaberrated and aberrated eigenvectors (based on the location of their maximum) were found and compared to the electronic aberrations. They were also used to shift the aberrated data so that it would be aberration corrected. This was performed for a variety of magnitudes of aberrations and it was found that aberrations with a root-mean-square (RMS) time-shift of up to 720 ns could be corrected. This 720 ns RMS is significantly worse than what is typically

found in soft tissue. For example, breast tissue has a typical RMS aberration of 25 to 100 ns [9–12]. Figure 3.8 shows the unaberrated, aberrated, and corrected images. It should be noted that a random DC offset in the phase-error estimates occurs and is not yet understood. Fortunately, a DC offset only corresponds to a global shift of the image and therefore is not a major concern.

To quantify the quality of focusing for each image in fig. 3.8, the focusing factor introduced in chapter II was computed for a 3.3 μs time window of the rf-data centered about the scatter from the bubble at a depth of 22 mm.

$$F = \frac{1}{N} \frac{\int \left(\sum_{i=1}^{N} \psi_i(t) \right)^2 dt}{\sum_{i=1}^{N} \int \psi_i^2(t) dt}$$

The subsets of the rf-data were obtained based on time-of-flight estimates. The waveforms were then detrended (i.e. shifted) relative to the maximum of the unaberrated case to remove the time-shifts associated with different acoustic paths for each element. It was found that the focusing factor for the electronically aberrated data was less than 0.01 and the focusing factor for the aberration corrected data was the same as the unaberrated data, 0.56. This indicates that the aberration correction realigned the waveforms so that they were as coherent as the original unaberrated data.

Theoretically for a point-scatterer, it should be possible to obtain a focusing factor of 1, however this is not accomplished here. First it should be noted that the focusing factor is a measure of the coherent intensity to the incoherent intensity and therefore scales as the square of the signal amplitudes. This accentuates the difference from unity. Figure 3.9 displays 2 subsets of the rf-data used to compute the focusing factor. The right column of plots show the received signals on each element for the case of a transmit element axially above the bubble. The left column

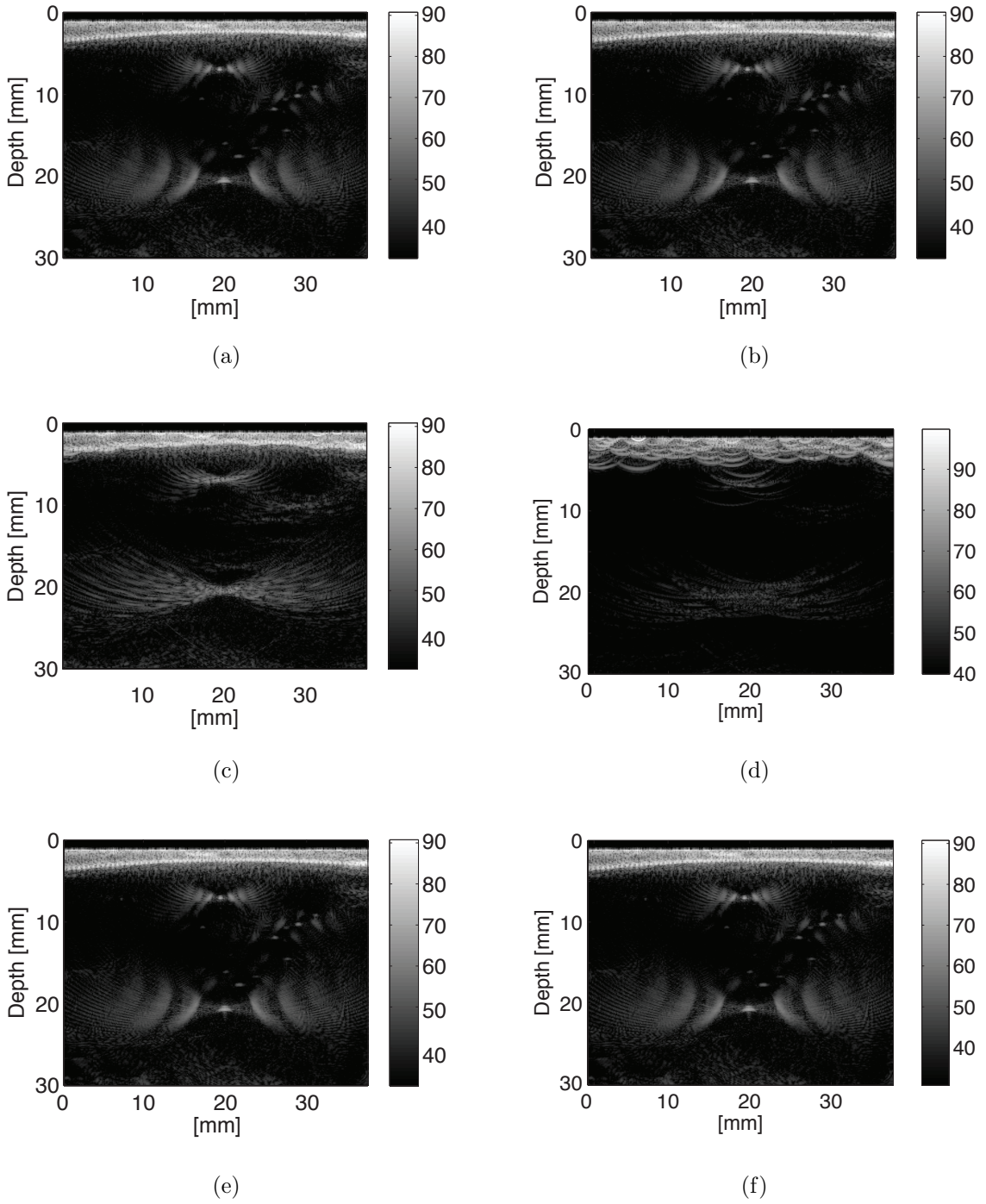

Figure 3.8: (a) and (b) are the original images collected for several ADV bubbles in LithoClear (though two bubbles are most dominant). (c) and (d) are images created after introducing an artificial root-mean-square random time shift of 100 ns and 720 ns, respectively, into the rf-data. The images are clearly aberrated and the bubble is almost indiscernible with the 720 ns RMS time-delays. (e) and (f) are the aberration corrected images using the time-shifts obtained from the first "temporal eigenvector"

of plots show the received signals on each element for the case of a transmit element laterally displaced relative to the bubble. The fall off in amplitude of the rf-data as one moves towards the edge elements of the array indicates that the directivity of the elements is significant. This can also be seen by noting that the amplitudes received when element 15 transmits is smaller than the amplitudes received when element 31 transmits. As a result, the scatter from other objects in the field-of-view becomes more significant. This scatter is uncorrelated to the bubble scatter and therefore decreases the focusing factor. It can also be seen in fig. 3.9 that while the crests and troughs of the waveforms align nicely, several of the waveforms appear to be shifted by a whole wavelength (such as going from receive element 31 to 32 when transmitting on element 15). This is an additional source of reduction for the focusing factor. It is important to note however that these reasons only demonstrate that the focusing factor is an imperfect method of quantifying the focusing on an absolute basis. A relative comparison of the focusing factors was very useful in indicating that the aberration was corrected to the point that it became indistinguishable from the unaberrated case. Visual qualitative assessment should remain the primary method of image analysis.

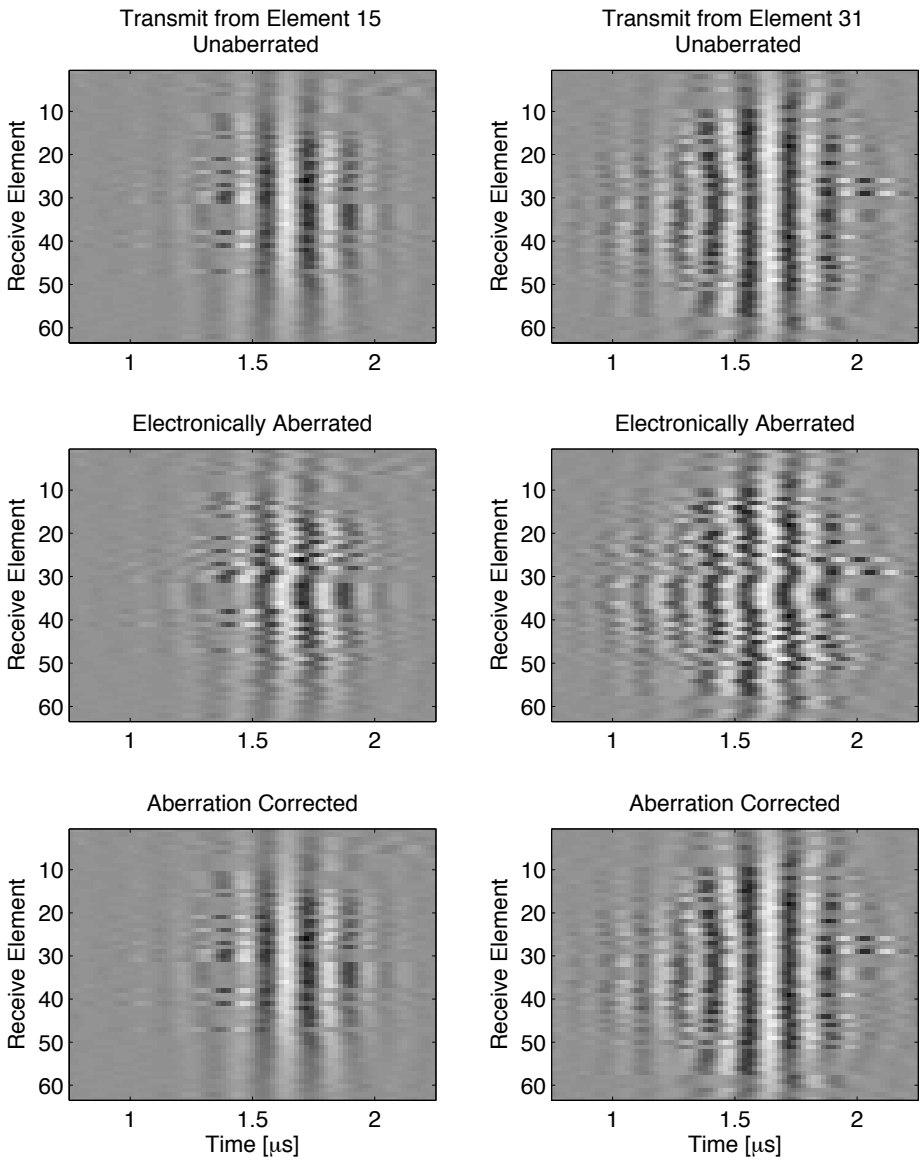

Figure 3.9: Sample subsets of detrended rf-data for transmitting on element 15 (left column) and transmitting on element 31 (right column).

3.5 Conclusions

In this chapter an aberration correction scheme was developed and implemented for imaging. Several practical points were highlighted for successful implementation. Among the most important points was that the data must satisfy spatial reciprocity for the DORT algorithm to be successfully implemented. This requirement limited the ability to perform aberration correction with a physical aberrator and ADV bubble. Using aberrators with lower attenuation may ameliorate this problem. It was also found that transmitting at lower frequencies aided the symmetry of the data. Thus future work with lower frequency arrays is suggested. Additionally, higher output amplitude should improve the data symmetry due to improved SNR. Another approach to increasing the acoustic output would be to transmit coded-excitations, such as chirp pulses [21; 22] or Walsh functions [23; 24], for pulse compression on receive. Prada *et al.* reported that the use of Walsh functions increased the signal-to-noise ratio by approximately 20 dB. These and additional methods of increasing the penetration depth and signal-to-noise ratio for SA algorithms can be found in [6].

Using an electronic aberration correction scheme, it was found that DORT could successfully correct aberrations with an RMS error of more than 700 ns using an ADV bubble. This indicates that with sufficient data symmetry, ADV bubbles can be used to correct for near-field phase screens, even those with very large aberrations. Having demonstrated that aberration corrected imaging is possible with ADV, it now becomes worthwhile to pursue the use of more sophisticated correction algorithms. Prada *et al.* have demonstrated the ability of the MUSIC algorithm to resolve two point-like scatterers separated by $\lambda/3$ [24].

3.6 Acknowledgements

This work was supported in part by NIH grants R01EB000281, R21CA116043, R33CA112144. Additional support was provided as a Rackham Pre-Doctoral Fellowship from the Rackham Graduate School at the University of Michigan.

REFERENCES

[1] C. Prada and M. Fink, "Eigenmodes of the time reversal operator: A solution to slective focusing in multiple-target media," *Wave Motion*, vol. 20, pp. 151–163, 1994.

[2] C. Prada, S. Manneville, D. Spoliansky, and M. Fink, "Decomposition of the time reversal operator: Detection and selective focusing on two scatterers," *Journal of the Acoustical Society of America*, vol. 99, pp. 2067–2076, April 1996.

[3] L. N. Trefethen and D. Bau, *Numerical Linear Algebra*. Society for Industrial and Applied Mathematics, 1997.

[4] J. A. Jensen and N. B. Svendsen, "Calculation of pressure fields from arbitrarily shaped, apodized, and excited ultrasound transducers," *IEEE Transactions on Ultrasonics, Ferroelectrics, and Frequency Control*, vol. 39, no. 2, pp. 262–267, 1992.

[5] J. A. Jensen, "Field: A program for simulating ultrasound systems," *10th Nordic-Baltic Conference on Biomedical Imaging*, vol. 34, no. 1, pp. 351–353, 1996.

[6] J. A. Jensen, S. I. Nikolovikolov, K. L. Gammelmark, and M. H. Pedersen, "Synthetic aperture ultrasound imaging," *Ultrasonics*, vol. 44, pp. e5–e15, 2006.

[7] T. L. Szabo, *Diagnostic Ultrasound Imaging: Inside Out*. Academic Press Series in Biomedical Engineering, 200 Wheeler Road, 6th Floor, Burlington, MA 01803, USA: Elsevier Academic Press, 1 ed., 2004.

[8] J. G. Proakis and D. G. Manolakis, *Digital Signal Processing: Principles, Algorithms, and Applications*. Prentice-Hall, Inc., 3 ed., 1996.

[9] G. E. Trahey, P. D. Freiburger, L. F. Nock, and D. C. Sullivan, "*In Vivo* demonstration of aberration correction using acoustic droplet vaporization measurements of ultrasonic beam distortion in the breast," *Ultrasonic Imaging*, vol. 13, no. 1, pp. 71–90, 1991.

[10] P. D. Freiburger, D. C. Sullivan, B. H. LeBlanc, S. W. Smith, and G. E. Trahey, "Two dimensional ultrasonic beam distortion in the breast: *In vivo* measurements and effects," *Ultrasonic Imaging*, vol. 14, no. 4, pp. 398–414, 1992.

[11] L. M. Hinkelman, D.-L. Liu, R. C. Waag, Q. Zhu, and B. D. Steinberg, "Measurement and correction of ultrasonic pulse distortion produced by the human breast," *Journal of the Acoustical Society of America*, vol. 97, no. 3, pp. 1958–1969, 1995.

[12] R. C. Gauss, M. S. Soo, and G. E. Trahey, "Wavefront distortion measurements in the human breast," *IEEE Ultrasonics Symposium*, vol. 2, pp. 1547–1551, 1997.

[13] M. Burcher, A. T. Fernandez, and C. Cohen-Bacrie, "A novel phase aberration measurement technique derived from the DORT method: Comparison with correlation-based method on simulated and *in-vivo* data," *IEEE Ultrasonics Symposium*, vol. 1, pp. 860–865, 2004.

[14] C. Prada, J. de Rosny, D. Clorennec, J.-G. Minonzio, A. Aubry, M. Fink, L. Berniere, P. Billand, S. Hibral, and T. Folegot, "Experimental detection and focusing in shallow water by decomposition of the time reversal operator," *Journal of the Acoustical Society of America*, vol. 122, pp. 761–768, August 2007.

[15] E. Kerbrat, C. Prada, D. Cassereau, and M. Fink, "Imaging in the presence of grain noise using the decomposition of the time reversal operator," *Journal of the Acoustical Society of America*, vol. 113, pp. 1230–1240, March 2003.

[16] D. H. Chambers and A. K. Gautesen, "Time reversal for a single spherical scatterer," *Journal of the Acoustical Society of America*, vol. 109, no. 6, pp. 2616–2626, 2001.

[17] D. H. Chambers, "Analysis of the time-reversal operator for scatterers of finite size," *Journal of the*, vol. 112, pp. 411–421, May 2002.

[18] J.-L. Robert, M. Burcher, C. Cohen-Bacrie, and M. Fink, "Time reversal operator decomposition with focused transmission and robustness to speckle noise: Application to microcalcification detection," *Journal of the Acoustical Society of America*, vol. 119, pp. 3848–3859, June 2006.

[19] J. F. Kruecker, G. L. LeCarpentier, J. B. Fowlkes, and P. L. Carson, "Rapid elastic image registration for 3-D ultrasound," *IEEE Transactions on Medical Imaging*, vol. 21, pp. 1384–1394, November 2002.

[20] A. H. Lo, O. D. Kripfgans, P. L. Carson, and J. B. Fowlkes, "Spatial control of gas bubbles and their effects on acoustic fields," *Ultrasound in Medicine and Biology*, vol. 32, no. 1, pp. 95–106, 2006.

[21] Y. Takeuchi, "An investigation of a spread energy method for medical ultrasound systems: Part one: Theory and investigation," *Ultrasonics*, vol. 17, p. 175, 182 1979.

[22] M. O'Donnell, "Coded excitation systems for improving the penetration of real-time phase-array imaging systems," *IEEE Transactions on Ultrasonics, Ferroelectrics, and Frequency Control*, vol. 39, no. 3, pp. 341–351, 1992.

[23] S. Azzaretti, D. Dotti, R. Lombardi, and D. Rossi, "Echo-graphic images enhanced through Walsh functions," *IEEE Ultrasonics Symposium*, vol. 1, pp. 675–678, 1997.

[24] C. Prada and J.-L. Thomas, "Experimental subwavelength localization of scatterers by decompstion of the time reversal operator interpreted as a covariance matrix," *Journal of the Acoustical Society of America*, vol. 114, pp. 235–243, July 2003.

CHAPTER IV

Generalized Shot Noise Model for Time-Reversal in Multiple-Scattering Media Allowing for Arbitrary Inputs and Windowing

4.1 Introduction

Parvulescu and Clay performed the first time-reversal acoustic (TRA) experiments in 1965 [1]. In the following two decades however, relatively little work was performed in TRA. Beginning approximately fifteen years ago however, there has been a burst of activity, led in large part by Prof. Mathias Fink. Over this time, nearly all of the TRA experiments can be described by the general process of sending a short pulse into a medium and recording the resulting wave $s(t)$. The recorded signal is time-reversed $s(t) \rightarrow s(-t)$ (and possibly processed) and then retransmitted into the medium. The resulting time-reversal focused signal is recorded and analyzed.

One area of TRA that has shown both surprising and fruitful results is the time-reversal of waves that have travelled through random high-order multiple-scattering environments. Traditionally, random multiple-scattering environments display chaotic behaviors that prohibit focusing through them. Propagating waves through a "forest-of-needles" to a point receiver and then time-reversing this signal and showing that it would refocus at its origin was the first demonstration of the ability to focus through this type of medium [2]. Surprisingly, it was found that the focused signals were even more well defined after going through the multiple-scattering

medium than if focusing was performed in a homogenous medium [2]! These results were extended to other high-order multiple-scattering environments such as a chaotic cavity, where the boundaries of a reverberant material scattered the sound [3]. Various approaches have been taken to describe the unexpected results of TRA in multiple-scattering media. This chapter is concerned with generalizing the approach first developed by Derode *et al.* [4] to explain this phenomena. This approach treats the multiple-scattering events via a shot noise model. The shot noise approach allowed Derode *et al.* [4] to successfully model one-bit time-reversal. It has also been used to determine the impact of windowing a signal before performing time-reversal [5]. Others have also extended the shot noise model to incorporate additional phenomena, such as scattering dependencies in "forest-of-needle" experiments [6]. In addition to the shot noise approach other approaches have used scattering theory [7–9], eigenmode decomposition [3], and Green's Functions [10]. Each of which makes different assumptions and elucidates different effects (e.g. coherent backscatter [9], noise emission in time-reversal [11], etc.).

The primary motivation for the development of this generalized model is to predict the signal-to-noise ratio for future time-reversal chaotic cavity (TRCC) experiments (though other applications may be found, as illustrated below). In particular for cases where one is interested in transmitting signals besides delta-functions, such as the long tone-bursts associated with high-intensity focused ultrasound for heating or acoustic radiation force experiments. TRCCs were first introduced by Fink and colleagues [3; 12; 13]. TRCC experiments traditionally work by having a transducer transmit an acoustic/elastic pulse into a solid (typically a metal). The sound reverberates within the cavity, reflecting off of the solid's walls. The acoustic signal at any point within the cavity can quickly become a diffuse wave. If the diffuse wave is recorded, time-reversed, and retransmitted, the waves will approximately retrace their paths and focus at the transducer that originally transmitted the pulse.

The initial experiments by Draeger and Fink measured elastic waves in a 2D silicon wafer. Quieffin *et al.* [14] showed that this concept could be extended to 3D solids and more importantly that if the solid were put into contact with a water bath, signal would leak out of the solid and could be recorded with a hydrophone in the water. Then using spatial reciprocity, they showed that if the signal recorded by the hydrophone was time-reversed and retransmitted by the original transducer, a pulse would focus on the hydrophone's location outside of the cavity. The location of the hydrophone could be varied and thus it was found that TRCCs allowed focusing throughout a 3D volume with as few as one ultrasound transducer. Additional work by Fink and colleagues has lead to prototypes for imaging devices [15] and high amplitude ultrasound therapy devices [16], among other applications. Since the initial development of TRCCs, Sarvazyan and colleagues have also made significant progress in understanding and utilizing TRCCs [17–19].

Modeling of high-order multiple-scattering TRA has found other applications. These include biomedical engineering [20], non-destructive testing and evaluation [21; 22], geophysics [23–25], underwater acoustics [26], imaging [27; 28], and (wireless) communication [29–31]. In many of these applications, one may be interested in sending not just a short pulse through the multiple-scattering medium, but an extended pulse that could be used to contain extensive information or induce an effect. In this chapter, the model initiated by Derode *et al.* [4] is generalized to account for arbitrary input functions and arbitrary windowing. The goal of the model is to compute the expectation value and variance of a time-reversal focused signal through a multiple-scattering medium.

This chapter is organized as follows. Section 4.2 provides the general theory. This includes outlining the problem in greater detail (section 4.2.2), deriving the expectation value (section 4.2.3), variance (section 4.2.4), and directivity pattern (section 4.2.6), and providing some physical (section 4.2.1) and numerical support

(section 4.2.5) for the model. In section 4.3 a set of common parameters is then applied to these general results, allowing the expectation value (section 4.3.1) and variance (section 4.3.2) to be simplified. The SNR under these conditions is also derived and discussed (section 4.3.3).

4.2 General Theory

In order to lay a complete foundation for the shot noise model, it will be built up from the general class of processes to which it belongs, stochastic processes.

4.2.1 Background

Stochastic Processes

A stochastic process is often described as a random process. The arguments of Papoulis [32] will be used to provide a firmer definition.

A stochastic process can be viewed as a function of two variables $(t;\eta)$. η represents the possible outcomes of the sample space and t is a real number used to describe the outcome of the stochastic process. In other words, for a given outcome η_o the stochastic process is a particular function of t. As a concrete example let $\mathbf{x}(t;\eta)$ represent the stochastic process which is described by a coin-tossing experiment (a boldface font will be used to denote a stochastic processes in this introductory section). In this case, the outcomes of the sample space are *heads* or *tails*, i.e. η is either *heads* or *tails*. $\mathbf{x}(t;\eta)$ will be defined as:

$$\mathbf{x}(t;\eta) = \begin{cases} sin(t) & \text{if } \eta = \text{heads}, \\ 2t & \text{if } \eta = \text{tails}. \end{cases} \tag{4.1}$$

In this case, the stochastic process $\mathbf{x}(t;\eta)$ consists of two very regular curves, but it is stochastic in nature due to the random outcome of the coin-toss. In general there are four categories that a stochastic process can fall into [32, pg 205]:

1. A family of time functions (both t and η are variables)

2. A single function (t is a variable but η is fixed)

3. A random variable (t is fixed but η is a variable)

4. A single number (both t and η are fixed)

Note that there is no requirement that $\mathbf{x}(t;\eta = \text{constant})$ be a regular function. It can be a complicated function itself that is not easily described in closed form. For example $\mathbf{x}(t;\eta = \text{constant})$ may describe the irregular motion of a particle in fluid (Brownian motion) based on the initial random placement of the particle in the fluid (where the placement is the outcome and the sample space is all locations in the fluid).

Poisson Processes

A particular stochastic process that is important for time-reversal chaotic cavities is the Poisson process. It can be defined on its own, however, here it will introduced as a limit of a binomial process. Suppose the sample space is an interval $(0, T)$ and the possible outcomes are either the random selection of a point within a particular subset (t_1, t_2) of the interval $(0, T)$ or the random selection of a point outside the particular subset (t_1, t_2) of the interval $(0, T)$. For this process if one selects "at random" n points in the interval $(0, T)$, what is the probability that k of these points will lie in the subset interval (t_1, t_2) [32, pg. 55]? This can be identified as being a series of n binomial events with a positive event being the placement of a point in the interval (t_1, t_2). The probability of success is $p = \frac{t_2 - t_1}{T}$. Based on the binomial distribution the probability that k out of n points will lie in the interval (t_1, t_2) will be:

$$P\{k \text{ out of } n \text{ points in the interval } (t_1, t_2)\} = \binom{n}{k} p^k (1-p)^{n-k}. \tag{4.2}$$

If the number of events n is large ($n \gg 1$) and the probability of a successful event is small (i.e. $\frac{t_2-t_1}{T} \ll 1$), then for k on the order of $\frac{n(t_2-t_1)}{T}$ the binomial distribution is well approximated by a Poisson distribution.

$$P\{k \text{ out of } n \text{ points in the interval } (t_1, t_2)\} \approx e^{-n\frac{t_2-t_1}{T}} \frac{(n\frac{t_2-t_1}{T})^k}{k!} \tag{4.3}$$

$$= e^{-\lambda(t_2-t_1)} \frac{(\lambda(t_2-t_1))^k}{k!}, \tag{4.4}$$

where $\lambda = \frac{n}{T}$ is the density of events.

A Poisson process $\mathbf{x}(t)$ is then defined as a process that counts the number of points in an interval $(0, t < T)$ when the probability of having k points in any subinterval (t_1, t_2) is described by the Poisson distribution (eqn. 4.4). The plot of a Poisson process $\mathbf{x}(t)$ looks like an irregular staircase. Mathematically it can be described as:

$$\mathbf{x}(t) = \int_0^t \sum_{i=-\infty}^{\infty} \delta(t - t_i)dt - \mathbf{x}(0), \tag{4.5}$$

where $\delta(t)$ is the dirac-delta function and t_i follows the distribution described by eqn. 4.4. Note that this fits into the first definition of a stochastic process outlined above. It is a family of time functions where t_i plays the role of η in section 4.2.1.

Shot Noise

The stochastic process $\mathbf{z}(t)$ that is described by the derivative of $\mathbf{x}(t)$ with respect to time is called a Poisson impulse process:

$$\mathbf{z}(t) = \frac{d\mathbf{x}(t)}{dt}. \tag{4.6}$$

A shot noise process is one which is described as:

$$\mathbf{h}(t) = \mathbf{z}(t) \otimes h_{ae}(t) \tag{4.7}$$

$$= \sum_{i=-\infty}^{\infty} h_{ae}(t - t_i), \tag{4.8}$$

where one can recognize that $\mathbf{z}(t)$ is just a series of Poissonian distributed dirac-delta functions.

The impulse response $\mathbf{h}(t)$ of a time-reversal chaotic cavity can now be recognized as a shot noise process. Rather than selecting points on an interval, an event is described by each random arrival of a pulse $\mathbf{h}_{ae}(t)$ (the acousto-electric impulse response) that has traveled along one of the many different paths (in a ray-acoustic approach) or modes (in a wave-acoustic approach) of the cavity. Since there are many possible paths/modes (i.e. $n \gg 1$) and if one looks at a small interval (i.e. $\frac{t_2 - t_1}{T} \ll 1$), then the distribution of arrival times t_i is Poissonian for any subset interval. For a high-density shot noise process, the central limit theorem says that the Poisson distribution is well approximated by a Gaussian distribution. Properties of Gaussian distributions are well known, which will make it easier to compute the statistical model.

Experimental Validation of Shot Noise Assumptions

To further motivate the use of a shot noise model, the impulse response was experimentally obtained from a time-reversal chaotic cavity (Imasonic SAS, Besançon, France) constructed to be the same as the one used by Montaldo *et al.* [16]. The impulse response was obtained by driving one of the elements on the TRCC with a step function generated from an HP33120A function generator (Agilent, Palo Alto, CA, USA) and amplified by an ENI A-300 rf power amplifier (Rochester, NY, USA). The face opposite the elements was placed in a water tank and a hydrophone (PVF_2, Raytheon Co., Waltham, MA, USA) recorded the signal transmitted into

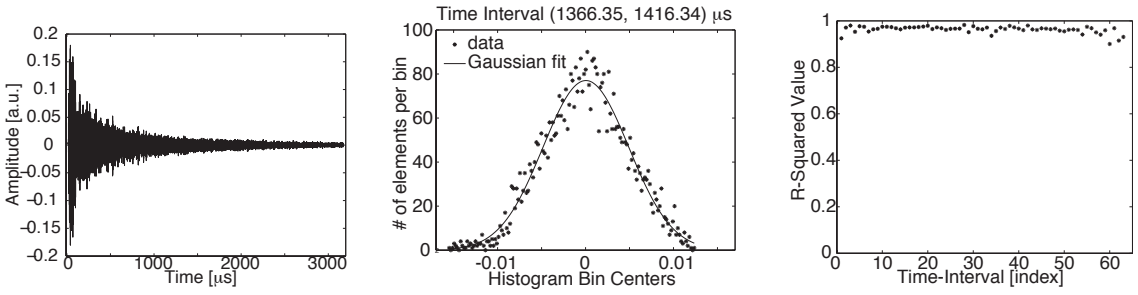

(a) (b) (c)

Figure 4.1: (a) Experimentally obtained impulse response for a time-reversal chaotic cavity. (b) Example of a histogram of the amplitudes for an arbitrarily chosen interval and its Gaussian fit. (c) R^2 values indicating that the amplitudes in each 50 μs time interval of the impulse response are well modeled as normal random variables.

the water. The impulse response (IR) (fig. 4.1a) of the cavity was recorded with a hydrophone and broken into 50 μs time-intervals. If the IR can be modeled as a normal random variable, then the amplitudes within each time-interval should have a Gaussian distribution. To determine if this is true, the amplitudes in each interval were plotted in a histogram. The histogram was then fit to a Gaussian function $Ae^{\frac{(x-\mu)^2}{2\sigma^2}}$ (4.1b) and the R-squared value (i.e. square of the Pearson product-moment correlation coefficient) computed to determine the goodness-of-fit. Figure 4.1c shows that the computed R-squared values are indeed all close to one, indicating that the Gaussian model can be used as an adequate approximation of the data.

While it has been demonstrated that the assumptions used for the shot noise model are valid for a specific case, the derivations that follow should hold for any high-order multiple-scattering process that satisfy the assumptions made above. In fact, the derivation is not necessarily specific to acoustic waves and could be applied to any wave phenomena where phase coherent detectors with reversible signals exist or are developed (e.g. radio frequency electromagnetic waves). The results of the derivations will be compared to a random number numerical simulation, rather than a physical experiment or a numerical simulation based on the wave equation. Others have shown that the shot noise model does describe physical results of time-reversal

focusing under various particular conditions.[5; 6]

4.2.2 Time-Reversal Focused Signal

The generic time-reversal experiment that will be modeled occurs as follows. An input signal $g(t)$ is transmitted into the scattering medium, which has an impulse response $h(t)$. The resulting output signal $g(t) \otimes_t h(t)$ is recorded (where $\otimes_t$ is a convolution over time t). A window-function $W(t)$ is applied to the output signal, which is then normalized by its maximum value $\mathbf{M}$:

$$\frac{1}{\mathbf{M}} W(t) \cdot (g(t) \otimes_t h(t)). \tag{4.9}$$

The window function selects the desired portion of the total output signal that will be used in the time-reversal experiment. The windowed function is then time-reversed ($t \to -t$) with a temporal shift of T to ensure causality, yielding:

$$\frac{1}{\mathbf{M}} W(T-t) \cdot (g(-t) \otimes_t h(T-t)). \tag{4.10}$$

Appendix A demonstrates that the above is the appropriate method of writing out a time-reversed and shifted convolution. The time-reversed function is now retransmitted into the medium resulting in the signal:

$$r(t) = \left(\frac{1}{\mathbf{M}} W(T-t) \cdot \Big(g(-t) \otimes_t h(T-t) \Big) \right) \otimes_t h(t). \tag{4.11}$$

The expectation value and variance of this signal will be computed.

4.2.3 Expectation Value

As Derode *et al.* [4] show, even though $\mathbf{M}$ is a random variable, because of its origins in $g(t) \otimes h(t)$, it is approximately constant and thus can be pulled out of the expectation integral. As such it will now be denoted as M. An approximation

for M can be found in appendix B. To compute the expectation value of eqn. 4.11, the convolutions are written as integrals (see appendix A for derivations on how to properly convert nested, time-reversed, and time-shifted convolutions). The integration variables for the convolutions are θ_t and τ_θ. The functional variable associated with each convolution is t and θ, respectively.

$$E\{r(t)\} \approx \frac{1}{M} E\left\{ \left(W(T-t) \cdot \Big(g(-t) \otimes_t h(T-t) \Big) \right) \otimes_t h(t) \right\} \tag{4.12}$$

$$= \frac{1}{M} E\left\{ \left(W(T-t) \cdot \int_{\tau=-\infty}^{\infty} g(-\tau) h(T-(t-\tau))\, d\tau \right) \otimes_t h(t) \right\} \tag{4.13}$$

$$= \frac{1}{M} E\left\{ \int_{\theta_t=-\infty}^{\infty} \left(W(T-\theta_t) \cdot \int_{\tau_\theta=-\infty}^{\infty} g(-\tau_\theta) h(T-(\theta_t-\tau_\theta))\, d\tau_\theta \right) h(t-\theta_t)\, d\theta_t \right\} \tag{4.14}$$

Since $h(t)$ defines a stochastic process with a normal probability density function $f(h(t))$, the expectation value of $r(t)$ can be computed as:

$$E\{r(t)\} = \int_{h(t)=-\infty}^{\infty} [r(t;h(t)) \cdot f(h(t))]\, dh(t). \tag{4.15}$$

Using this notation, eqn. 4.14 is first rewritten expressing the expectation value as an integral. The integrals are then reordered, making the integral over $h(t)$ the innermost integral, and finally rewriting that integral in the $E\{\bullet\}$ notation:

$$E\{r(t)\} \approx \frac{1}{M} \int_{\tau_\theta=-\infty}^{\infty} \int_{\theta_t=-\infty}^{\infty} g(-\tau_\theta)\, W(T-\theta_t) E\big\{ h(T-(\theta_t-\tau_\theta)) h(t-\theta_t) \big\} d\theta_t d\tau_\theta. \tag{4.16}$$

Now all constants with respect to the stochastic process $h(t)$ have been removed from the expectation value. As was described above, $h(t)$ is a normal random variable with mean zero and variance $\sigma^2(t)$. The expectation value of two such normal random variables multiplied together is [32]:

$$E\{\mathbf{x}(t_1) \cdot \mathbf{y}(t_2)\} = \rho(t_1 - t_2) \cdot \sigma_x(t_1) \cdot \sigma_y(t_2), \tag{4.17}$$

where $\rho(t_1 - t_2) = \rho(t_2 - t_1)$ is the correlation coefficient of the normal random variables $\mathbf{x}(t_1)$ and $\mathbf{y}(t_2)$, and $\sigma_x(t_1)$ and $\sigma_y(t_2)$ are the standard deviations of $\mathbf{x}(t_1)$ and $\mathbf{y}(t_2)$, respectively. Applying this and rewriting the integrals in traditional convolution notation yields:

$$\begin{aligned} E\{r(t)\} \approx & \frac{1}{M} \int_{\tau_\theta=-\infty}^{\infty} g(-\tau_\theta) \cdot \rho(T-(t-\tau_\theta)) \times \\ & \left(\int_{\theta_t-\infty}^{\infty} W(T-\theta_t)\sigma(T-(\theta_t-\tau_\theta))\sigma(t-\theta_t)\, d\theta_t \right) d\tau_\theta \end{aligned} \tag{4.18}$$

$$\begin{aligned} = & \frac{1}{M} \int_{\tau_t=-\infty}^{\infty} g(-\tau_t)\rho(T-(t-\tau_t)) \times \\ & \left(\Big(W(T-t)\sigma(T-(t-\tau_t)) \Big) \otimes \sigma(t) \right) d\tau_t \end{aligned} \tag{4.19}$$

$$E\{r(t)\} \approx \frac{1}{M} g(-t) \otimes \left[\rho(T-t) \left(\Big(W(T-t) \cdot \sigma(T-t) \Big) \otimes \sigma(t) \right) \right]. \tag{4.20}$$

Equation 4.20 is the statistical approximation for the expectation value of the time-reversal focused signal. Note that it is non-zero only for a duration approximately as long as the input function $g(t)$. This time with non-zero amplitude will be referred to as the main lobe of the signal and all times outside this as side lobes. Looking at the square bracket term, one sees that a rapidly oscillating function $\rho(T-t)$ is multiplied by a relatively slow changing function $\Big(W(T-t) \cdot \sigma(T-t) \Big) \otimes_t \sigma(t)$ (assuming the window function is not rapidly changing). As a result, the term in the square brackets will look approximately like a scaled version of $\rho(T-t)$. Therefore, how large this term is, and thus how large $E\{r(t)\}$ is, can be estimated by a convolution involving the envelope the window. Therefore the result found by others that the expected signal increases as the integrated amplitude of the envelope of the impulse response (or time-reversed signal in the case of one-bit time-reversal) increases is confirmed [4; 5; 33]. Equation 4.20 is easily shown to simplify to the corresponding result of Derode *et al.* [4] (term 1 of eqn. A2) by letting the window extend to positive and negative infinity (i.e. $W(t) = 1 \ \forall \ t$),

setting $T = 0$, and letting $g(t) \to \delta(t)$.

4.2.4 Variance

Since the variance can be computed from $\mathrm{VAR}\{r(t)\} = E\{r^2(t)\} - E^2\{r(t)\}$, the process is similar to what was done in the previous section. However, the mathematics are more tedious due to the squaring of $r(t)$. Therefore the variance is computed in appendix C. The result is:

$$\begin{aligned}\mathrm{VAR}\{r(t)\} = &\left(\frac{1}{M^2} \int_{\theta_1=-\infty}^{\infty} \int_{\theta_2=-\infty}^{\infty} W(T-\theta_1) W(T-\theta_2) \sigma^2(t-\theta_1) \sigma^2(t-\theta_2) \times \right. \\ &\left[g(-\theta_1) \otimes_{\theta_1} \rho(T - \theta_1 - (t-\theta_2)) \right] \times \\ &\left. \left[g(-\theta_2) \otimes_{\theta_2} \rho(T - \theta_2 - (t-\theta_1)) \right] \, d\theta_2 \, d\theta_1 \right) + \\ &\left(\frac{1}{M^2} \int_{\theta_1=-\infty}^{\infty} W(T-\theta_1) \sigma(t-\theta_1) \left[\sigma(t) \otimes_t \left\{ W(T-t) \rho(t-\theta_1) \times \right. \right. \right. \\ &\left. \left. \left. \left[g(-\theta_1) \otimes_{\theta_1} \left\{ \sigma^2(T-\theta_1) \Big[g(-t) \otimes_t \rho(t-\theta_1) \Big] \right\} \right] \right\} \right] \, d\theta_1 \right). \end{aligned} \tag{4.21}$$

Each of these terms can be related to the physical processes occurring in multiple-scattering. The nature of the symmetry of the square brackets in the first term indicates that this term only contributes at the main lobe and is zero outside of it. This is seen in plotting this termp (top plot of fig. 4.2). This term comes from variations in the total energy contained in the time-reversed signal that is transmitted into the medium. That is, it originates from the variance in the total energy in the time-reversed signal over different realizations of multiple-scattering processes (i.e. a reordering of the scatterers or placement of the sound source). Note that on average the energy will be the same for a particular interval and conservation of energy dictates that the total energy in $h(t)$ over all time will be constant. However, over different realizations of the multiple-scattering environment, the distribution of energy will change, even for the same time interval. Due to this,

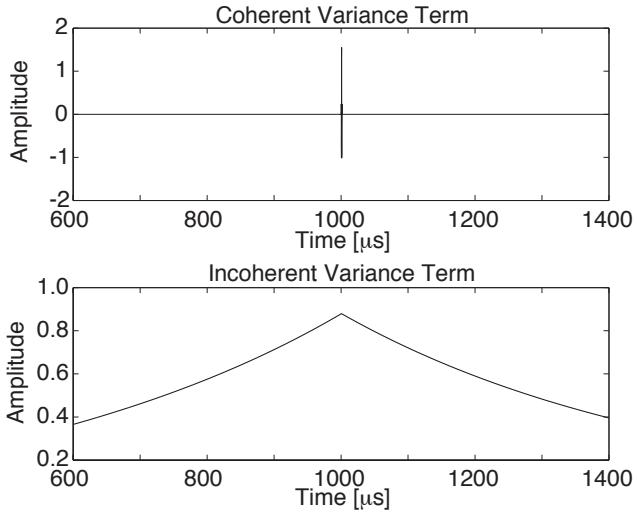

Figure 4.2: Each term of the variance plotted separately. (top) The coherent variance is is a short burst that only lasts for the duration of the input waveform. (bottom) The incoherent variance has a duration that is as long as the time-reversed and transmitted signal pulse the nominal length of the impulse response

the first term will be referred to as the coherent or correlated variance. To minimize this variance, one might ensure that the wave is completely diffuse or try to include a larger portion of the signal when time-reversing. Further changes that can be made to reduce this term are outlined in section 4.3.

The second term is the bottom plot of fig. 4.2. It is due to the interference of the time-reversed signal and $h(t)$ at all times when the two waveforms are uncorrelated. Thus one can refer to this term as being the incoherent or uncorrelated variance. To maximize the main lobe to side lobe ratio (a possible SNR definition) one would be interested in minimizing the second term while maximizing the expectation value. Alternatively, for a more consistent main lobe amplitude, the first term should be minimized.

4.2.5 Comparison of Derived Model with Numerical Simulation

In addition to verifying the equations by showing their reduction to previously obtained results, the equations were also compared to ensembles of simulated data as was done by Derode *et al.* [4]. The simulated data was created from a normally distributed random array (created using the `randn` function in MATLAB (The Mathworks, Inc., Natick, MA, USA), which is based on the Ziggurat algorithm [34] that has a period of approximately 2^{64}) convolved with a normalized 3.5-cycle sine-wave to simulate $h(t)$, where the 3.5-cycle sine-wave models an acousto-electrical impulse response. $h(t)$ was then convolved with $g(t)$ (chosen as a delta function for this simulation), windowed and time-reversed. The result was then convolved with the original $h(t)$ to give a simulated realization of $r(t)$. The mean and standard deviation of an ensemble of 500 simulated $r(t)$ (each with a unique $h(t)$) were plotted against the analytical solution for $\mathrm{E}\{r(t)\}$ (eqn. 4.20) and the square root of the $\mathrm{VAR}\{r(t)\}$ (eqn. 4.21) (fig. 4.3). The figures demonstrate that the model accurately predicts the numerical simulation. R^2 values quantifying the goodness-of-fit are shown for each plot.

Based on the equations derived for the expectation value and variance and fig. 4.3, one can draw conclusions for how various parameters will impact the time-reversal focusing. Initially, if one focuses on figs. 4.3b and 4.3c it is possible to see the impact of the decay constant of the envelope of the impulse response. As one would physically expect, both the variance and the expectation value increase as the decay constant increases. This is due to the fact that there is more energy in the time-reversed signal. Also, one can see that the side lobes fall off more slowly as the time constant increases. The extrapolation of this result has been seen for one-bit time-reversal, where the side lobes are approximately constant in amplitude [4] and is consistent with the physical explanation of the incoherent variance given

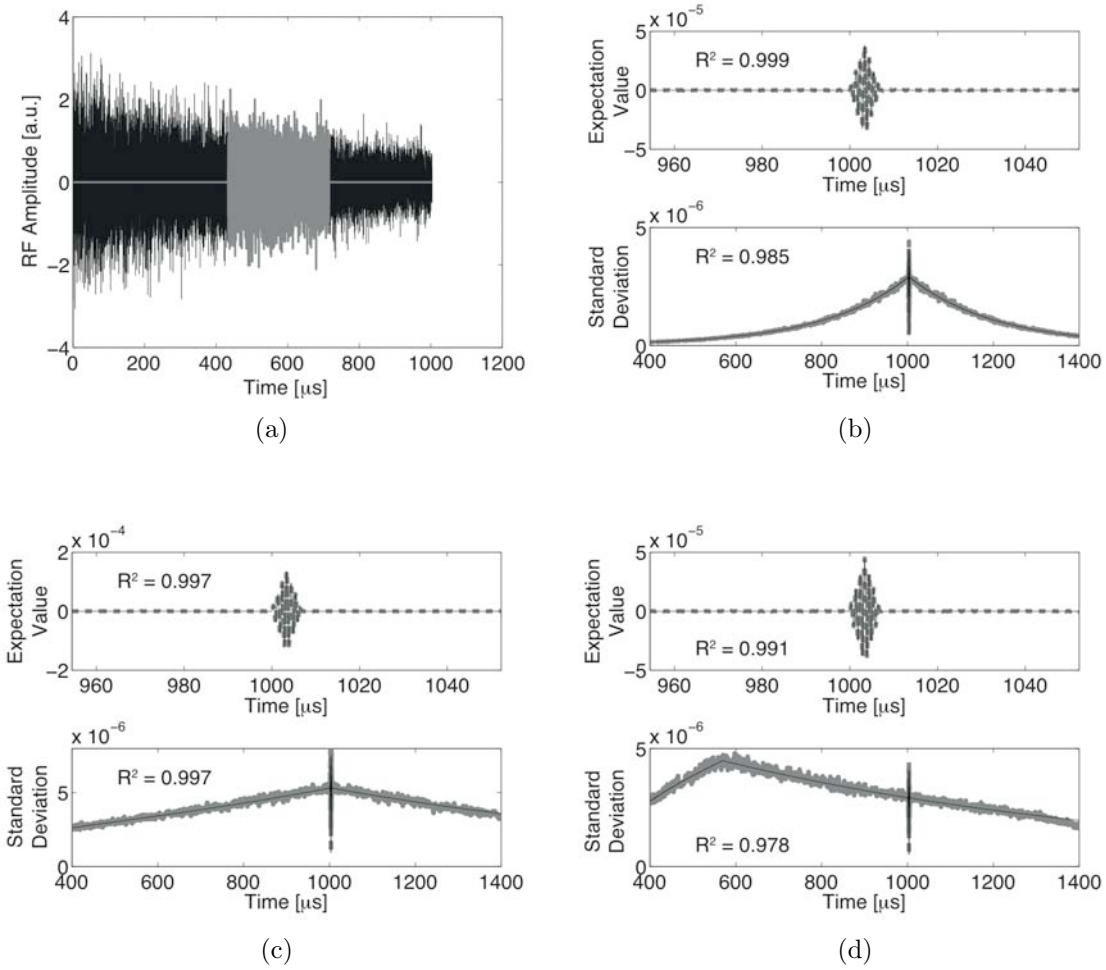

Figure 4.3: (a) Numerically simulated impulse response (IR) with the gray section corresponding to the windowed portion used for subfigure (d). Subfigures (b) − (d) compare the expectation/mean value (top plots) and standard deviation (i.e. square root of the variance) (lower plots) for the statistical model (black line) and numerical simulation (gray line). (b) Time-reversal focusing of the full IR shown in (a). (c) Time-reversal focusing of a full IR with a slower decay than the one shown in (a). (d) Time-reversal focusing of the windowed (gray) portion of the IR in (a). R^2 values are given for each plot demonstrating that the model is a good fit to the numerical simulation.

earlier. Next, the impact of shifting the window to later times can also be seen (fig. 4.3c and 4.3d). Looking at the expectation value, one sees that its maximum amplitude has decreased for fig. 4.3d. This is expected for two physical reasons. First, since the signal is windowed, the signal that is retransmitted has less total energy. Additionally, this signal correlates with the impulse response at a later time, when the impulse response has decreased in amplitude. Thus the amplitude of the correlation of the signals (which is essentially what the time-reversal process does) is smaller. Analogous reasoning also leads to explaining why the coherent variance is seen to be smaller. For subfigures (b) - (d), the shape of the incoherent portion of the side lobes initially increases in all cases as more of the time-reversed signal is transmitted and incoherently interferes with the impulse response. The magnitude of this interference is roughly the product of the overlap of the time-reversed signal with the envelope of the impulse response. Once the entire time-reversed signal has been transmitted and no more energy is being injected into the system, the incoherent interference peaks and then decreases as the magnitude of the impulse response falls off with time. Thus for a delayed window, such as fig. 4.3d, the incoherent interference peaks and begins to fall off before the time-reversed signal has lined up and coherently interferes with the impulse response. This is seen pictorially in fig. 4.4. Hence, the variance peaks around 600 μs with the expectation value peak not occuring until 1050 μs. This should always be seen whenever the window zeros out the initial part of the recorded signal $g(t) \otimes_t h(t)$. Note that the shape of the side lobes after the peak should fall off like $\sigma(t)$, while the shape before the peak will be more complicated and depend on both $g(t)$ and $\sigma(t)$. Further trends for changing parameters will be investigated more closely in section 4.3.

4.2.6 Directivity Pattern

To estimate the directivity pattern, the same process as above will be used, however the impulse response will be specific to a particular location x_o. As a result, equation

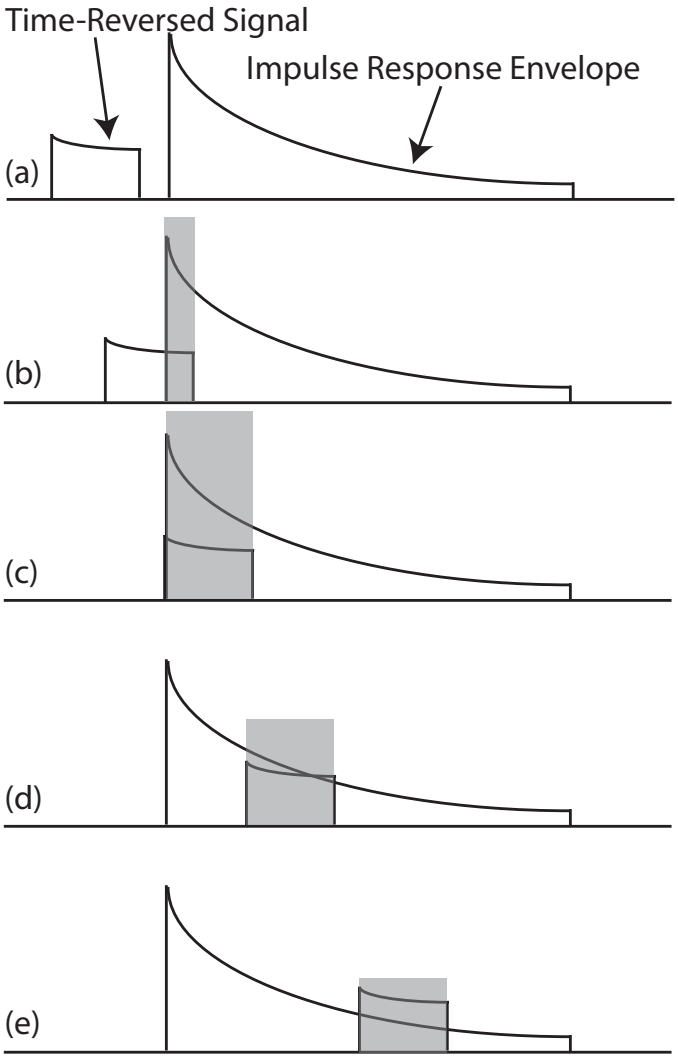

Figure 4.4: (a) Envelope of the time-reversed signal and the impulse response. Since the signals are convolved together, the time-reversed signal is effectively time-reversed a second time, hence it has a shape similar to the impulse response. (b)-(e) As the signal is injected into the medium, the product of the overlap of the two envelopes (shown schematically as a gray box) initially increases and then decreases.

4.10 is written as:

$$\frac{1}{\mathbf{M}} W(T-t) \cdot (g(-t) \otimes_t h(x_o, T-t)). \tag{4.22}$$

This windowed and time-reversed signal is then retransmitted into the cavity and recorded at a different location x_1. Thus eqn. 4.22 is convolved with an impulse response $h(x_1, t) = h'(t)$ from a different location x_1. The impulse response corresponding to the original location x_o will be denoted as $h(t)$. Assuming that the change in distance is large enough for $h(t)$ and $h'(t)$ to decorrelate, which can be determined from the van Cittert-Zernike theorem [4; 35], the expectation value and variance are easy to compute. The expectation value goes to zero since $\rho(t_1 - t_2, x_o - x_1)$ in eqn. 4.17 goes to zero as $x_o - x_1$ increases. For the variance, eqn. C.6 is recast as:

$$\begin{aligned}
&E\{h(T-(\theta_1-\tau_1))h'(t-\theta_1)h(T-(\theta_2-\tau_2))h'(t-\theta_2)\} \\
=&E\{h(T-(\theta_1-\tau_1))h'(t-\theta_1)\} \cdot E\{h(T-(\theta_2-\tau_2))h'(t-\theta_2)\} + \\
&E\{h(T-(\theta_1-\tau_1))h'(t-\theta_2)\} \cdot E\{h(T-(\theta_2-\tau_2))h'(t-\theta_1)\} + \\
&E\{h(T-(\theta_1-\tau_1))h(T-(\theta_2-\tau_2))\} \cdot E\{h'(t-\theta_1)h'(t-\theta_2)\}.
\end{aligned} \tag{4.23}$$

The first two terms on the right-hand side of the equation are zero for the same reason as the expectation value above. The third term corresponds to the incoherent variance term and is non-zero. Assuming that each of the paths has the same scattering statistics (i.e. $h'(t)$ and $h(t)$ both decay as $\sigma(t)$) then, the total variance

is the same as the incoherent variance calculated earlier.

$$\mathrm{VAR}\{r(x_1,t;x_o)\} = \left(\frac{1}{M^2}\int_{\theta_1=-\infty}^{\infty} W(T-\theta_1)\sigma(t-\theta_1)\left[\sigma(t)\otimes_t\left\{W(T-t)\rho(t-\theta_1,x_1-x_1)\times\left[g(-\theta_1)\otimes_{\theta_1}\left\{\sigma^2(T-\theta_1)\Big[g(-t)\otimes_t\rho(t-\theta_1,x_o-x_o)\Big]\right\}\right]\right\}\right]\,d\theta_1\right) \tag{4.24}$$

Just as Derode *et al.* [4] found previously in the simplified case, it is found here that the -6 dB width of the directivity pattern is a measure of the correlation length of the scattered waves. For applications in imaging, this term determines the background noise, above which all signals must be observed. Also note that as the amplitude of $g(t)$ increases, the noise floor will increase.

If $h(t)$ and $h'(t)$ decay with different decay envelopes ($\sigma(t)$ and $\sigma'(t)$ respectively), then the result becomes:

$$\mathrm{VAR}\{r(x_1,t;x_o)\} = \left(\frac{1}{M^2}\int_{\theta_1=-\infty}^{\infty} W(T-\theta_1)\sigma'(t-\theta_1)\left[\sigma'(t)\otimes_t\left\{W(T-t)\rho(t-\theta_1,x_1-x_1)\times\left[g(-\theta_1)\otimes_{\theta_1}\left\{\sigma^2(T-\theta_1)\Big[g(-t)\otimes_t\rho(t-\theta_1,x_o-x_o)\Big]\right\}\right]\right\}\right]\,d\theta_1\right). \tag{4.25}$$

4.3 Application to a Common Set of Parameters

While it was possible to ascertain some qualitative physical insights from the above equations, they do not lend themselves to easily determining the quantitative impact of various parameter (such as changing the window placement or input function). In this section, certain conditions for the envelope $\sigma(t)$, window function $W(t)$, and input function that are commonly seen in experimental work will be assumed (eqn. 4.26). This will make it is possible to simplify $\mathrm{E}\{r(t)\}$ (eqn. 4.20) and $\mathrm{VAR}\{r(t)\}$

(eqn. 4.21) to the point where trends can be surmised. This will result in a better understanding of the above equations *and* show the results for commonly seen experimental parameters. If any of these assumptions are violated, one can always return to the original equations from section 4.2.

As others have noted, for high-order multiple-scattering events, the envelope of the scattered signal, which is proportional to the standard deviation, often decays exponentially [4; 5; 36] (e.g. fig. 4.1a). Therefore it will be assumed that $\sigma(t) = u(t)e^{-\alpha t}$, where $u(t)$ is the Heaviside function. Next, a rect-window will be used for windowing the time-reversed signal. It will also be assumed that the duration of $g(t)$, t_g, is small compared to the envelope decay time constant ($\tau_\sigma = \frac{1}{\alpha}$). While there is interest in choosing long input functions, this assumption is necessary to simplify the expectation value and variance. As will be seen, as the assumption $t_g \ll \tau_\sigma$ is initially violated (i.e. $t_g < \tau_\sigma$ holds but $t_g \ll \tau_\sigma$ does not hold), the trends found for the expectation value and variance will still hold approximately, though the exact equations will not. This is because this condition is merely used to assure that the envelopes of functions do not change over time-intervals specified below. As $\sigma(t)$ does change, it is slow and smooth so the impact is not dramatic. Of course when $t_g \ll \tau_\sigma$ is strongly violated (i.e. $t_g \geq \tau_\sigma$), one must return to the equations derived in section II. Finally, it will be assumed that the duration of the acousto-electric impulse response $\rho(t)$, t_ρ, is small compared to the t_g. Summarizing these assumptions:

$$\sigma(t) = u(t)e^{-\alpha t} \tag{4.26a}$$

$$W(t) = \begin{cases} 1 & \text{if } t_{on} \leq t \leq t_{off}, \\ 0 & \text{otherwise} \end{cases} \tag{4.26b}$$

$$t_\rho \ll t_g \ll \frac{1}{\alpha} = \tau_\sigma. \tag{4.26c}$$

4.3.1 Expectation Value

The application of the above assumptions to the expectation value (eqn. 4.20) is performed in appendix D. The result is:

$$E\{r(t)\} \approx \frac{1}{2M\alpha} e^{-2\alpha t_{on}} (1 - e^{-2\alpha \Delta t}) \cdot g(T - t). \tag{4.27}$$

First, it is seen that this expectation value is a scaled version of the input function and does not increase in amplitude as t_g increases (as will be the case for the variance). Additionally, as the window shifts to later times (i.e. t_{on} increases), the peak amplitude of the expectation value drops off exponentially. This is a result of the following. First, the waveform transmitted into the system, $\frac{1}{M} W(T - t)(g(T - t) \otimes_t h(-t))$, is always the same magnitude since it is normalized by M. It is also always the same shape since the exponential decay function is self-similar. Second, a signal is not obtained until this waveform is correlated with the portion of $h(t)$ from which it came, the magnitude of this portion being $e^{-\alpha t_{on}}$. Therefore, one would expect the convolution of $\frac{1}{M} W(T - t)(g(T - t) \otimes_t h(-t))$ and $h(t)$ to scale as $e^{-\alpha t_{on}}$. As the window width increases, the peak amplitude of the expectation value grows. This being due to the fact that more signal is included in the pulse-compression that occurs during time-reversal. Since the impulse response falls off exponentially, the contribution naturally saturates. As the decay time increases, the peak increases due to more energy being included for a given window width. These dependences can be seen in fig. 4.5.

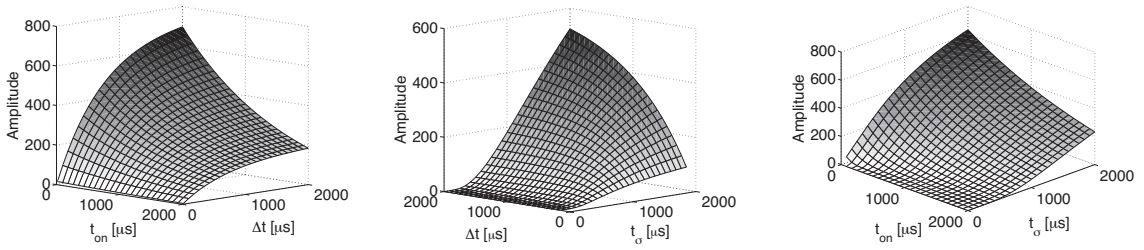

(a) (b) (c)

Figure 4.5: The dependence of the expectation value on (a) window width$\Delta\ t$ and placement t_{on} (choosing a decay time of $t_\sigma = 1500\mu s$), (b) window width$\Delta\ t$ and decay constant t_σ (choosing a window placement of $t_{on} = 1000\mu s$), and (c) window placement t_{on} and decay constant t_σ (choosing a window width of$\Delta\ t = 1000\mu s$).

4.3.2 Variance

Coherent Variance

The simplification of the coherent variance based on the assumptions in eqn. 4.26 is shown in appendix E. For $t_g > t_{on}$ the result is:

$$\mathrm{VAR}_{coherent} \approx \frac{\kappa_1 e^{4\alpha(T-t-t_{on})}}{4\alpha M^2} \begin{cases} 0 & \text{if } t < T - t_g \text{ or } T < t \\ e^{-4\alpha(T-t_{on}-t)} - e^{-4\alpha\Delta t} & \text{if } T - t_g \leq t \leq T - t_{on} \\ 1 - e^{-4\alpha\Delta t} & \text{if } T - t_{on} \leq t < T, \end{cases} \tag{4.28}$$

where $\kappa_1 = \int_{-t_g/2}^{t_g/2} g(T-(t+\tau))g(T-(t-\tau))\ d\tau$. If the duration of the input function is less than the window turn on time ($t_g \leq t_{on}$), then:

$$\mathrm{VAR}_{coherent} \approx \frac{\kappa_1 e^{4\alpha(T-t-t_{on})}}{4\alpha M^2} \begin{cases} 0 & \text{if } t < T - t_g \text{ or } T < t \\ 1 - e^{-4\alpha\Delta t} & \text{if } T - t_g \leq t < T. \end{cases} \tag{4.29}$$

From this result, it can be seen that the coherent variance term only contributes at the main lobe. It is also seen that the amplitude saturates as the window width grows for the same reason as the expectation value, though the exact shape of this

saturation varies depending on whether t_g or t_{on} is larger and is not the same as the expectation value. The amplitude also increases linearly with the decay constant $\tau_\sigma = \frac{1}{\alpha}$. The square root of the coherent variance (i.e. the coherent standard deviation) decays similarly to $E\{r(t)\}$ as t_{on} increases. Finally, it is important to note that the coherent variance scales with κ_1, which increases as the pulse duration lengthens, independent of bandwidth.

Incoherent Variance

The simplification of the incoherent variance based on the assumptions in eqn. 4.26 is also a mathematically tedious process and is given in appendix F. The result is:

$$\mathrm{VAR}_{incoherent} \approx \frac{\kappa_2(0)}{4\alpha M^2} e^{2\alpha(T-2t_{on}-t)} \begin{cases} e^{-4\alpha(T-t_{on}-t} - e^{-4\alpha\Delta t}) & \text{if } t < T - t_{on} \\ 1 - e^{-4\alpha\Delta t} & \text{if } t \geq T - t_{on}. \end{cases} \tag{4.30}$$

$\kappa_2(0)$ is approximated by the pulse-intensity integral (PII).

Thus the incoherent variance scales with the pulse-intensity integral. Noting that M will go as the maximum of $\sigma(t)$, which is approximately $e^{-\alpha t_{on}}$, it can be seen that the location of the window (i.e. t_{on}) does not change the peak magnitude of the incoherent variance term but rather shifts where it occurs. Specifically, as t_{on} increases, the time of the peak shifts in a linear manner. This contrasts with the expectation value (eqn. 4.27) and coherent variance (fig. 4.7c), which do not shift in time as t_{on} changes but rather stay at the same location and decrease exponentially in amplitude. In general for $t < T - t_{on}$ the incoherent variance increases with t as a result of more energy being transmitted into the system as described earlier. It then peaks at $t = T - t_{on}$ and decays exponentially for larger t since no additional energy is being transmitted into the system at this point. It is also clear that the incoherent variance grows as both the window width and decay constant increase in the same manner as the coherent variance.

Total Variance

The total variance can now be obtained from:

$$\mathrm{VAR} = \mathrm{VAR}_{coherent} + \mathrm{VAR}_{incoherent}. \tag{4.31}$$

When $t_{on} < t_g$

$$\mathrm{VAR} \approx \frac{1}{4\alpha M^2} \begin{cases} \kappa_2(0)e^{2\alpha(T-2t_{on}-t)}\times & \\ \quad (e^{-4\alpha(T-t_{on}-t)} - e^{-4\alpha\Delta t}) & \text{if } t \leq T - t_g \\ (\kappa_2(0) + \kappa_1 e^{2\alpha(T-t)})e^{2\alpha(T-2t_{on}-t)}\times & \\ \quad (e^{-4\alpha(T-t_{on}-t)} - e^{-4\alpha\Delta t}) & \text{if } T - t_g \leq t \leq T - t_{on} \\ (\kappa_2(0) + \kappa_1 e^{2\alpha(T-t)})e^{2\alpha(T-2t_{on}-t)}\times & \\ \quad (1 - e^{-4\alpha\Delta t}) & \text{if } T - t_{on} \leq t < T \\ \kappa_2(0)e^{2\alpha(T-2t_{on}-t)}(1 - e^{-4\alpha\Delta t}) & \text{if } T < t, \end{cases} \tag{4.32}$$

and when $t_g \leq t_{on}$

$$\mathrm{VAR} \approx \frac{1}{4\alpha M^2} \begin{cases} \kappa_2(0)e^{2\alpha(T-2t_{on}-t)}\times & \\ \quad (e^{-4\alpha(T-t_{on}-t)} - e^{-4\alpha\Delta t}) & \text{if } t < T - t_{on} \\ \kappa_2(0)e^{2\alpha(T-2t_{on}-t)}(1 - e^{-4\alpha\Delta t}) & \text{if } T - t_{on} \leq t < T - t_g \\ (\kappa_2(0) + \kappa_1 e^{2\alpha(T-t)})e^{2\alpha(T-2t_{on}-t)}\times & \\ \quad (1 - e^{-4\alpha\Delta t}) & \text{if } T - t_g \leq t < T \\ \kappa_2(0)e^{2\alpha(T-2t_{on}-t)}(1 - e^{-4\alpha\Delta t}) & \text{if } T < t. \end{cases} \tag{4.33}$$

Figure 4.6 shows when each of the conditions in the piecewise function contribute. The relative magnitude of the coherent and incoherent terms is determined by $(\kappa_2(0) + \kappa_1 e^{4\alpha(T-t)})$. When $T - \frac{\tau_\sigma}{4} ln(\frac{\kappa_2(0)}{\kappa_1}) < t$ the incoherent term is larger. Recalling that there will only be a contribution from coherent term for $T - t_g < t$

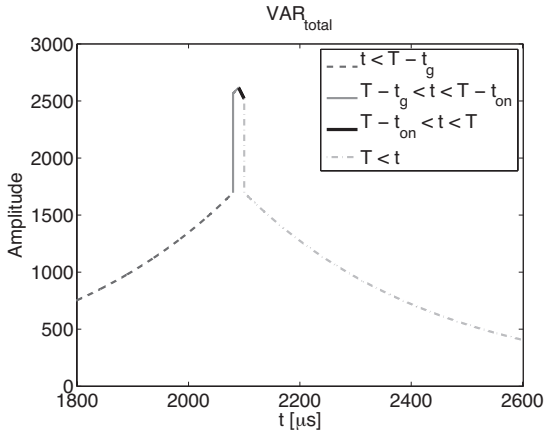

Figure 4.6: The total variance plotted with each portion of the piecewise function shown with a different line style/color.

and that $t_g \ll t_\sigma$, the condition $T - \frac{\tau_\sigma}{4} ln(\frac{\kappa_2(0)}{\kappa_1}) < t$ will always be satisfied. Thus the contribution from the incoherent term will always be larger by approximately $\kappa_2(0)/\max_{time}\{\kappa_1\}$. For tone-bursts greater than 5-cycles this ratio is approximately 4. The change in the total variance as a function of the decay constant, window width, window placement, and length of a tone-burst input function can be seen in fig. 4.7. The broad portion of the plot being due to the incoherent variance and the sharp peak around 3000 μs being the coherent variance. The dependence of both the coherent and incoherent variance on t_g is of particular note since it increases rapidly, independent of the input signal's bandwidth.

4.3.3 Signal-to-Noise Ratio

The signal-to-noise ratio (SNR) is defined as the ratio of the main lobe peak-to-peak amplitude to the side lobe standard deviation. Outside the main lobe only the incoherent term contributes.

$$\text{SNR} = \frac{\max\{E\{r(t)\}\} - \min\{E\{r(t)\}\}}{\sqrt{\text{VAR}_{incoherent}\{r(t)\}}} \tag{4.34}$$

Based on the nature of the directivity pattern, the above equation describes both the SNR as a function of time at the focus and SNR associated with the directivity

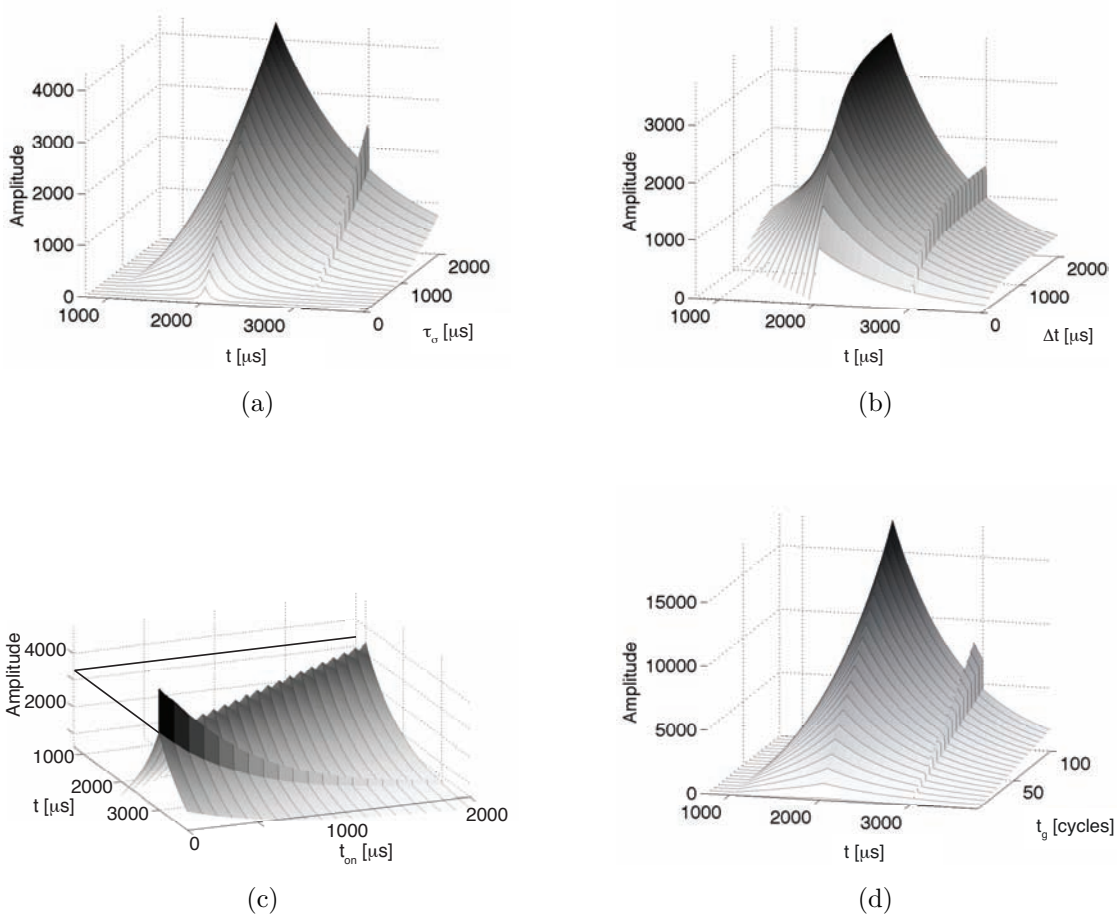

Figure 4.7: The total variance is shown as a function of time and how this dependence changes with (a) the decay time constant τ_σ, (b) the window width$\Delta\ t$, (c) the window placement t_{on}, and (d) the duration of tone-burst input t_g (using $\tau_\sigma = 1500\mu s$, $t_{on} = 1000\mu s$, $\Delta t = 1000\mu s$, and $t_g = 20$ cycles as the respective constants).

pattern. Applying eqn. 4.26 and simplifying:

$$\mathrm{SNR}(t) = \frac{(\max\{g(T-t)\}-\min\{g(T-t)\})}{\sqrt{\alpha\kappa_2(0)}\ e^{\alpha(T-t)}} \begin{cases} \frac{1-e^{-2\alpha\Delta t}}{\sqrt{(e^{-4\alpha(T-t_{on}-t)}-e^{-4\alpha\Delta t})}} & \text{if } t < T - t_{on} \\ \frac{1-e^{-2\alpha\Delta t}}{\sqrt{(1-e^{4\alpha\Delta t})}} & \text{if } t \geq T - t_{on}. \end{cases} \tag{4.35}$$

As a function of time, it is seen that the SNR has a minimum at $t = T - t_{on}$ when the functional dependence on t switches from $e^{-4\alpha(T-t_{on}-t)}$ to 1. Thus, it should be noted that this minimum shifts with the window placement, while the center of the main lobe is always at $t = T$ (i.e. it does not change as the window placement changes). The window width also impacts the SNR. Both $(1 - e^{-2\alpha\Delta t})$ and $\sqrt{(1 - e^{-4\alpha\Delta t})}$ saturate to 1 asΔ t grows, but the later saturates more quickly. Since it is the denominator, the SNR will monotonically increase as the window width increases. Finally, it is seen that the SNR is inversely proportional to the $\sqrt{\kappa_2(0)} \approx \sqrt{\mathrm{PII}}$. The PII increases as the length of a pulse grows. Thus the SNR will decrease as the pulse length increases. It is important to note that the above SNR equation was derived for an arbitrary input function $g(t)$ with the only constraint on $g(t)$ being that $t_g \ll \tau_\sigma$. Thus this result is entirely independent of bandwidth. It has previously been seen that time-reversal requires a broadband signal, otherwise it becomes simple monochromatic phase conjugation. Good time-reversal focusing still requires broadband signals, but this is only a necessary and not a sufficient condition for good focusing. The result above shows that the PII (and thus pulse length) must also be small. The presence of $\kappa_2(0)$ comes from the incoherent variance term. It results from the fact that as the PII increases, $g(t) \otimes_t h(t)$ increases. Physically this can be associated with the long-range correlations created by the longer input function in the scattered signal. Previous, work indicated that these long-range correlations come from the multiple-scattering medium, however it is now evident that they may also arise due to the input signal.

Two time points are of particular interest, the minimum SNR ($t = T - t_{on}$) and

the SNR near the main lobe ($t \approx T$). For $t = T - t_{on}$, the SNR becomes:

$$\mathrm{SNR}_{\min} = \frac{1}{\sqrt{\alpha\kappa_2(0)}} \frac{1 - e^{-2\alpha\Delta t}}{\sqrt{(1 - e^{4\alpha\Delta t})}} \frac{(\max\{g(T-t)\} - \min\{g(T-t)\})}{e^{\alpha t_{on}}}. \tag{4.36}$$

The directivity patterns can be defined by plotting the maximum signal over time at a particular location. $\mathrm{SNR}_{\min}$ does this. Therefore eqn. 4.36 can also be used to describe how the SNR of the directivity pattern will change. Figure 4.8 shows the dependence of the minimum SNR on the decay constant, window width, window placement, and duration of $g(t)$ for a tone-burst input. Note that a negative SNR, on the dB scale used, implies that the magnitude of the noise is greater than the signal itself. Previously it was mentioned that both the expectation value and the variance increase with τ_σ and$\Delta\ t$. Figure 4.8 shows however that the expectation value must increase faster since the SNR increases. Not surprisingly the SNR decreases with pulse length (independent of bandwidth) since the expectation value has no amplitude dependence on t_g but the variance does. Finally, it is seen that $\mathrm{SNR}_{\min}$ decreases as t_{on} shifts. This is expected since the maximum of the incoherent variance does not change with t_{on}, but the expectation value decreases.

The SNR near the mainlobe can be approximated from eqn. 4.35 evaluated at $t = T$ rather than $t = T \pm t_g/2$ because the incoherent variance is a slowly changing function on the time scale of t_g. In this case:

$$\mathrm{SNR}_{\text{near ML}} = \frac{1}{\sqrt{\alpha\kappa_2(0)}} \frac{1 - e^{-2\alpha\Delta t}}{\sqrt{(1 - e^{4\alpha\Delta t})}} (\max\{g(T-t)\} - \min\{g(T-t)\}). \tag{4.37}$$

The trends are also shown in fig. 4.8. It is seen that the SNR near the mainlobe is very similar to $\mathrm{SNR}_{\min}$, except that it has no dependence on the window placement.

Minimizing the ratio of the standard deviation to the expectation value (the coefficient of variance, CV) at the mainlobe is desirable so the total amplitude at

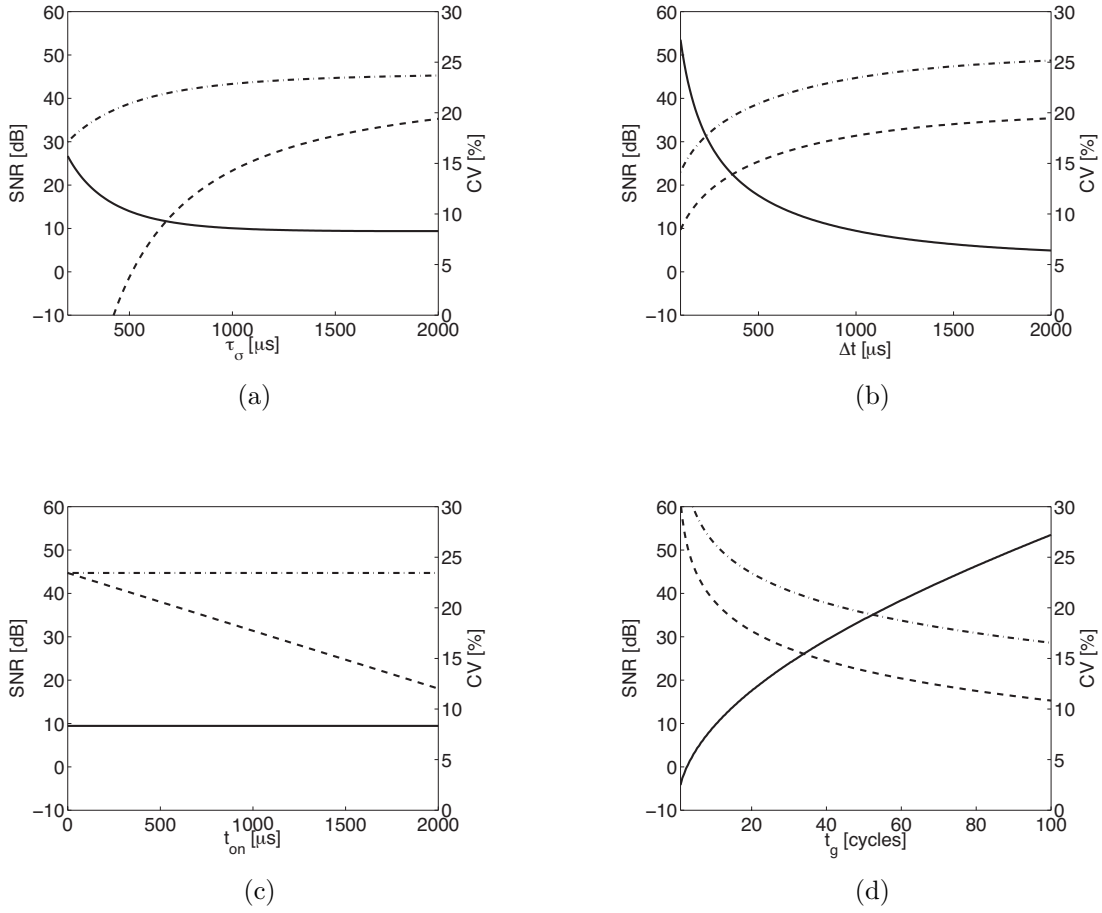

Figure 4.8: The dependence of the $\mathrm{SNR}_{\mathrm{min}}$ (dashed line), $\mathrm{SNR}_{\mathrm{near\ ML}}$ (dash-dot line), and $\mathrm{CV}_{\mathrm{max}}$ (solid line) on (a) the decay time constant, (b) the window width, (c) the window placement, and (d) the duration of a tone-burst input (using $t_\sigma = 1500\mu s$, $t_{on} = 1000\mu s$, $\Delta t = 1000\mu s$, and $t_g = 20$ cycles as the respective constants). SNR is the signal-to-noise ratio and CV is the coefficient of variance

the focus is predictable. Recalling the assumptions (eqn. 4.26):

$$\mathrm{CV} = \left.\frac{\sqrt{\mathrm{VAR}\{r(t)\}}}{E\{r(t)\}}\right|_{t\in[T-t_g,T]} \tag{4.38}$$

$$\approx \left.\frac{\sqrt{\frac{\kappa_2(0)}{c^2 4\alpha}e^{2\alpha(T-t_{on}-t)}(1-e^{-4\alpha\Delta t}) + \frac{1}{4\alpha c^2}e^{4\alpha(T-t)}e^{-2\alpha t_{on}}(1-e^{-2\alpha\Delta t})\ \kappa_1}}{\frac{1}{2\alpha c}e^{-\alpha t_{on}}(1-e^{-2\alpha\Delta t})\cdot g(T-t)}\right|_{t\in[T-t_g,T]} \tag{4.39}$$

$$= \sqrt{\alpha}\frac{e^{\alpha(T-t_{on}-t)}}{e^{-\alpha t_{on}}}\left.\frac{\sqrt{\kappa_2(0)(1-e^{-2\alpha\Delta t})(1+e^{-2\alpha\Delta t}) + \kappa_1 e^{2\alpha(T-t)}(1-e^{-2\alpha\Delta t})}}{(1-e^{-2\alpha\Delta t})\cdot g(T-t)}\right|_{t\in[T-t_g,T]} \tag{4.40}$$

$$= \sqrt{\alpha}e^{\alpha(T-t)}\left.\frac{\sqrt{\kappa_2(0)(1+e^{-2\alpha\Delta t}) + \kappa_1 e^{2\alpha(T-t)}}}{\sqrt{(1-e^{-2\alpha\Delta t})}\cdot g(T-t)}\right|_{t\in[T-t_g,T]}. \tag{4.41}$$

Recalling that $\kappa_1 = \int_{-t_g/2}^{t_g/2} g(T-(t+\tau))g(T-(t-\tau))\,d\tau$ and $\kappa_2(0) \approx \int_0^{t_g} g^2(\tau)\,d\tau$:

$$\mathrm{CV} \approx \sqrt{\alpha}e^{\alpha(T-t)}\times$$
$$\left.\frac{\sqrt{(1+e^{-2\alpha\Delta t})\int_0^{t_g} g^2(\tau)d\tau + e^{2\alpha(T-t)}\int_{-t_g/2}^{t_g/2} g(T-(t+\tau))g(T-(t-\tau))d\tau}}{\sqrt{(1-e^{-2\alpha\Delta t}}\cdot g(T-t)}\right|_{t\in[T-t_g,T]}. \tag{4.42}$$

Both terms in the numerator increase as the total 'on-time' and amplitude of the input $g(t)$ grow, whereas the denominator only increases with the amplitude. As the window shifts to later times, the second term in the denominator grows, increasing the CV. This originates from the fact that as the window shifts to later times, the expectation value decreases. Finally, for small window widths, the numerator remains finite, while the denominator goes to zero. For large windows, all the terms with$\Delta\ t$ go to zero, and thus no longer contribute. Therefore the CV gets very large for small window widths and decreases to a saturation value as the window width grows. The rate of this saturation depends on α. Also note that the CV decreases

as the decay time-constant ($\frac{1}{\alpha}$) increases and that the window placement has no impact on the CV. These results are in fig. 4.8 where the maximum CV (over time) is plotted.

4.4 Conclusions

Time-reversal acoustics has been a highly successful method of focusing sound through high-order multiple-scattering media and has found application in many fields [20–24; 26–31]. An initial shot noise model has been proposed by Derode *et al.* [4] to describe the expected signal and noise of this process. The model has been extended so that it applies to arbitrary input signals and windowing. The equations resulting from the extended model are novel and they confirmed previous predictions and also provided new predictions and explanations. This includes an explanation of the origin of the noise observed in multiple scattering time-reversal (coherent versus incoherent contributions). Additionally it predicted that windowing can cause the peak of the noise to occur far from the main lobe and that the SNR depends on the pulse intensity integral of the original input signal.

The relatively complex results of section 4.2 were then simplified for a set of parameters commonly found in experimental work. This in turn has allowed many trends to be identified, in particular the fact that increasing the length of the input function degrades the SNR, independent of bandwidth. This is the result of the expectation value not depending on t_g, but the variance increasing with t_g due to long-range correlations in the scattered signal $g(t) \otimes_t h(t)$ due to $g(t)$. Additionally, it is seen that time-reversing later windows of a recorded signal does not effect the SNR near the main lobe, but it does reduce the main lobe to side lobe ratio for side lobes far from the main lobe (fig. 4.3d). Many of these results are also qualitatively similar to those seen for one-bit time-reversal and an extension of this model to one-bit time-reversal would be interesting but beyond the scope of this dissertation.

Further analysis, specific to a particular application, can be done with these equations. This could include trying to maximize the SNR and minimize the CV for short pulses used in imaging. Alternatively, one might be interested in determining specific configurations that maximize the SNR and amplitude for long pulses that are used in thermal high-intensity focused ultrasound or acoustic radiation force experiments, among other applications. Determining signals that maximize the amplitude for short pulses [19] may be useful for histotripsy [37]. One approach for imaging may be to use coded pulses, which would effectively doubly encode the signal, first with coded pulse and second with the reverberations in the multiple-scattering media.

In addition to looking at how the input function impacts the time-reversal focused signal, it is possible to do time-reversal using multiple channels (i.e. multiple transmitter-receiver pairs). It has been shown that if multiple pairs are used to transmit the same information, the SNR increases [38]. Recognizing that the main lobe will add coherently, its amplitude will increase proportional to the number of channels, the side lobes however will add incoherently (based on the physical interpretation provided) and thus will only go as the square root of the number of channels. This has been verified by Derode *et al.* [5].

In addition, it has been proposed that if multiple transmitters and receivers are used simultaneously, one can increase the bit-rate of sending information [39]. This is because the multiple-scattering medium makes each set of paths from receiver to transducer unique and independent (to first approximation, ignoring weak localization effects, recurrent scattering, correlated scatters, etc). While it may be possible to increase the bit-rate, it is important to verify that the amount of noise (i.e. variance in the signal) does not dominate the signal (i.e. expectation value) under the conditions being used. The work of this chapter provides a method for estimating these parameters based on its derivation of signal and noise of

transmitting arbitrary pulses through a multiple-scattering medium. In particular it is found that the physical explanation of the incoherent (uncorrelated) noise term will be the same for each transmitter-receiver pair and will add as uncorrelated noise does, thus increasing the noise-floor for all channels as the square of the RMS of the signal.

4.5 Acknowledgments

I would like to thank Drs. Matthew Schipper and Albert Levine for discussions on statistics, which aided this work. This work was also supported in part by NIH grants R01EB000281 and R21CA116043.

REFERENCES

[1] A. Parvulescu and C. S. Clay, "Reproducibility of signal transmissions in the ocean," *The Radio and Electronic Engineer*, vol. 29, pp. 223–228, April 1965.

[2] A. Derode, P. Roux, and M. Fink, "Robust acoustic time reversal with high-order multiple scattering," *Physical Review Letters*, vol. 75, p. 42064210, December 1995.

[3] C. Draeger and M. Fink, "One channel time-reversal in chaotic cavities: Theoretical limits," *Journal of the Acoustical Society of America*, vol. 105, pp. 611–617, February 1999.

[4] A. Derode, A. Tourin, and M. Fink, "Ultrasonic pulse compression with one-bit time reversal through multiple scattering," *Journal of Applied Physics*, vol. 85, pp. 6343–6352, May 1999.

[5] A. Derode, A. Tourin, and M. Fink, "Limits of time-reversal focusing through multiple scattering: Long-range correlation," *Journal of the Acoustical Society of America*, vol. 107, pp. 2987–2998, June 2000.

[6] V. Leroy and A. Derode, "Temperature-dependent diffusing acoustic wave spectroscopy with resonant scatterers," *Physical Review E*, vol. 77, p. 036602, March 2008.

[7] A. Derode, A. Tourin, and M. Fink, "Random multiple scattering of ultrasound. II. is time reversal a self-averaging process?," *Physical Review E*, vol. 64, no. 3, p. 036606, 2001.

[8] B. A. van Tiggelen, "Green function retrieval and time reversal in a disordered world," *Physical Review Letters*, vol. 91, p. 243904, December 2003.

[9] J. de Rosny, A. Tourin, A. Derode, B. A. van Tiggelen, and M. Fink, "Relation between time reversal focusing and coherent backscattering in multiple scattering media: A diagrammatic approach," *Physical Review E*, vol. 70, p. 046601, 2004.

[10] P. Blomgren, G. Papanicolaou, and H. Zhao, "Super-resolution in time-reversal acoustics," *Journal of the Acoustical Society of America*, vol. 111, p. 230, 248 2002.

[11] G. Ribay, J. de Rosny, and M. Fink, "Time reversal of noise sources in a reverberation room," *Journal of the Acoustical Society of America*, vol. 117, no. 5, pp. 2866–2872, 2005.

[12] C. Draeger and M. Fink, "One-channel time reversal of elastic waves in a chaotic 2D-silicon cavity," *Physical Review Letters*, vol. 79, pp. 407–410, July 1997.

[13] C. Draeger, J.-C. Aime, and M. Fink, "One-channel time-reversal in chaotic cavities: Experimental results," *Journal of the Acoustical Society of America*, vol. 105, pp. 618–625, February 1999.

[14] N. Quieffin, S. Catheline, R. K. Ing, and M. Fink, "Real-time focusing using an ultrasonic one channel time-reversal mirror coupled to a solid cavity," *Journal of the Acoustical Society of America*, vol. 115, pp. 1955–1960, May 2004.

[15] G. Montaldo, N. Perez, C. Negreira, and M. Fink, "The spatial focusing of a leaky time reversal chaotic cavity," *Waves in Random and Complex Media*, vol. 17, pp. 67–83, February 2007.

[16] G. Montaldo, P. Roux, A. Derode, C. Negreira, and M. Fink, "Ultrasound shock wave generator with one-bit time reversal in a dispersive medium, application to lithotripsy," *Applied Physics Letters*, vol. 80, pp. 897–899, February 2002.

[17] A. Y. Sutin, E. Roides, and A. P. Sarvazyan, "Damage detection in composites using the time-reversal acoustics method," *Journal of the Acoustical Society of America*, vol. 116, p. 2567, October 2004.

[18] Y. D. Sinelnikov, A. Y. Sutin, and A. P. Sarvazyan, "Time-reversal acoustic focusing with liquid resonator for medical applications," *6th International Symposium on Therapeutic Ultrasound*, vol. 911, pp. 82–86, 2006.

[19] L. Fillinger, A. Y. Sutin, and A. P. Sarvazyan, "Time reversal focusing of short pulses," *IEEE Ultrasonics Symposium*, pp. 220–223, October 2007.

[20] M. Fink, G. Montaldo, and M. Tanter, "Time-reversal acoustics in biomedical engineering," *Annual Review of Biomedical Engineering*, vol. 5, pp. 465–497, June 2003.

[21] A. S. Gliozzi, M. Griffa, and M. Scalerandi, "Efficiency of time-reversed acoustics for nonlinear damage detection in solids," *Journal of the Acoustical Society of America*, vol. 120, pp. 2506–2517, November 2006.

[22] S. D. Kim, C. W. In, K. E. Cronin, H. Sohn, and K. Harries, "Reference-free ndt technique for debonding detection in cfrp-strengthened rc structures," *Journal of Structural Engineering*, vol. 133, no. 8, pp. 1080–1091, 2007.

[23] E. Larose, "Mesoscopics of ultrasound and seismic waves: Application to passive imaging," *Ann. Phys. Fr*, vol. 31, no. 3, pp. 1–126, 2006.

[24] C. Larmat, J.-P. Montagner, M. Fink, Y. Capdeville, A. Tourin, and E. Clevede, "Time-reversal imaging of seismic sources and application to the great sumatra earthquake," *Geophysical Research Letters*, vol. 33, p. L19312, 2006.

[25] E. Larose, P. Roux, M. Campillo, and A. Derode, "Fluctuations of correlations and green's function reconstruction: Role of scattering," *Journal of Applied Physics*, vol. 103, p. 114907, 2008.

[26] G. F. Edelmann, T. Akal, W. S. Hodgkiss, S. Kim, W. A. Kuperman, and H. C. Song, "An initial demonstration of underwater acoustic communication using time reversal," *IEEE Journal of Oceanic Engineering*, vol. 27, pp. 602–609, July 2002.

[27] P. Roux, A. Derode, A. Peyre, A. Tourin, and M. Fink, "Acoustical imaging through a multiple scattering medium using a time-reversal mirror," *Journal of the Acoustical Society of America*, vol. 107, pp. L7–L12, December 1999.

[28] G. Montaldo, D. Palacio, M. Tanter, and M. Fink, "Building three-dimensional images using a time-reversal chaotic cavity," *IEEE Transactions on Ultrasonics, Ferroelectrics, and Frequency Control*, vol. 52, pp. 1489–1498, September 2005.

[29] J. V. Candy, A. J. Poggio, D. H. Chambers, B. L. Guidry, C. L. Robbins, and C. A. Kent, "Multichannel time-reversal processing for acoustic communications in a highly reverberant environment," *Journal of the Acoustical Society of America*, vol. 118, pp. 2339–2354, October 2005.

[30] R. C. Qui, C. Zhou, N. Guo, and J. Q. Zhang, "Time reversal with miso for ultrawideband communications: Experimental results," *IEEE Antennas and Wireless Propagation Letters*, vol. 5, pp. 269–273, 2006.

[31] G. Lerosey, J. de Rosny, A. Tourin, and M. Fink, "Focusing beyond the diffraction limit with far-field time reversal," *Science*, vol. 315, pp. 1120–1122, 2007.

[32] A. Papoulis, *Probability, Random Variables, and Stochastic Processes*. McGraw-Hill Series in Systems Science, McGraw-Hill, Inc., 1984.

[33] A. Sarvazyan, "Ultrasonic tranasducers for imaging and therapy based on time-reversal principles," *Journal of the Acoustical Society of America*, vol. 123, p. 3429, May 2008.

[34] G. Marsaglia and W. W. Tsang, "The ziggurat method for generating random variables," *Journal of Statistical Software*, vol. 5, pp. 1–7, October 2000.

[35] J. W. Goodman, *Statistical Optics*. Wiley, 1985.

[36] A. Tourin, A. Derode, A. Peyre, and M. Fink, "Transport parameters for an ultrasonic pulsed wave propagating in a multiple scattering medium," *Journal of the Acoustical Society of America*, vol. 108, no. 2, pp. 503–512, 2000.

[37] W. W. Roberts, T. L. Hall, K. Ives, J. S. Wolf, J. B. Fowlkes, and C. A. Cain, "Pulsed cavitational ultrasound: A noninvasive technology for controlled tissue ablation (histotripsy) in the rabbit kidney," *The Journal of Urology*, vol. 175, pp. 734–738, February 2006.

[38] M. Fink, "Acoustic time-reversal mirrors," *Topics in Applied Physics*, vol. 84, pp. 17–42, 2002.

[39] A. Derode, A. Tourin, J. de Rosny, M. Tanter, S. Yon, and M. Fink, "Taking advantage of multiple scattering to communicate with time-reversal antennas," *Physical Review Letters*, vol. 90, p. 014301, January 2003.

CHAPTER V

Additional Supplemental and Motivational Work

In addition to the main results presented in the previous chapters, additional work has been performed which provides support and motivation. Chapters II and III are concerned with the use of ADV bubbles for aberration correction. Despite the extensive work performed with ADV (table 1.1), the physical mechanisms underlying ADV are not yet fully understood. Of the work performed, references [1–7] have studied how various acoustic and material parameters impact the vaporization threshold. Unfortunately, various data point towards different mechanisms. Ultra high-speed photography was used to image the vaporization process during the first few microseconds of the vaporization process [8]. The first part of this chapter will describe this work.

Chapter IV developes a shot-noise model to describe time-reversal performed with arbitrary input signals in a multiple-scattering medium. Whilst several applications were listed, the most prominent is time-reversal chaotic cavities (TRCCs). To provide additional motivation for this work, several TRCC experiments are presented. This work can be found in [9; 10] and is described in the second portion of this chapter.

5.1 Initial Growth and Coalescence of ADV Microbubbles

5.1.1 Introduction

There are two orthogonal approaches to initiating the phase-change that occurs during ADV (assuming the overall system is isochoric during the initial triggering of ADV), changing the pressure or changing the temperature. For the acoustic parameters in which ADV is typically performed *in vivo* [2; 11; 12], the energy deposition is such that the medium is not heated. Thus, the phase-transition is due to pressure changes. These pressure changes may come as the result of acoustic cavitation (i.e. the sound wave causes direct pressure changes, which initiate ADV) or hydrodynamic cavitation (i.e. the sound wave induces movement and thus an associated velocity that can be related to changes in pressure and shear force). Either of these mechanisms may occur internal to, at the surface of, or external to the droplet.

Certain data obtained while studying ADV seems to indicate that acoustic cavitation external to the droplet is the mechanism. For a possible mechanism external to the droplet, it has been found that placing ultrasound contrast agent (UCA) in flow with superheated droplets, causes a decrease in the required acoustic pressure to vaporize the droplets when using 20 μs vaporization pulses [5]. In this case, the UCA may act as a nucleation site for inertial cavitation, whose associated violent collapse may disrupt the superheated droplet, allowing it to phase-transition. Without UCA it has been found under a variety of acoustic and material parameters, usually above 3 MHz, that inertial cavitation (IC) initiates at a higher pressure than ADV and that the IC event may be an ADV bubble collapsing [7]. Together these studies show that acoustic cavitation may cause ADV, but an appropriate external nucleation site (e.g. UCA) must be present.

Additionally, it has been found without UCA that as the pulse length of the

vaporization pulse initially increases (e.g. 1 μs to 10 μs), the threshold for transition does not change. However, if the length of the pulse is increased further (beyond say 1 ms) then a sudden drop in the vaporization threshold pressure is seen [5]. This is consistent with nucleation starved inertial cavitation (which is a stochastic process whose probability increases with time). Additionally, it has been found that changing the fluid properties (e.g. viscosity) of the fluid containing the superheated droplets results in changes in the vaporization threshold, which is consistent with previous inertial cavitation work [1; 7].

However certain other data does not support the external acoustic cavitation hypothesis. A few hundred high-speed images have been collected of droplet vaporization [4; 8]. The images are planar projections and thus it is not possible to determine if the vaporization is occurring on the surface of or within the droplet. However if external acoustic cavitation were a primary mechanism, it would be expected that a nucleation site clearly outside the surface of the droplet would be recorded occasionally. This however has not been the case. Additionally, it has been found that the ADV pressure threshold decreases as the insonation frequency increases. This is contrary to the increasing pressure threshold with frequency associated with inertial cavitation. It should be noted that these results hold in a micro flow-tube experiment where measurement of vaporization is performed on a macroscopic scale for ensembles of droplets, not for individual droplets.

Other data that has been obtained seems to indicate that hydrodynamic cavitation is the initiation mechanism. One such result is that as the droplet diameter is increased, it becomes easier to vaporize [4; 7]. It is known that larger objects induce greater changes to flow patterns, which can result in increased cavitation activity, thus implying that a larger droplet would help set the stage for adjacent hydrodynamic cavitation that can initiate the phase-transition. Additionally, previous high-speed camera images seemed to indicate that nucleation

sites preferentially occured on the acoustic axis, i.e. corresponding to the direction of motion [4]. These same sets of images also indicated that vaporization occurs only once the droplet began oscillating at a particular magnitude [4]. This association with motion would imply hydrodynamic cavitation. Again however, some of the data contraindicates hydrodynamic cavitation. For instance, since a particular oscillation magnitude must be reached, it is implied that for increasing frequency, a larger velocity is needed to initiate vaporization. The larger velocity would imply larger pressure gradients are needed. However, the threshold pressure decreases with increasing frequency. Additional other data being studied by others at the University of Michigan (such as the impact of changing surfactants for the droplet formation or changing the degree of superheat) has yet to be associated with a given theory.

Each of the various ADV applications (occlusion therapy [2; 11; 12], aberration correction [13], drug delivery, and bubble-enhanced high-intensity focused ultrasound [6; 14]) can benefit from the specific pathways for ADV discussed above. For instance, it has been observed that depending on the acoustic and fluid parameters, ADV can occur with and without inertial cavitation [7]. For drug delivery, inertial cavitation may be a useful means of actively assisting drugs, incorporated into the droplets, to cross vascular or cellular membranes when the droplets vaporize. For occlusion therapy, the capillary rupture that can be associated with inertial cavitation may make it more difficult to occlude flow. For aberration correction, it is desirable to produce a small, isolated, single bubble, whereas bubble-enhanced high-intensity focused ultrasound may benefit from a higher density of bubbles as might be achieved with fragmentation that is often associated with IC.

To investigate these pathways, ultra high-speed photography was used to study up to the first sixteen microseconds of the vaporization process. Initially, the impact of the acoustic pulse length was observed. Next, the growth of the bubble over the first two microseconds was monitored. Finally, the coalescence of two bubbles near

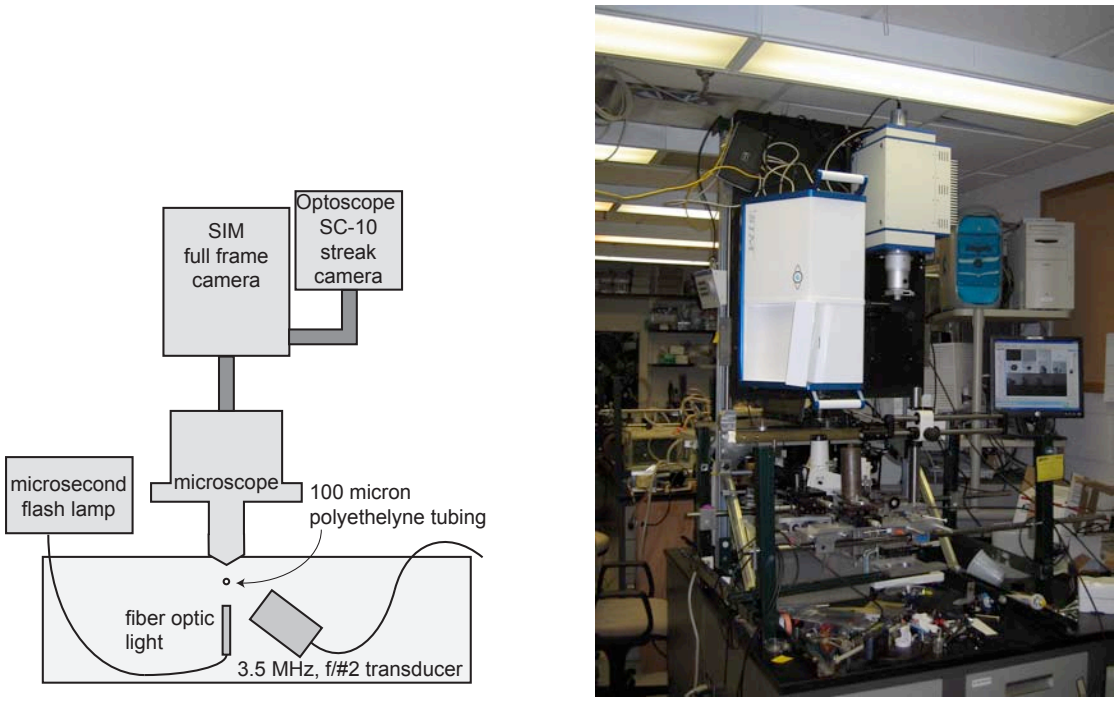

(a) (b)

Figure 5.1: Experimental setup of the ultra high-speed imaging system (schematic on left, photo on right). The full frame camera is coupled to the streak camera on a vertical table. Below is a hybrid microscope with a 40x water immersion long distance objective. Droplets are positioned in the acoustic and optical field using a polyethylene tube (shown in cross-section).

each other was recorded.

5.1.2 Experimental Setup

The experimental setup can be seen in fig. 5.1.

Droplet Preparation

ADV droplets were manufactured by first creating a solution of 4 mg per mL bovine albumin (A3803, Sigma-Aldrich, St. Louis, MO, USA) in normal saline (0.9% w/v, Hospira Inc., Lake Forest, IL, USA). Seven hundred fifty microliters of this solution was added to a 2 mL glass vial. Then liquid dodecafluoropentane (DDFP, L16969, Alfa Aesar, Ward Hill, MA, USA) was added gravimetrically to a final DDFP volume fraction of 25%. The vial was capped and shaken for 45 seconds at 4550 cycles per

minute using an amalgamator (VialMix, Lantheus Medical Imaging, Billerica, MA, USA). The droplets were then refrigerated (5°C) until use.

Imaging Specifications

Full frame photography was performed using a Specialised Imaging Multi-Channel Framing Camera (SIM802, Specialised Imaging Ltd., Hertfordshire, UK). Sixteen full frame images (1360 × 1024 pixels) could be obtained with a frame rate of up to 200 MHz. Coupled to the SIM802 was a streak camera (Optoscope SC-10, Optronis GmbH, Kehl, Germany) capable of simultaneously obtaining streak speeds up to 64 lines per microsecond. Illumination was provided with a 300 Joule, 12 μs flash lamp.

Magnification was achieved by placing a 50 mm to 24 mm Nikkor lens (Nikon Inc., Melville, NY, USA) on the camera to provide a two-times gain. The Nikkor lens was focused on the camera port of a Nikon eclipse series microscope with a forty-times water objective. The cumulative magnification resulted in a 12 pixels per micron resolution for the full frame images (corresponding to a 113 × 85 micron field of view).

Acoustics

Confocal with the 40 times water objective was a 3.5 MHz, f-number 2, single-element transducer with a focal distance of 38.1 mm (A381S, Panametrics, Olympus NDT Inc., Waltham, MA, USA). A function generator (33120A, Agilent, Palo Alto, CA, USA) was gated with a secondary function generator (3314A, Agilent) to produce single two, six, or thirteen-cycle tone bursts. The tone bursts were amplified with a power amplifier (Model 350, Matec, Northborough, MA, USA). The amplified signal was transmitted to the transducer. The acoustic output was measured to be up to 8 MPa (peak rarefactional) in a water path. ADV droplets were brought to the focus via a 100 micron inner-diameter polyethylene tube. The tube was

oriented perpendicular to the optical and acoustic beams. The entire setup was contained within a water tank at 22°C. Note that at this temperature the DDFP is not superheated.

5.1.3 Results

Acoustic Pulse Duration

Three burst lengths were initially investigated using interframe times of 1.025 μs and exposures of 25 ns. Thirteen vaporization events were observed with an approximately two-cycle tone burst, seven events for an approximately six-cycle tone burst, and fifteen events for an approximately thirteen-cycle tone burst. The droplets varied between 6 and 20 μm in diameter for the two-cycle tone bursts and between 4.5 and 15 μm for the thirteen-cycle tone bursts. Figures 5.2 and 5.3 show typical results for the two and thirteen-cycle tone bursts respectively.

The most striking difference is that for the two-cycle case, it is seen that not all of the DDFP phase-transitioned to a gas. This result was seen for all droplet sizes with two-cycle vaporization. In comparison, for the thirteen-cycle tone burst, the images seem to show all of the DDFP phase transitioning during the on-time of the acoustics. This result was seen in all fifteen cases tested. For the six-cycle tone burst, incomplete vaporization was observed for three cases, and all of the DDFP phase-transitioned for the other four cases.

Another interesting observation is that for the two-cycle cases, the shell appears to have remained intact. This is seen in the clear and sharp delineation of the edge of the droplet and the lack of fragmentation (fig. 5.2). It is possible that these observations are not due to the shell but instead the result of the immiscible nature of DDFP in water. Further work with fluorescent shells or another marker is needed to fully elucidate this point. A final note for the two-cycle cases is that many bubbles appear within the projection of the droplet. However in none of the cases were the bubbles seen outside the projection. If the vaporization were occurring external to

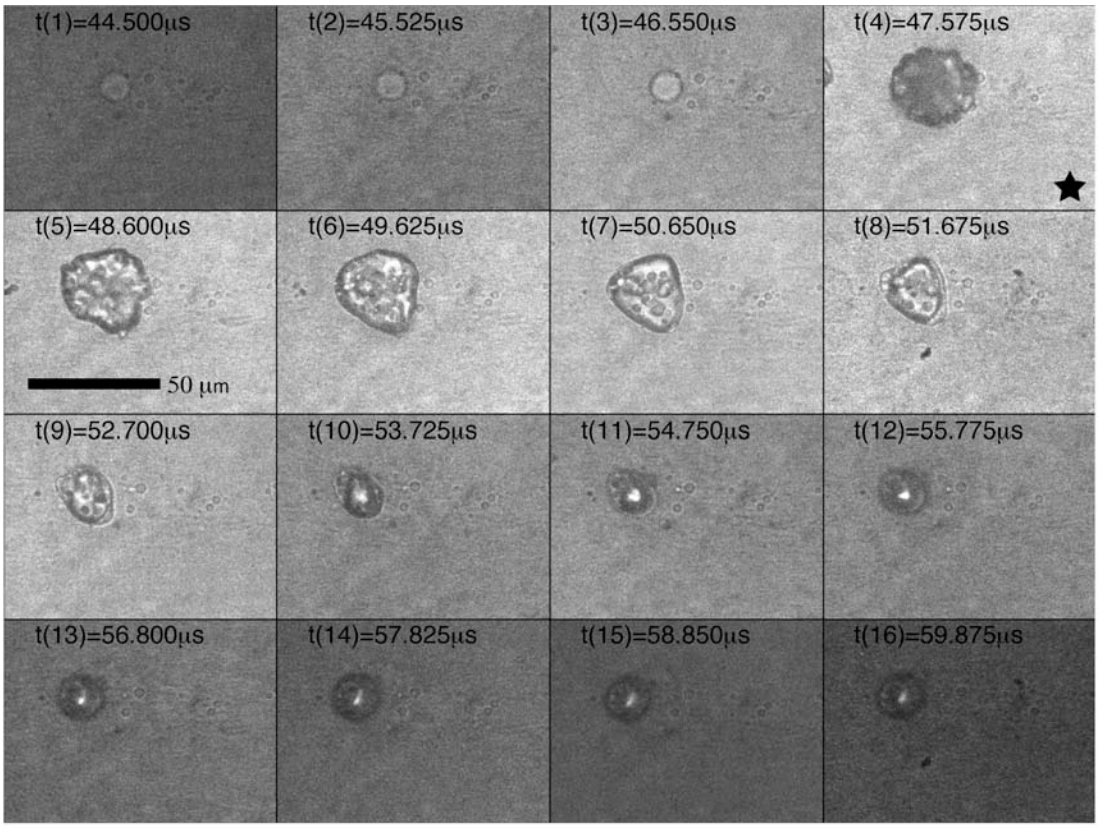

Figure 5.2: Sixteen images showing vaporization using an approximately two-cycle tone burst. The presence of ultrasound during a frame is denoted by a star. The timing of the frames is seen in the upper left of each frame. The differences in intensities between frames is a result of the duration of the flashlamp.

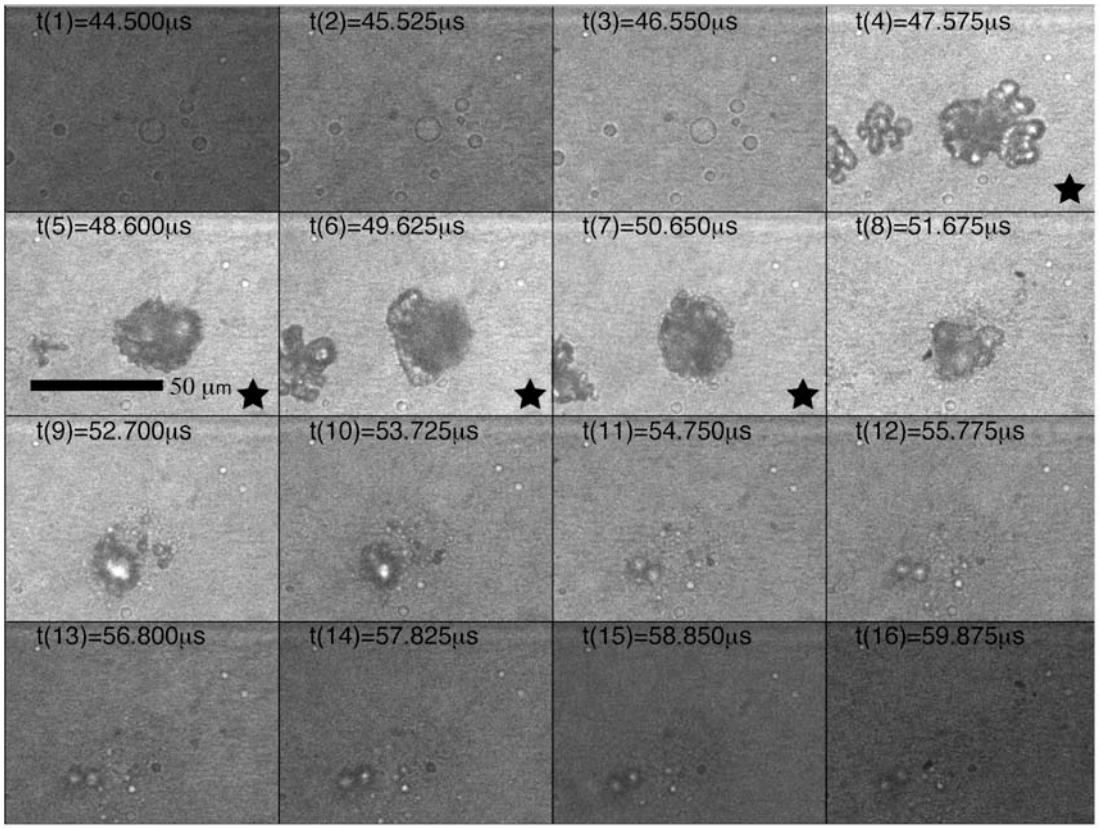

Figure 5.3: Sixteen images showing vaporization using approximately thirteen-cycle tone bursts. The key difference between the two-cycle and thirteen-cycle conditions is that not all of the DDFP phase-transitioned when only a two-cycle tone burst was used.

the droplet, it would be expected that some of these bubbles would occur outside of the droplet. Therefore these results indicate that under these conditions (short tone bursts and a dearth of external nucleation sites such as UCA) external acoustic cavitation is not the primary mechanism.

Based on the result of this section, all of the following experiments were performed using thirteen-cycle tone bursts to ensure complete vaporization.

Initial Vaporization Dynamics

The initial vaporization dynamics were studied next by using a 75 ns frame repetition period (13 MHz frame rates) and 25 ns optical exposures. Due to the short interframe time, once the ultrasound arrives, it remains present for the remainder of the frames. Thirty-seven vaporization events were studied in this manner. Fig. 5.4 shows a sample vaporization event.

The first point to note is that the effect of the compressional and rarefactional portions of the wave can been seen in the oscillatory nature of the transitioning bubble. This is possible because the frame repetition period is approximately one-quarter of an acoustic period at 3.5 MHz. The effect is most obvious in frames six and seven, where one sees the nucleation bubble appear and then disappear, respectively. In frame eight the bubble again returns. The oscillation effect can be seen again going from frames ten to thirteen where the growth of the bubble seems to slow and perhaps shrink slightly before again continuing to grow more quickly.

To study this effect more concretely, the droplet/bubble radius as a function of time since nucleation was determined for all thirty-seven vaporization events. Figure 5.5a plots the bubble radius versus elapsed time for all events. Due to the varying size of each initial droplet, and changes in relative position due to tube movement and droplet position within the tube, there is a relatively large variance between each droplet. However, it is clearly seen that the oscillatory nature is present in most of the vaporization events, at approximately the acoustic frequency.

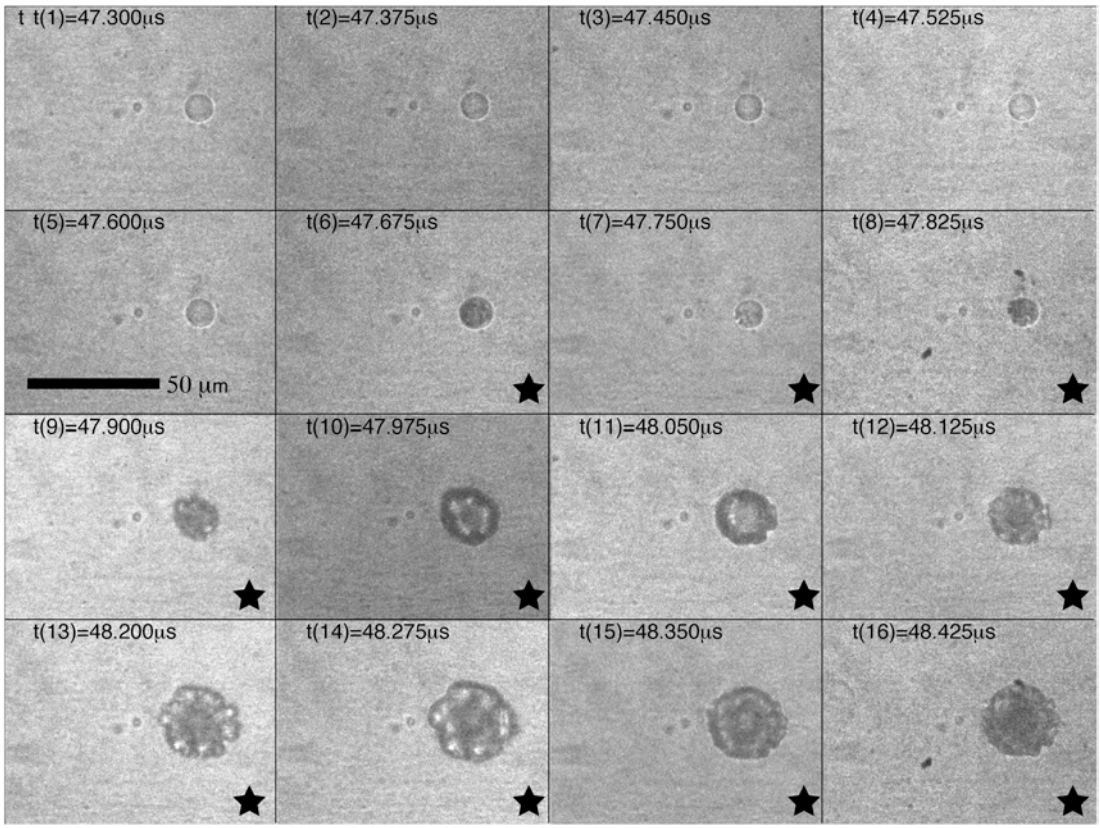

Figure 5.4: Example vaporization event imaged with a 75 ns frame repetition period. The stars indicate when the acoustic pulse is present. Note that the effects of the compressional and rarefactional portion of the waves can be seen in the oscillatory nature of the transitioning bubble. The exact phase of the acoustic wave for each frame is unknown however.

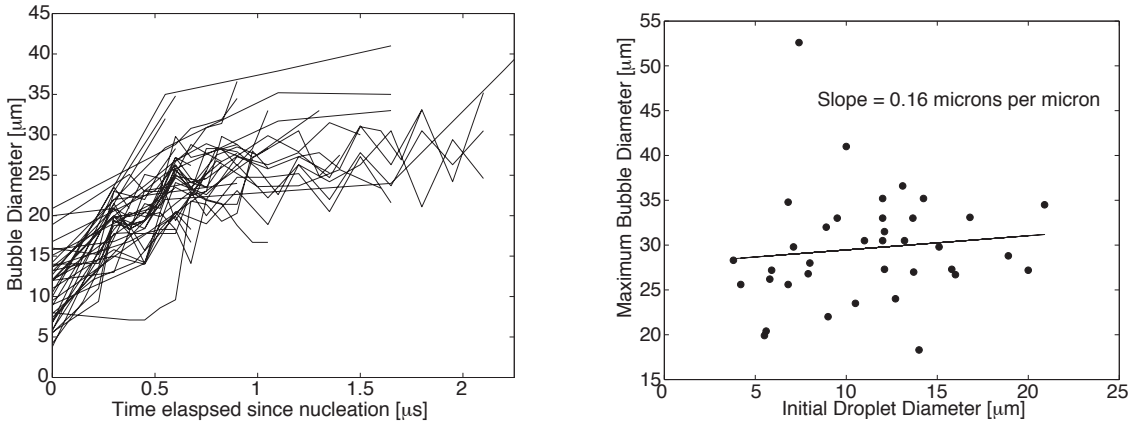

(a) (b)

Figure 5.5: (a) The bubble diameter versus time since nucleation for all thirty-seven vaporization events analyzed. Note that the oscillation in droplet diameter with the acoustic period is evident in most of the vaporization events. The diameter at time zero is the initial droplet diameter. (b) The maximum bubble diameter achieved during the first two microseconds versus the droplet diameter that produced the bubbles. Growth due to in-gassing of ambient gasses is not seen on this time scale.

Another feature that begins to become apparent from fig. 5.5a is that the bubble diameter after one to two microseconds is independent of the initial droplet diameter. Figure 5.5b shows the maximum bubble diameter during the first two microseconds as a function of the initial droplet diameter. A linear fit shows a nearly flat slope. Clearly during the first two microseconds, the bubble has not reached its terminal size. However, the results indicate that the initial bubble grows independent of the size of the droplet. This likely indicates that the initial bubble growth is driven by acoustics and/or the consumption of DDFP with all the tested droplets not phase-transitioning all of the DDFP during the first two microseconds.

Bubble Coalescence

In the process of vaporization, it was seen in 35 cases (not used in the previous analysis), that when two or more droplets vaporized near each other, they would coalesce (fig. 5.6) [15; 16]. The coalescence was not the result of bubbles growing into each other, but rather the centers of mass moving towards each other. This

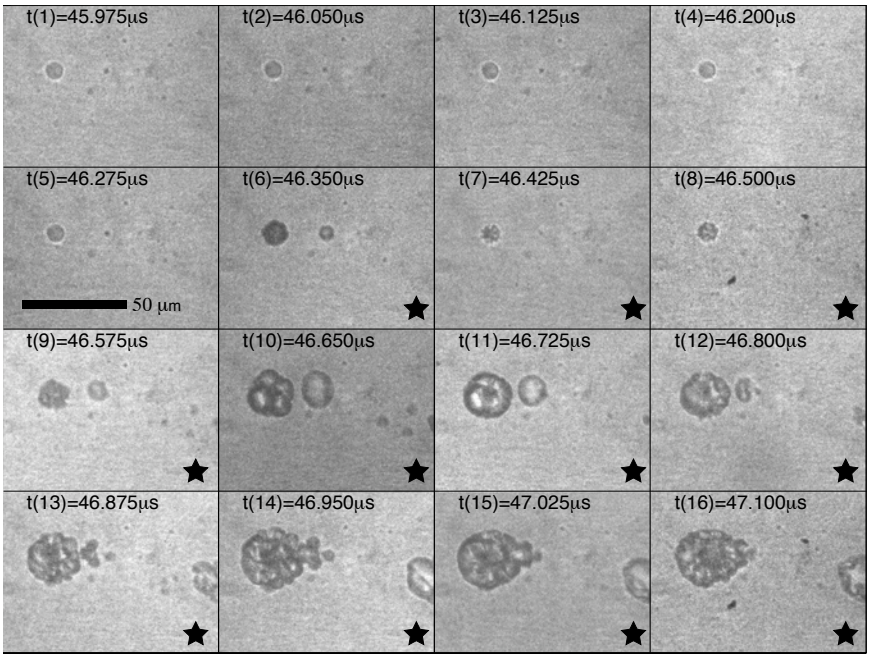

(a)

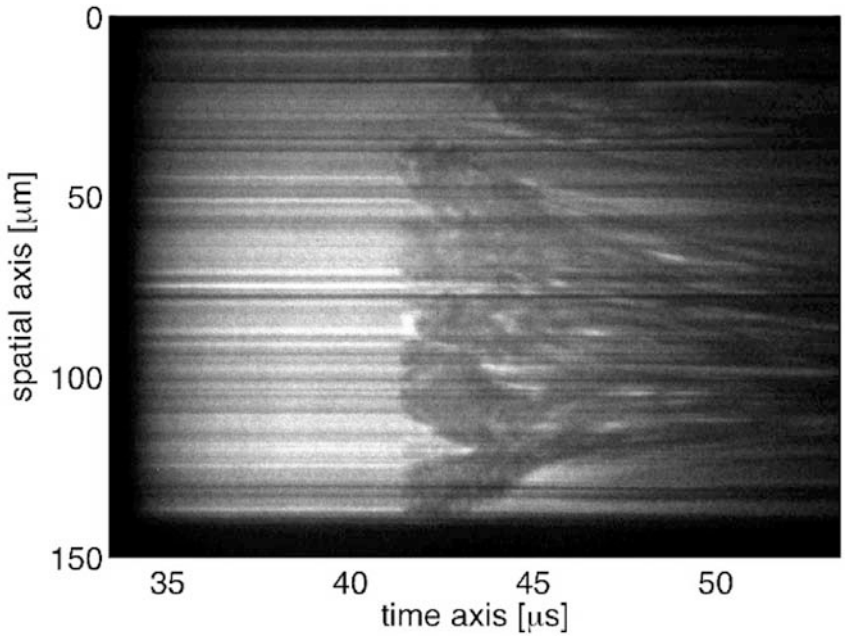

(b)

Figure 5.6: (a) Full frame images demonstrating the coalescence of two ADV bubbles. Note that the center of mass of each bubble displaces toward the other, indicating an attractive force, such as secondary Bjerknes radiation force. (b) A streak image further demonstrating bubble coalescence.

occurred while the acoustics were on. It is believed that the coalescence is due to secondary Bjerknes radiation force. Measuring the relative velocity, it was found that the average droplet-droplet impact velocity was 9 m/s and that the impact velocity varied between 4.5 and 16.5 m/s.

5.1.4 Conclusions

It was seen that the acoustic pulse length has a significant impact on the initial vaporization process. With two-cycle tone bursts, part of the DDFP did not vaporize and it is possible that the shell remained intact. The isolated bubble that would result from this could be beneficial for producing point-targets for phase aberration correction. If in fact the shell remains intact however, this would have a very detrimental impact on the ability to deliver drugs. For thirteen-cycle tone bursts, it was seen that all of the DDFP phase transitioned. In this process, fragmentation could also be seen. The fragmentation may be beneficial in distributing drugs and producing multiple bubbles for bubble-enhanced high-intensity focused ultrasound thermal therapy, but detrimental for aberration correction.

Using thirteen-cycle tone bursts, the initial vaporization process was studied and it was found that the maximum bubble diameter during the first two microseconds was independent of the size of the originating droplet. This may indicate that small droplets have a faster wall velocity as they vaporize. If this is the case, then the acoustic emissions from a small versus large droplet might be able to be discriminated, allowing for an *in vivo* assessment of droplet sizes being vaporized. This knowledge would be useful for all of the applications discussed.

Finally, it was seen that droplets near each other could coalesce. This coalescence may be highly beneficial for occlusion therapies, as large bubbles will occlude higher in the vascular tree. The coalescence may be detrimental to aberration correction if the resulting bubble is too large to be considered a point target. The coalescence may also impact how drugs are distributed upon vaporization.

The results of this work suggest additional study to further elucidate the points highlighted here. It is also important that the work here be repeated in a water bath at 37°C to simulate the impact of superheat, which would be experienced *in vivo*.

5.2 Experimental Applications of Time-Reversal Chaotic Cavities

5.2.1 Motivation

This section is motivated by an application for time-reversal chaotic cavities initially proposed by Armen Sarvazyan and the University of Michigan Basic Radiological Sciences Division (NIH Grant R21EB002787). Over the past several years multiple methods of measuring *in vivo* tissue elasticity have been developed. One method measures the shear wave velocity, which is proportional to the square root of the shear modulus. The shear modulus is a measure of elasticity. It was proposed to use magnetic resonance imaging (MRI) to track a propagating shear wave [10]. The shear waves were created using acoustic radiation force. It was shown that an air-backed 9 cm diameter single element piezoelectric PZT crystal transmitting an 800 ms tone burst at 512 kHz could create a shear waves that could be measured in a tissue-mimicking phantom via MRI. From this an estimate of the elasticity of the tissue-mimicking phantom was obtained [9]. Unfortunately, shear waves are rapidly attenuated in many tissues. Therefore, to obtain elasticity measurements throughout a 3D volume, it is necessary to transmit focused tone bursts to many different locations. With a single element crystal, it is necessary to physically move the transducer to focus at multiple locations. To accomplish focusing throughout a 3D volume without mechanically moving the transducer either a 2D array or a time-reversal chaotic cavity must be used. Two-dimensional arrays typically have several hundred or thousand elements, making them expensive. A time-reversal chaotic cavity however can focus short pulses throughout a 3D volume with as few

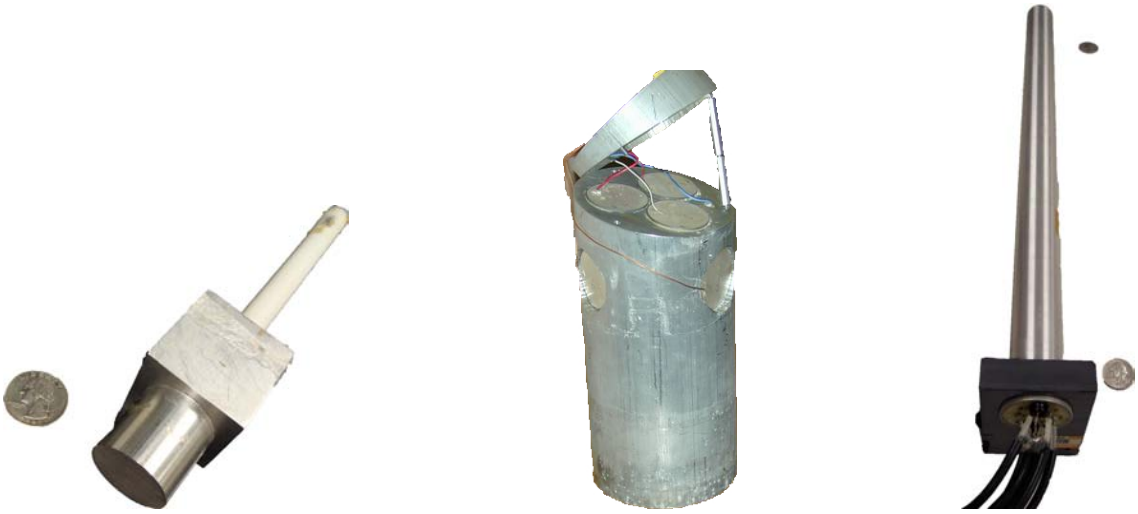

(a) (b) (c)

Figure 5.7: Photographs of various time-reversal chaotic cavities used. Note that the transducers in the leftmost cavity are on the inside of the cavity and therefore cannot be seen.

as one element. However to induce a shear wave, it is necessary to focus long pulses to achieve a significant displacement from acoustic radiation force. This need was the original motivation for chapter IV and the following study of TRCCs.

5.2.2 Time-Reversal Chaotic Cavity Focusing Capabilities

As described earlier, a simple TRCC consists of an ultrasound transducer adhered to block of metal. Figure 5.7 shows several different cavities. The cavities in figs. 5.7a and 5.7b were constructed by Artann Laboratories (West Trenton, NJ, USA). The cavity shown in fig. 5.7c was constructed by Imasonic SAS (Besançon, France) and is schematically described in [17].

To reiterate, TRCC experiments consist of sending an electronic signal to one of the transducers. The transducer then launches an acoustic wave that reverberates within the cavity. Due to irregularities in the shape of the cavity or position of the transducer, the sound reverberates in a chaotic manner such that it quickly becomes a diffuse, ergodic wave. As a result, the waves passing through any point over time form a signal that is unique to the particular point (to first order). If the cavity is

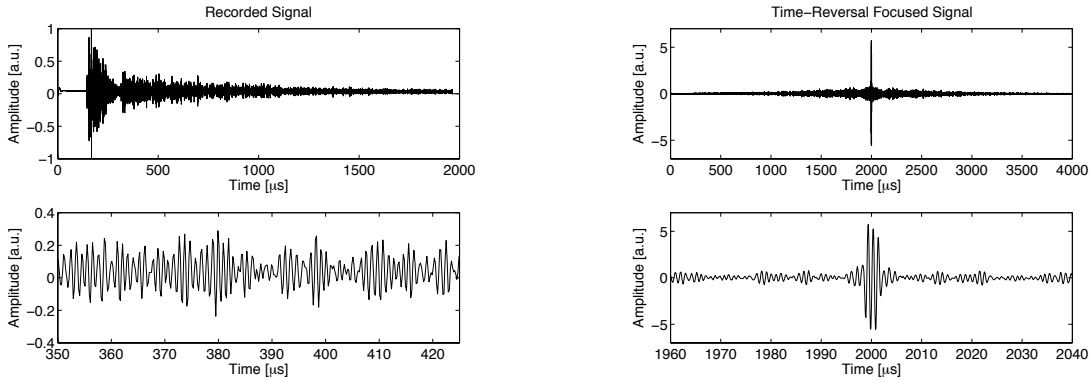

(a) (b)

Figure 5.8: Signals involved in a time-reversal experiment. (a) Acoustic emission from a TRCC. This signal is time-reversed and retransmitted. (b) Time-reversal focused acoustic emission. Both plots use the same amplitude units. One can see that the time-reversal focused emission is approximately six times larger in magnitude.

put in contact with a water bath, some of the signal will be transmitted out of the cavity as it impinges on the cavity wall. Just as the signal at any point on the wall is unique, the signal recorded at any position in the water will also be unique. The signal can be recorded by a hydrophone. Since the signal must be recorded with a hydrophone, this is an invasive method of aberration correction if it were to be done in tissue. Alternatively, one can record the signals in a water path and transmit them into tissue, making the common ultrasound assumption that tissue is well modeled by water.

Figure 5.8a shows a sample signal recorded in water. Often times these signals from a few microsecond long pulse last for a few hundred to a few thousand microseconds. The signal is then time-reversed, windowed, and normalized before being retransmitted. If one envisions the signals composing the recorded waveform as corresponding to travel down particular acoustic paths, then time-reversal effectively sends out the signals for the longest paths first and then the signals for the shorter paths. Simple time-reversal ensures, under linear, nonattenuating conditions, that the timing is such that each signal will travel its path such that all paths

are completed simultaneously. This results in strong, but imperfect, constructive interference of all of the transmitted signals. We will call this process the canonical TRCC experiment. Figure 5.8b shows a time-reversal focused signal. Figures 5.8a and 5.8b use the same amplitude units. Clearly constructive interference is occurring given that the time-reversal focused signal is approximately six times larger than the maximum of the original signal. Additionally, temporal side lobes are present. This is because when each signal is transmitted, it will travel down both the correct paths and incorrect paths. As a result, the signal will also arrive at incorrect times. This is the incoherent noise described in chapter IV. The time-reversal experiments were performed using an HP33120A arbitrary function generator (Agilent, Palo Alto, CA, USA) to transmit a short tone burst to a 50 or 55 dB power amplifier (A-300, ENI, Rochester, NY, USA or Model 350, Matec, Northborough, MA, USA). The amplified signal was then applied to the transducer elements. The signals were recorded with a hydrophone (PVF_2 , Raytheon Co., Waltham, MA, USA) connected to an oscilloscope (9314L, Lecroy, Chestnut Ridge, NY, USA). The signals were uploaded to a PC and processed using LabVIEW (National Instruments, Austin, TX, USA). The time-reversed waveforms were then downloaded to the arbitrary function generator for transmission.

Having seen in fig. 5.8b that it is possible to focus a signal temporally, the ability to focus throughout a 3D volume was investigated. The canonical TRCC experiment was performed at five different spatial locations over a 1 cm^2 area. In addition to recording the time-reversal focused signal at the original locations, they were also recorded at nearby points to form a directivity pattern. Figure 5.9 plots the directivity pattern ($\max_{\text{time}}\{\psi^{TRF}(x_o,t)\}$) as gray points. A second set of directivity patterns (hollow points) were obtained by sending a short burst into the cavity and recording the emission (i.e. no time-reversal is performed). It is seen that time-reversal focusing greatly enhances the maximum signal at a given focal point.

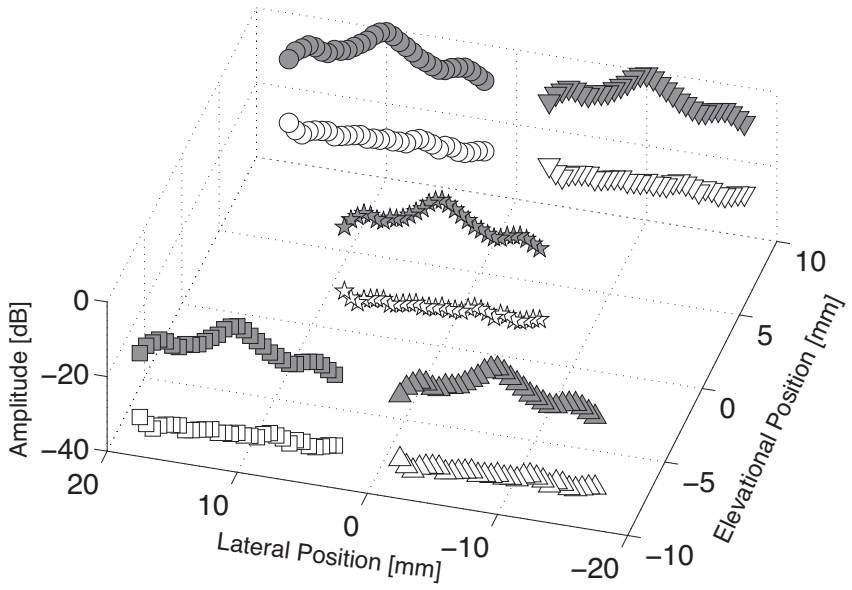

Figure 5.9: Directivity patterns for focusing at five different spatial locations over a 1 cm^2 area (gray points). The full-width half-max is between 5 and 7 mm for all cases. The hollow points show the directivity pattern measured at the five different spatial locations when just transmitting a pulse into the cavity and not an appropriate time-reversed signal.

Next, the impulse response was recorded for two different locations. These impulse responses were summed before time-reversing and then retransmitted to determine the focusing. The results are in fig. 5.10. It is seen that focusing at two different locations can be performed simultaneously with a TRCC. It should be noted that the two peaks are not equal in magnitude. This can be corrected by scaling the impulse responses before summing them.

5.2.3 Time-Reversal Chaotic Cavity Aberration Correction

A final set of experiments were performed to demonstrate aberration correction with a TRCC. The canonical TRCC experiment was performed and the c-plane scanned (fig. 5.11b, bottom). Then an *ex vivo* human skull was placed between the TRCC and the hydrophone (fig. 5.11a). The c-plane was again scanned. The acoustic field was entirely defocused (fig. 5.11c, bottom). Finally, a canonical TRCC experiment

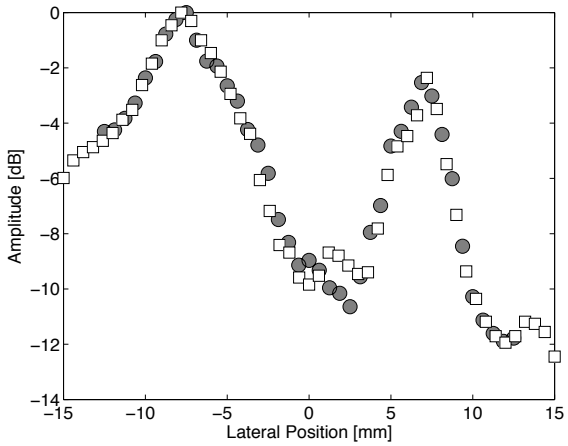

Figure 5.10: Directivity patterns for focusing at two different spatial locations simultaneously. Note that the experiment was performed twice (circle versus square data points) to assess repeatability.

was performed with the skull in place and the c-plane scanned (fig. 5.11d, bottom). It was found that the signal was refocused, although the amplitude was diminished due to the insertion loss of the skull. Figure 5.11 also shows the rf-lines at the intended focus for each case. The fact that a TRCC can be used to focus through a skull is not entirely surprising because to a certain degree, the skull acts as yet another scatterer in the multiple scattering problem. Even so, it is important to note this ability because the skull is a high insertion loss material, and therefore a significant portion of the transmitted signal never arrives at the hydrophone. Therefore under these conditions, this result shows that the loss from the skull is tolerable.

5.2.4 Conclusions

A variety of experimental results concerning the focusing abilities of TRCCs have been demonstrated. The ability to focus throughout a volume has been demonstrated. It was also seen that multiple simultaneous focal spots could be created. However, these focal spots may have different peak magnitudes. Based on chapter IV, one could compute whether the observed peaks fall within the expected

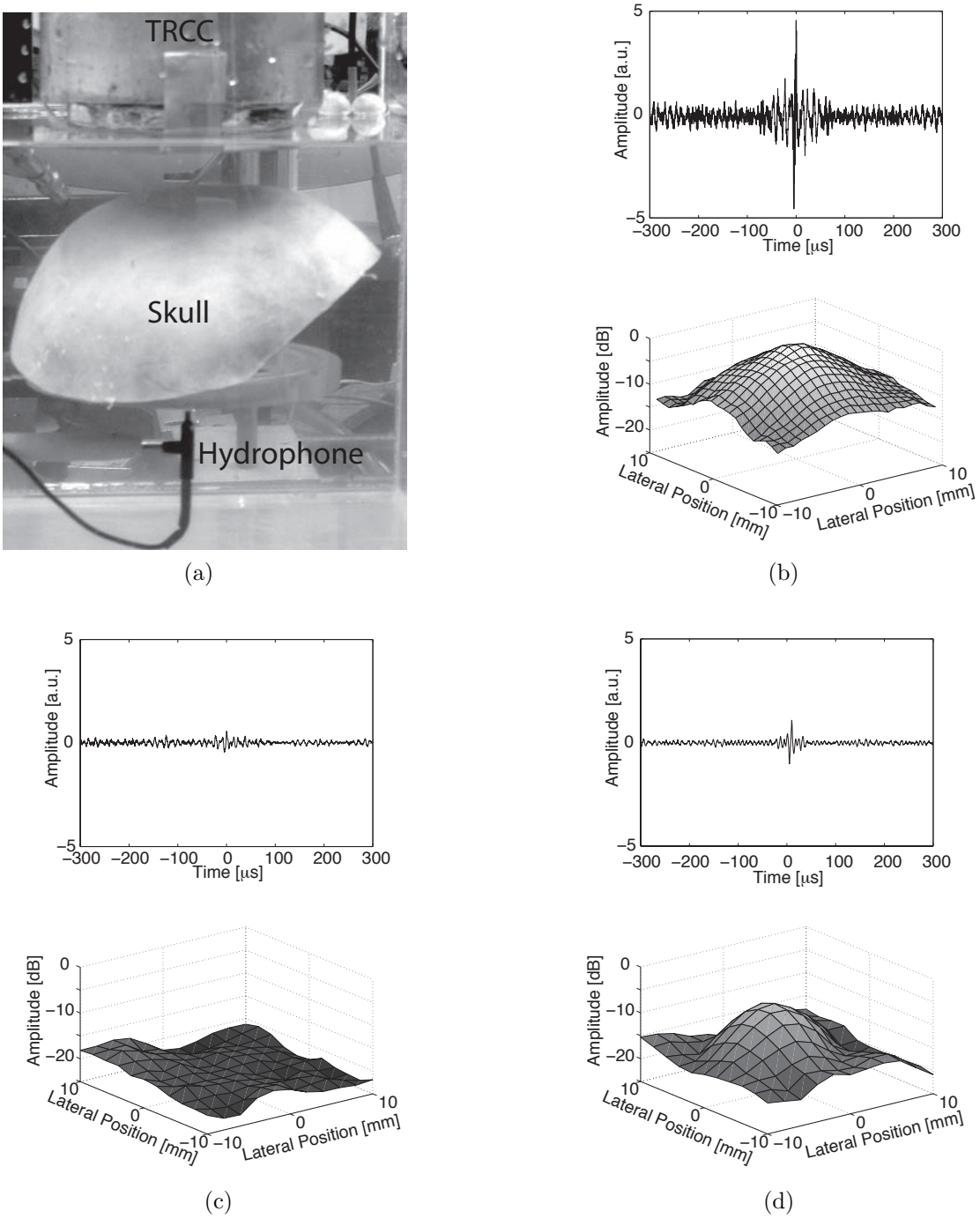

Figure 5.11: (a) Photograph of the setup. (b)-(d) RF-signals and c-plane beam patterns involved in the time-reversal experiments. (b) Time-reversal focused signal without the skull. (c) Transmitting the same signals as (b), but with the skull in place. Complete defocusing is observed. (d) Time-reversal focused signal obtained with the skull in place. The signal is refocused, but smaller due to the losses from the skull.

coherent variance or if the cavity preferentially transmits to a particular location due to its geometry. In either case, one can normalize for this difference when summing the two recorded signals so that equal spot sizes are attained. The ability of a TRCC to focus through a lossy medium (an *ex vivo* human skull) was also observed.

5.3 Acknowledgments

The ultra high-speed camera work was supported in part by NIH Grants R33CA112144, R21CA116043, and S10RR022425-01A1 and a Rackham Pre-Doctoral Fellowship from the Rackham Graduate School at the University of Michigan. The experimental TRCC work was supported in part by NIH Grants R21CA116043 and R21EB002787 and an Applied Physics Fellowship from the Applied Physics Program at the University of Michigan.

REFERENCES

[1] O. D. Kripfgans, J. B. Fowlkes, D. L. Miller, O. P. Eldevik, and P. L. Carson, "Acoustic droplet vaporization for therapeutic and diagnostic applications," *Ultrasound in Medicine and Biology*, vol. 26, no. 7, pp. 1177–1189, 2000.

[2] O. D. Kripfgans, J. B. Fowlkes, M. Woydt, O. P. Eldevik, and P. L. Carson, "*In vivo* droplet vaporization for occlusion therapy and phase aberration correction," *IEEE Transactions on Ultrasonics, Ferroelectrics, and Frequency Control*, vol. 49, no. 2, pp. 726–738, 2002.

[3] T. Giesecke and K. Hynynen, "Ultrasound-mediated cavitation thresholds of liquid perfluorocarbon droplets *In Vitro*," *Ultrasound in Medicine and Biology*, vol. 29, no. 9, pp. 1359–1365, 2003.

[4] O. D. Kripfgans, M. L. Fabilli, P. L. Carson, and J. B. Fowlkes, "On the acoustic vaporization of micrometer-sized droplets," *Journal of the Acoustical Society of America*, vol. 116, pp. 272–281, July 2004.

[5] A. H. Lo, O. D. Kripfgans, P. L. Carson, E. D. Rothman, and J. B. Fowlkes, "Acoustic droplet vaporization: Effects of pulse duration and contrast agent," *IEEE Transactions on Ultrasonics, Ferroelectrics, and Frequency Control*, vol. 54, pp. 933–946, May 2007.

[6] T. Porter and P. Zhang, "Temperature and size-dependence of the vaporization threshold of phase-shift emulsions," *Journal of the Acoustical Society of America*, vol. 123, p. 2997, May 2008.

[7] M. L. Fabilli, K. J. Haworth, N. H. Fakhri, O. D. Kripfgans, P. L. Carson, and J. B. Fowlkes, "The role of inertial cavitation in acoustic droplet vaporization," *IEEE Transactions on Ultrasonics, Ferroelectrics, and Frequency Control*, vol. Accepted, 2009.

[8] K. J. Haworth and O. D. Kripfgans, "Initial growth and coalescence of acoustically vaporized perfluorocarbon microdroplets," *IEEE Ultrasonics Symposium*, vol. 1, 2008.

[9] K. J. Haworth, O. D. Kripfgans, D. D. Steele, and S. D. Swanson, "Acoustically induced tissue displacement for shear wave elasticity imaging using MRI," *Journal of the Acoustical Society of America*, vol. 118, p. 1942, September 2005.

[10] O. D. Kripfgans, K. J. Haworth, D. D. Steele, and S. D. Swanson, "Magnetic resonance elastography using time reversed acoustics," *Proceedings of SPIE: Medical Imaging*, vol. 5746, pp. 1–10, 2005.

[11] O. D. Kripfgans, C. M. Orifici, P. L. Carson, K. A. Ives, O. P. Eldevik, and J. B. Fowlkes, "Acoustic droplet vaporization for temporal and spatial control of tissue occlusion: A kidney study," *IEEE Transactions on Ultrasonics, Ferroelectrics, and Frequency Control*, vol. 52, pp. 1101–1110, July 2005.

[12] M. Zhang, K. J. Haworth, J. B. Fowlkes, M. L. Fabilli, O. D. Kripfgans, W. W. Roberts, and P. L. Carson, "Superselective tissue occlusion by acoustic droplet vaporization (ADV)," *8th International Symposium on Therapeutic Ultrasound*, September 2008.

[13] K. J. Haworth, J. B. Fowlkes, P. L. Carson, and O. D. Kripfgans, "Towards aberration correction of transcranial ultrasound using acoustic droplet vaporization," *Ultrasound in Medicine and Biology*, vol. 34, pp. 435–445, March 2008.

[14] K.-I. Kawabata, R. Asami, T. Azuma, H. Yoshikawa, and S.-I. Umemura, "Cavitation assisted HIFU with phase-change nano droplet," *IEEE Ultrasonics Symposium*, vol. 1, 2008.

[15] V. Bjerknes, *Fields of Force*. New York: Columbia University Press, 1906.

[16] L. A. Crum, "Bjerknes forces on bubbles in a stationary sound field," *Journal of the Acoustical Society of America*, vol. 57, no. 6, pp. 1363–1370, 1975.

[17] G. Montaldo, P. Roux, A. Derode, C. Negreira, and M. Fink, "Ultrasound shock wave generator with one-bit time reversal in a dispersive medium, application to lithotripsy," *Applied Physics Letters*, vol. 80, pp. 897–899, February 2002.

CHAPTER VI

Conclusions and Future Work

6.1 Introduction

The work presented in chapters II and III provide proof of principle that ADV bubbles can be used to focus waveforms on both transmit and receive. Initially, Kripfgans *et al.* [1] and Psychoudakis *et al.* [2] explored the likelihood of using ADV bubbles for aberration correction. The work herein demonstrates that they can be used. The implications are wide ranging, with applications in both diagnostic and therapeutic ultrasound. The feasibility of both applications *in vivo* is supported by recent work [3]. It was shown there that droplets can be vaporized transcutaneously at depth using an intravenous injection.

The diagnostic applications are naturally more difficult as they require focusing on transmit and receive. The difficulty of receive focusing is that one must either measure (as was done in chapter III) or estimate the unaberrated wavefront to determine the aberration. For isotropically scattering ADV bubbles, the waveform can be estimated as a spherical wave. However, to accurately reconstruct an image with simple algorithms, the aberrations must be random and not beam-steering type aberrations (e.g., a wedge of tissue that has a different speed of sound). Beam-steered aberrated wavefronts are spherical, however the center of the spherical wavefront is no longer at the bubble for a homogenous backpropagation. More recently developed correction algorithms such as MUSIC may be used to address these problems and

may also allow for super-resolution imaging [4; 5].

Application to therapeutic ultrasound is simpler and can be undertaken with an IV injection of ADV droplets. The therapeutic array can then be used to vaporize a sparse distribution of droplets. The resulting bubbles can then be used to determine aberrations, and subsequently focus the ultrasound more effectively. For applications in histotripsy where the treatment amplitudes can be significantly larger *in situ* than the ADV vaporization threshold [6], it may be possible to achieve amplitudes sufficient to vaporize droplets but not initiate histotripsy cavitation activity. Using ADV-based aberration correction, the US amplitudes can be increased in the focal volume and it may then be possible to initiate histotripsy under conditions not otherwise possible due to limited aperture and aberrations. This may open new areas of the body to being treated via histotripsy. For applications in thermal ablation (HIFU), the ADV threshold and HIFU amplitudes are similar [7], but ADV can be accomplished with much shorter pulses. In this case, ADV-based aberration correction will allow for better targeting and decreased treatment times due to more efficient deposition of ultrasound energy.

One possible concern with therapeutic ultrasound that has not been addressed herein is nonlinear scattering and propagation. Nonlinear scattering can occur from both tissue and, more strongly, from bubbles, such as those produced by ADV. Nonlinear scattering produces harmonics of the transmit frequency, which can propagate back to the array. Assuming the propagation is linear, time-reversal acoustics can take advantage of nonlinear scattering from ADV bubbles to obtain focusing information for both the transmitted frequency and the harmonics. If a particular medium is too aberrating to adequately focus a signal at depth at a relatively higher frequency, one can transmit at lower frequencies and listen for the harmonics scattered by the bubble. The scattered harmonic can be selected with a filter and time-reversed. Since the scattered harmonic propagated through the

aberrating medium to arrive at the array, it will focus correctly back to the bubble. The transmitted harmonic will produce its own harmonics upon scattering from the bubble. If this process is repeated, one can continue to increase the operational frequency until she/he has arrived at the frequency of choice. Additionally, it has been shown that time-reversal is an effective means of identifying nonlinear scatterers for nondestructive testing [8]. In these manners, nonlinear scattering and time-reversal acoustics can be used in conjunction. Nonlinear propagation can also be accounted for with time-reversal acoustics, assuming a nonviscous (i.e. lossy) medium. As shown by Tanter et al. [9], the nonlinear nonviscous wave equation is time-reversal invariant (unless shocking occurs). This can be imagined by the fact that during nonlinear propagation, the compressional portion of the wave propagates faster, while the rarefactional portion propagates slower to form the typical N-wave. Upon time-reversal the faster compressional parts of the N-wave are transmitted later than the rarefactional portions and as they 'catch-up' the nonlinearities disappear resulting in the original waveform. In tissue however, viscous losses are always present and as a result, time-reversal invariance is violated. Like the lossy skull, however, it may be that the waveforms can still be substantially refocused. Further analysis of this problem, based on specific assumptions about the nonlinearity of the medium and its other acoustic properties, is a suggested field for future work.

A second limitation to therapeutic applications is the need for 2D arrays with individually programable elements. This limitation provided the motivation for chapter IV and the second half of chapter V. These sections described the capabilities of time-reversal chaotic cavities to focus arbitrary signals. As shown in chapter V, with an appropriate method of obtaining the signal propagated from the element of the TRCC to a location *in vivo* or *in vitro*, aberration correction can be performed. This may be done in practice by illuminating an ADV bubble and recording the signal scattered from the bubble with the TRCC. Unfortunately, due to the pulse

spreading associated with the initial step in a TRCC experiment and the small echo that bubble point-targets produce, this signal will be very small and very low noise detection electronics will need to be employed. However, time-reversal of this signal will then allow for focusing on the bubble. In this manner, the outcomes of chapter II can be translated to a TRCC.

The specific contributions of this dissertation and suggested future directions of study are now described.

6.2 Transcranial Acoustic Droplet Vaporization

6.2.1 Results

To be able to perform ADV-based aberration correction, it is necessary to create ADV bubbles *in vivo*. In chapter II, the skull was chosen to demonstrate that ADV can be performed in regions traditionally thought of as highly inaccessible to ultrasound. By demonstrating the ability to vaporize through an *ex vivo* human skull, it is likely that schemes can be found for vaporizing in many locations within the human body. Here it was found that the combination of ultrasound contrast agent and long pulses resulted in ADV. These parameters were chosen based on the work of Lo *et al.* and indicated that cavitation external to the droplets initiated vaporization [10].

6.2.2 Future Directions

It is recommended that additional studies be performed to determine under what conditions aberrated ADV should be performed. To begin, it should be noted that there appear to be two different frequency regimes for performing ADV. Figure 6.1a shows that the vaporization thresholds for studies with relatively short pulses [10; 11] have a decreasing threshold with increasing frequency. In what may be another regime, with long pulses the threshold increases with increasing frequency

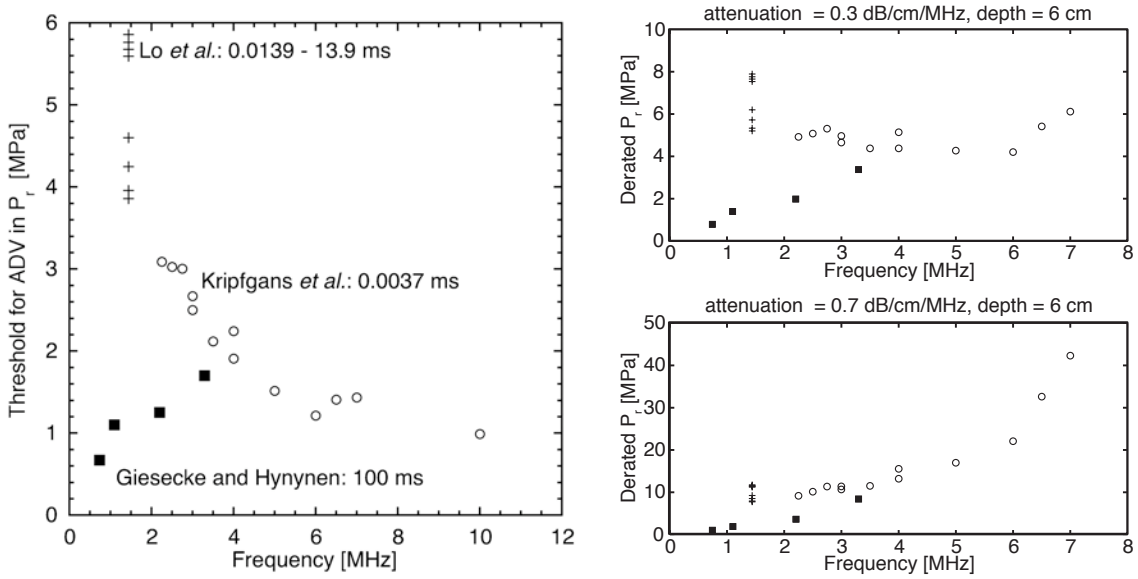

(a) (b)

Figure 6.1: (a) ADV threshold as a function of frequency as measured by Kripfgans *et al.* [11] (circle), Giesecke and Hynynen (square) [12], and Lo *et al.* (cross) [10]. The pulse duration used for each set of data is shown next to each data set. (b) Simulated pressures that need to be achieved in a water path for vaporization if 6 cm of 0.3 dB/cm/MHz or 0.7 dB/cm/MHz attenuating material is placed between the transducer and focal spot.

(consistent with inertial cavitation theory) [12]. It appears that below 4 MHz the pathway of Giesecke and Hynynen can occur first. This would be the frequency range investigated for transcranial ADV. For alternative applications however, higher frequencies may be more favorable since the threshold decreases. Depending on the tissue however, the derated ADV threshold may not decrease due to frequency dependent attenuation (fig. 6.1b). Therefore the specific application should be identified before studying the parameters that will lead to the best ADV.

It would also be desirable in future work to eliminate the need for using UCA. Use of UCA is complicating for two reasons. First it requires an as yet undetermined proximity between the UCA and ADV droplet. Second, the presence of UCA increases the amount of scatter and therefore may make it more difficult to isolate the echo from an ADV bubble for aberration correction. Further study of the

vaporization pathways, such as the first part of chapter V, should lend greater insight into reducing the ADV threshold appropriately.

6.3 Transcranial Transmit Aberration Correction

6.3.1 Results

Chapter II investigated the ability to perform transcranial transmit aberration correction. The first result of this work was the design of a setup that allowed for the creation and placement of single microbubbles in an ultrasound field of view. This allowed the study of aberration correction. Using a synthetic aperture setup, transcranial transmit aberration correction was performed. Unfocused 38.1 mm diameter transducers were used for transmit and receive. Focal gains of 1.9 ± 0.3 were obtained. Phase averaging that occurred across the large transducers likely limited the focal gain.

6.3.2 Future Directions

Several hardware upgrades are recommended to improve and further test transmit aberration correction. First, the use of smaller transducers is recommended. The tradeoff for decreasing phase averaging (by using smaller transducers) is the decrease in transmit power than can be achieved. The large reflection and attenuation of the skull makes this a considerable concern. Others have developed transducers that balance this trade off and thus act as template for future work [13]. More critical perhaps is the development of an array-based system with arbitrary transmitting and receiving. The two, single-element, synthetic aperture arrangement used required approximately ten minutes to complete an experiment. It was found that bubbles smaller than approximately 75 microns tended to dissolve too quickly for the experiments to be carried out. This was not a significant issue for the experiments performed here because the 75-200 micron bubbles were still significantly smaller

than a wavelength at the 1 MHz transmit frequency used. For applications using higher frequencies however, smaller bubbles are required so that they remain point-scatterers [2]. A quicker, array-based system would also be beneficial for *in vivo* testing where breathing and other body motions must be taken into account. In addition to a quicker, array-based system, increasing the sensitivity of the transducers and the signal-to-noise (SNR) of the electronics should lead to better results. This would allow for better signal detection for signal subtraction. The presence of noise limited the focal gain achieved for certain rf-lines.

In addition to hardware upgrades, the coupling of transcranial ADV and aberration correction into one system is a natural next step. Not only would this lead to an easier to operate system, but also a more practical system for *in vivo* work.

6.4 Aberration Corrected Imaging

6.4.1 Results

The focus of chapter III was on creating an aberration corrected image. This was performed using an array-based synthetic aperture setup. The algorithms employed used the same data set for both imaging and aberration correction.

Initially, several parameters concerning image formation were analyzed. In particular, the focus was on the practical implementation of image formation. Many of the results mirrored those found in standard delay-and-sum beamforming. This included the need to implement apodization and requirements on element spacing. An appropriate filter for envelope detecting signals with large dynamic ranges was also developed.

Next, the decomposition of the time-reversal operator (DORT) algorithm was implemented. Here, a main focus was on appropriately using single versus multiple frequencies to determine what aberrations occurred. It was found that using a

multiple frequency approach could provide a more robust mechanism for identifying aberrations. Implementation of the DORT algorithm on only a portion of the rf-data was also investigated. This was found to be a good method to remove possible correlations and/or interference between the desired scatterer and any other interference such as speckle or reverberations.

Combining these approaches, aberration corrected images were created. The aberrations were induced from electronic time-shifts of the data. It was found that aberrations much larger than typically found in soft tissue could be accurately corrected using the scatterer off of an ADV bubble. Measurement of aberrations was performed based on unaberrated cases.

6.4.2 Future Directions

Electronic aberration was used in this work because of violations of spatial reciprocity in the rf-lines. This violation appeared to be due to attenuation resulting from the physical aberrator. Therefore a priority for this work, as is common in synthetic aperture imaging, is the increase of SNR/penetration depth. This is particularly critical as the reported experiments used polyacrylamide gel and ultrasound gel, both of which have low attenuation coefficients. Any future *in vivo* work would need to overcome soft tissue attenuation.

Several options may be pursued for increasing the SNR [14]. This includes using coded-excitation. In this case matched-filtering can be applied to the received signals. This results in a pulse-compressed signal. This is a common approach in SONAR and RADAR [15]. Alternatively, rather than firing single elements, multiple elements may be banded together on transmit to increase the amplitude of the transmitted signal. The gain may be proportional to the square root of the number of elements used [16]. Finally, since most attenuation in medical ultrasound increases with frequency, obtaining lower frequency probes will allow for increased signal penetration.

A second issue that must be dealt with is appropriately modeling the scatter from a bubble in DORT. For small enough bubbles, it is possible to model the scatterer as a point-source. As Psychoudakis *et al.* showed theoretically, bubbles with a $ka > 1$ can no longer be considered an isotropic scatterer [2]. This limit should be tested experimentally. This non-isotropic scatterer should also be modeled for its impact on the DORT algorithm. Then instead of assuming a circular or parabolic fit to the DORT 'temporal eigenvectors', a more appropriate fit can be made. This would relieve the need to fit the aberrated case to an unaberrated case.

Upon correction of the aforementioned issues, and repetition of the experiments in materials with appropriate background scatter to mimic soft tissue speckle, the experiments should be performed *in vivo*. *In vivo* measurements are important to determine two important points. First, what is the size of the isoplanatic patch *in vivo*. This will clearly depend on the level of aberration, however it would be important to develop a rule-of-thumb as to the density/sparsity of bubbles needed to correct an entire image. This density will play an important role in the dose of ADV droplets given. Second, when droplets are vaporized and trapped in a capillary, do they still represent an isotropic scatterer, or at least one that can be modeled properly to allow aberrations to be measured and therefore corrected.

6.5 Multiple-scattering Time-Reversal

6.5.1 Results

In chapter IV a model was developed to describe the ability to perform time-reversal focusing in a multiple scattering medium (e.g., a TRCC) using arbitrary input functions and windowing. This model is an extension of the shot-noise model developed by Derode *et al.* [17]. The model was developed and examples were given to demonstrate its applicability to TRCCs and also that it matched numerical simulations of an ideal shot-noise process. Several important points were noted.

First, it was seen that the noise associated with these processes can be classified into an incoherent and coherent part. The incoherent part of the noise can be considered to be the result of acoustic waves propagating down incorrect paths. The coherent noise can be associated with the variance in the distribution of energy for an ensemble of transmits. It was observed that the coherent noise always contributed at the main lobe of the signal. The incoherent noise was found to always peak at a location based on the windowing and therefore could be made to occur at or far from the main-lobe.

A set of parameters common in time-reversal multiple scattering experiments was applied to the model. This allowed for additional simplifications that further elucidated how various parameters impacted the quality of time-reversal focusing. These parameters were investigated for their impact on the signal magnitude, noise magnitude, and SNR. Several of the results are qualitatively consistent with other models. This includes the improvement in SNR with increasing window width and decay constant of the recorded signal. One key finding is that the SNR scales approximately with the pulse-intensity integral. It had previously been assumed that multiple-scattering time-reversal with tone bursts would not be successful because the signal is narrow band (and thus mimics phase-conjugation rather than broadband time-reversal). However the dependence on the pulse-intensity integral implies that even if one were to design a broadband long pulse, the SNR would not be relatively large.

6.5.2 Future Directions

It has been found that the model developed by Derode *et al.* breaks down due to long range correlations in the signal [17; 18]. By adjusting various parameters in the model, it was seen that the shot-noise model could still be applied. It would be of interest to experimentally test the break down of the model developed here in relation to long range correlations. This is particularly interesting since the input

signal itself can be considered to induce long range correlations.

Application of the model to optimizing the SNR for long pulses is also of great practical interest. This would include both HIFU and acoustic radiation force experiments. If it can be shown that large amplitude pulses with good SNR can be created using a TRCC or other multiple scattering medium, it may be possible to replace the need for large, high-power piezoelectric ceramics and composites. It would also allow for steering throughout a 3D volume.

6.6 Summary of Contributions

ADV-based aberration correction has been demonstrated to be a feasible technique. Additionally, focusing arbitrary signals via multiple-scattering time-reversal has been modeled. This has lead to the following results in this dissertation.

- Under appropriate acoustic conditions, ADV can be performed through an *ex vivo* human skull.
- Single gas or ADV bubbles can be used to correct the aberrations due to an *ex vivo* human skull.
- It is possible to develop and implement an aberration correction algorithm for aberration corrected imaging based on ADV and TRA. This can be achieved using a single synthetic aperture data set.
- A model for describing multiple-scattering time-reversal focusing with arbitrary inputs and windowing has been created.
- The multiple-scattering model has been applied to a common set of parameters. It was found that focusing long-pulses is difficult, even with high bandwidth.
- Time-reversal chaotic cavities can be used to focus throughout a volume and to focus at multiple locations simultaneously. They can also be used to focus

through an *ex vivo* human skull.

- Bubbles resulting from ADV are highly dependent on the vaporization pulse used. A small change in the vaporization pulse (using two to thirteen cycles) can have a substantial impact on the resulting bubbles. Additionally, nearby droplets may coalesce during the vaporization process.

REFERENCES

[1] O. D. Kripfgans, J. B. Fowlkes, M. Woydt, O. P. Eldevik, and P. L. Carson, "*In vivo* droplet vaporization for occlusion therapy and phase aberration correction," *IEEE Transactions on Ultrasonics, Ferroelectrics, and Frequency Control*, vol. 49, no. 2, pp. 726–738, 2002.

[2] D. Psychoudakis, J. B. Fowlkes, J. L. Volakis, and P. L. Carson, "Potential of microbubbles for use as point targets in phase aberration correction," *IEEE Transactions on Ultrasonics, Ferroelectrics, and Frequency Control*, vol. 51, pp. 1639–1648, December 2004.

[3] M. Zhang, K. J. Haworth, J. B. Fowlkes, M. L. Fabilli, O. D. Kripfgans, W. W. Roberts, and P. L. Carson, "Superselective tissue occlusion by acoustic droplet vaporization (ADV)," *8th International Symposium on Therapeutic Ultrasound*, September 2008.

[4] M. Cheney, "The linear sampling method and the MUSIC algorithm," *Inverse Problems*, vol. 17, no. 591, p. 595, 2001.

[5] F. K. Gruber, E. A. Marengo, and A. J. Devaney, "Time-reversal imaging with multiple signal classification considering multiple scattering between the targets," *Journal of the Acoustical Society of America*, vol. 115, no. 6, pp. 3042–3047, 2004.

[6] W. W. Roberts, T. L. Hall, K. Ives, J. S. Wolf, J. B. Fowlkes, and C. A. Cain, "Pulsed cavitational ultrasound: A noninvasive technology for controlled tissue ablation (histotripsy) in the rabbit kidney," *The Journal of Urology*, vol. 175, pp. 734–738, February 2006.

[7] M. R. Bailey, V. A. Khokhlova, O. A. Sapozhinikov, S. G. Kargl, and L. A. Crum, "Physical mechanisms of therapeutic effect of ultrasound (a review)," *Acoustical Physics*, vol. 49, no. 4, pp. 369–388, 2003.

[8] T. J. Ulrich, P. A. Johnson, and A. Y. Sutin, "Imaging nonlinear scatterers applying the time reversal mirror," *Journal of the Acoustical Society of America*, vol. 119, no. 3, pp. 1514–1518, 2006.

[9] M. Tanter, J.-L. Thomas, F. Coulouvrat, and M. Fink, "Time reversal invariance of nonlinear acoustic wave propagation in weakly viscous media," *IEEE Ultrasonics Symposium*, vol. 2, pp. 1419–1422, 1999.

[10] A. H. Lo, O. D. Kripfgans, P. L. Carson, E. D. Rothman, and J. B. Fowlkes, "Acoustic droplet vaporization: Effects of pulse duration and contrast agent," *IEEE Transactions on Ultrasonics, Ferroelectrics, and Frequency Control*, vol. 54, pp. 933–946, May 2007.

[11] O. D. Kripfgans, J. B. Fowlkes, D. L. Miller, O. P. Eldevik, and P. L. Carson, "Acoustic droplet vaporization for therapeutic and diagnostic applications," *Ultrasound in Medicine and Biology*, vol. 26, no. 7, pp. 1177–1189, 2000.

[12] T. Giesecke and K. Hynynen, "Ultrasound-mediated cavitation thresholds of liquid perfluorocarbon droplets *In Vitro*," *Ultrasound in Medicine and Biology*, vol. 29, no. 9, pp. 1359–1365, 2003.

[13] M. Pernot, J. F. Aubry, J. L. Thomas, and M. Fink, "High power transcranial beam steering for ultrasonic brain therapy," *Physics in Medicine and Biology*, vol. 48, pp. 2577–2589, 2003.

[14] J. A. Jensen, S. I. Nikolovikolov, K. L. Gammelmark, and M. H. Pedersen, "Synthetic aperture ultrasound imaging," *Ultrasonics*, vol. 44, pp. e5–e15, 2006.

[15] M. Soumekh, *Synthetic Aperture Radar Signal Processing: with MATLAB Algorithms*. John Wiley & Sons, Inc., 1999.

[16] M. Karaman, P.-C. Li, and M. O'Donnell, "Synthetic aperture imaging for small scale systems," *IEEE Transactions on Ultrasonics, Ferroelectrics, and Frequency Control*, vol. 42, no. 3, pp. 429–442, 1995.

[17] A. Derode, A. Tourin, and M. Fink, "Ultrasonic pulse compression with one-bit time reversal through multiple scattering," *Journal of Applied Physics*, vol. 85, pp. 6343–6352, May 1999.

[18] A. Derode, A. Tourin, and M. Fink, "Limits of time-reversal focusing through multiple scattering: Long-range correlation," *Journal of the Acoustical Society of America*, vol. 107, pp. 2987–2998, June 2000.

APPENDICES

APPENDIX A

Time-Reversal Properties of the Convolution Operation: Important Aspects for Time-Reversal Acoustics

A.1 Background

The convolution operation is a functional. A functional, sometimes also called a higher-order function, is defined as a function that 1) takes one or more functions as an input and/or 2) produces an output that is a function. A function is a map that takes a set of scalars as an input and maps them to another set of scalars. Graphically a functional is:

$$\{f(x), g(y)\} \xrightarrow{F} h(z), \tag{A.1}$$

where f, g, and h are functions, x, y, and z are scalars, and F is the functional. An alternative syntax is:

$$F[f, g] = h(z), \tag{A.2}$$

where f and g are the input functions and $h(z)$ is the output function. The inputs to f and g are purposefully not included in this general notation because they will depend on the specific definition of the functional F. Based on the definition above a functional may:

1. take one or more functions as an input and then outputs a scalar

2. take one or more functions as an input and then outputs a function

3. take one or more scalars as an input and then outputs a function

The convolution functional (or more commonly referred to as the convolution operation) fits the second definition above. The input is two functions, which each have a single scalar as an input. The output is a single function, which has a single scalar as an input. The convolution operation is specifically defined as:

$$r(t) = R[f, g] = \int_{-\infty}^{\infty} f(\tau)g(t - \tau)\ d\tau. \tag{A.3}$$

A.2 Notation

The symbol $\otimes$ will be used as short-hand to denote the convolution operation:

$$r(t) = R[f, g] = f(t) \otimes g(t). \tag{A.4}$$

Note that this short-hand is a bit of a misnomer. The input arguments, t, to f and g on the right-hand side of the equation are not the same as the input argument, t, for r. This will be explained in more detail below.

A.3 Commutative property

Recall that $f(t) \otimes g(t) = \int_{-\infty}^{\infty} f(\tau)g(t - \tau)\ d\tau$, then letting $\tau' = t - \tau$:

$$\begin{aligned} f(t) \otimes g(t) &= -\int_{\infty}^{-\infty} f(t - \tau')g(\tau')\ d\tau' && \text{(A.5)} \\ &= \int_{-\infty}^{\infty} g(\tau')f(t - \tau')\ d\tau' && \text{(A.6)} \\ &= \int_{-\infty}^{\infty} g(\tau)f(t - \tau)\ d\tau && \text{(A.7)} \\ &= g(t) \otimes f(t). && \text{(A.8)} \end{aligned}$$

Therefore: $f(t) \otimes g(t) = g(t) \otimes f(t)$ and it can be seen that **the convolution operation is commutative**

A.4 Time-Reversal and the convolution operation

First, note that there are multiple ways that time-reversal can occur with functionals. Time-reversal may refer to reversing the argument of the output function of the functional or reversing the argument of one or both of the input functions of the functional.

A.4.1 Time-reversing the argument of the output function of a convolution

Recall the definition of the convolution operation eqn. A.3:

$$r(t) = \int_{-\infty}^{\infty} f(\tau)g(t-\tau)\ d\tau.$$

Based on this definition, time-reversing the argument of the output function of the convolution operation yields:

$$r(T-t) = \int_{-\infty}^{\infty} f(\tau)g((T-t)-\tau)\ d\tau. \tag{A.9}$$

How does this relate to the short-hand notation? Is it $r(T-t) = g(t) \otimes f(T-t)$ or $g(-t) \otimes f(T-t)$ or $g(T-t) \otimes f(T-t)$ or even something else? Looking at some numerical examples of convolution can help determine what form is expected to be correct. Figure A.1 shows the numerical input functions. Figure A.2 shows some graphical representations of various convolution possibilities.

From these plots, it can be seen that the sum of the time-shifts of the input functions must match the time-shift of the output function. For example shifting the output function by T can be obtained from $a(T-t) \otimes b(-t)$, $a(-t) \otimes b(T-t)$, and

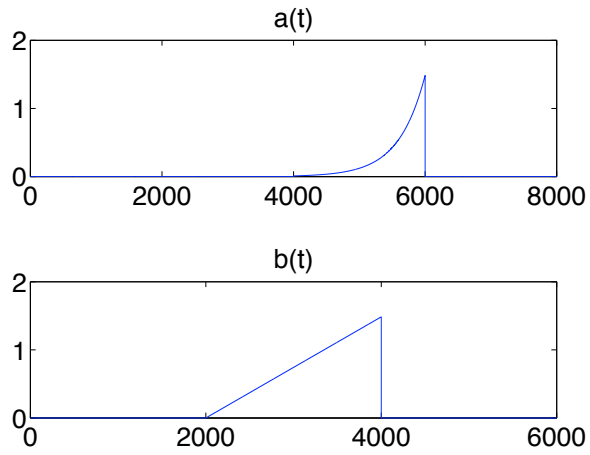

Figure A.1: The input functions a and b for the convolution operation.

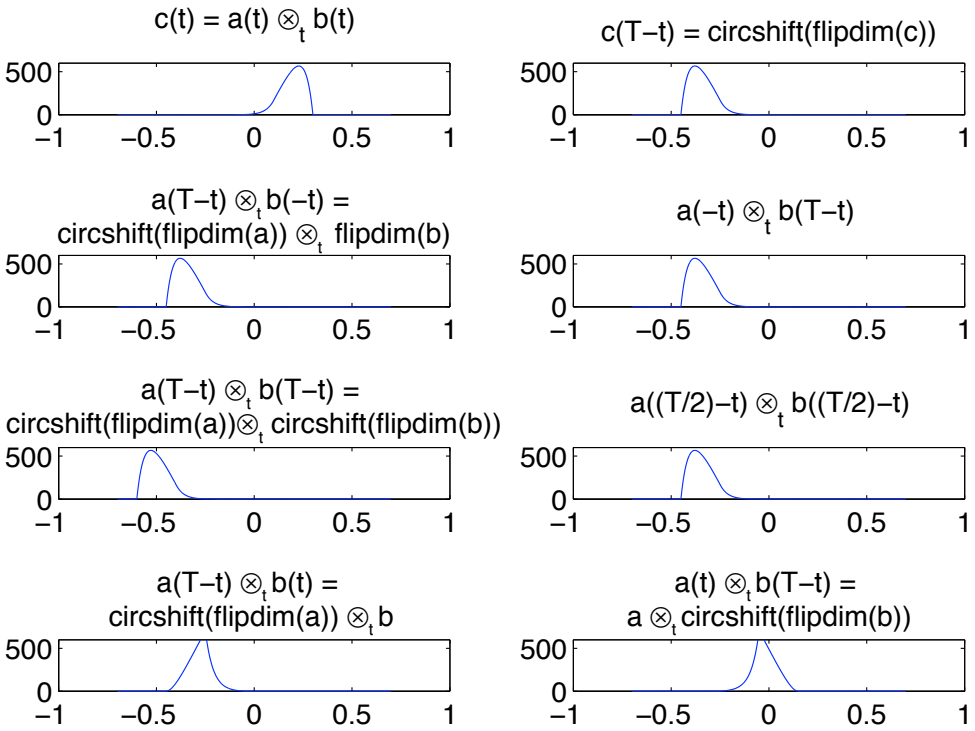

Figure A.2: The resulting convolution for various combinations of time-shifting and time-reversing the input functions a and b are shown. They are compared to the original convolution $c(t)$ and a time-shifted and time-reversed version $c(T-t)$ (top left and right plots). Note that if only one of the input functions is time-reversed, the output function is not the correct shape (bottom left and right plots). Also, if both input functions are shifted by T then the output function is shifted by $2T$ (second from the bottom on the left).

$a(^T/_2 - t) \otimes b(^T/_2 - t)$. Additionally, note that both of the input variables of the input functions must be time-reversed. Given this qualitative understanding, these results can be proven explicitly.

Time-shift associated with $g(t)$: $r(T-t) = g(T-t) \otimes f(-t) = f(-t) \otimes g(T-t)$

Beginning with eqn. A.9:

$$\begin{aligned} r(T-t) &= \int_{-\infty}^{\infty} f(\tau) g((T-t)-\tau)\ d\tau && \text{(A.10)} \\ &= \int_{-\infty}^{\infty} f(-(t-\tau')) g(T-\tau')\ d\tau' && \text{(A.11)} \\ &= \int_{-\infty}^{\infty} g(T-\tau) f(-(t-\tau))\ d\tau && \text{(A.12)} \\ &\equiv g(T-t) \otimes f(-t). && \text{(A.13)} \end{aligned}$$

The substitution $\tau' = t + \tau$ is used to go from eqn. A.10 to eqn. A.11. From this, one can also begin to see how the short-hand notation is properly used. It is seen that time-reversal of the t in the output function causes both t and τ to change signs in the integrand functions. However, the time-shift T remains the same sign and can be added to the start of the function that does not contain t (in this case f). Note that this result matches the intuition gained from figure A.2.

Given this understanding of the short-hand notation one might suspect that $r(T-t) = f(-t) \otimes g(T-t)$ can be written as:

$$r(T-t) = f(-t) \otimes g(T-t) = \int_{-\infty}^{\infty} f(-\tau) g(T-(t-\tau))\ d\tau, \qquad \text{(A.14)}$$

where the time-shift T has been added to the function that contains t (in this case

g). This is proven by again beginning with eqn. A.9:

$$\begin{aligned} r(T-t) &= \int_{-\infty}^{\infty} f(\tau)g((T-t)-\tau)\ d\tau && \text{(A.15)} \\ &= \int_{-\infty}^{\infty} f(\tau)g(T-(t+\tau))\ d\tau && \text{(A.16)} \\ &= -\int_{\infty}^{-\infty} f(-\tau')g(T-(t-\tau'))\ d\tau' && \text{(A.17)} \\ &= \int_{-\infty}^{\infty} f(-\tau')g(T-(t-\tau'))\ d\tau' && \text{(A.18)} \\ &= \int_{-\infty}^{\infty} f(-\tau)g(T-(t-\tau))\ d\tau && \text{(A.19)} \\ &\equiv f(-t)\otimes g(T-t). && \text{(A.20)} \end{aligned}$$

The substitution $\tau' = -\tau$ is used in going from eqn. A.16 to eqn. A.17. Thus the interpretation of the relationship between the integral notation and the short-hand notation is self-consistent and also it is consistent with the commutative property of convolutions that was shown earlier in section A.3.

Time-shift associated with $f(t)$: $r(T-t) = f(T-t)\otimes g(-t) = g(-t)\otimes f(T-t)$

One can then make the argument that since the convolution is commutative, it is sufficient to say that the roles of f and g in the above equations A.10 - A.20 can be switched to yield:

$$r(T-t) = f(T-t)\otimes g(-t) = g(-t)\otimes f(T-t). \qquad \text{(A.21)}$$

However, showing this more explicitly from the same starting point, eqn. A.9.

$$r(T-t) = \int_{-\infty}^{\infty} f(\tau)g((T-t)-\tau)\ d\tau \tag{A.22}$$

$$= -\int_{\infty}^{-\infty} f(T-\tau')g(\tau'-t)\ d\tau' \tag{A.23}$$

$$= \int_{-\infty}^{\infty} f(T-\tau)g(-(t-\tau))\ d\tau \tag{A.24}$$

$$\equiv f(T-t) \otimes g(-t). \tag{A.25}$$

The substitution $\tau = T - \tau'$ was used. To complete the set of equivalent ways to write $r(T-t)$:

$$r(T-t) = \int_{-\infty}^{\infty} f(\tau)g((T-t)-\tau)\ d\tau \tag{A.26}$$

$$= -\int_{\infty}^{-\infty} f(T-t+\tau')g(-\tau')\ d\tau' \tag{A.27}$$

$$= \int_{-\infty}^{\infty} g(-\tau)f(T-(t-\tau))\ d\tau \tag{A.28}$$

$$\equiv g(-t) \otimes f(T-t), \tag{A.29}$$

where the substitution $\tau = T - t + \tau'$ was used. To complete the understanding of time-shifting and time-reversing the argument of the output function of the convolution operation one needs to look at splitting the time-shift.

Splitting the time-shift between $f(t)$ and $g(t)$

If $T = T_1 + T_2$ then $r(T - t) = r(T_1 + T_2 - t)$. How does this affect translate into the integral notation and short-hand notation?

$$\begin{aligned} r(T-t) &= \int_{-\infty}^{\infty} f(\tau) g((T-t)-\tau)\, d\tau && \text{(A.30)} \\ &= \int_{-\infty}^{\infty} f(\tau) g((T_1+T_2-t)-\tau)\, d\tau && \text{(A.31)} \\ &= -\int_{\infty}^{-\infty} f(T_2-t+\tau') g(T_1-\tau')\, d\tau' && \text{(A.32)} \\ &= \int_{-\infty}^{\infty} g(T_1-\tau) f(T_2-(t-\tau))\, d\tau && \text{(A.33)} \\ &\equiv g(T_1-t) \otimes f(T_2-t) && \text{(A.34)} \end{aligned}$$

The substitutions $T = T_1 + T_2$ and $\tau = T_2 - t - \tau'$ were used. By using similar substitutions to those already shown, one can show $r(T - t) = f(T_1 - t) \otimes g(T_2 - t)$ and the corresponding integral forms. These are excluded here for brevity.

Additionally, from the above, the following can be surmised:

$$\begin{aligned} g(T_1-t) \otimes f(T_2-t) &\equiv g(-t) \otimes f(T_1+T_2-t) && \text{(A.35)} \\ g(T_1+t) \otimes f(T_2+t) &\equiv g(t) \otimes f(T_1+T_2+t) && \text{(A.36)} \\ g(T_1+t) \otimes f(T_2-t) &\equiv g(t) \otimes f(T_2-T_1-t). && \text{(A.37)} \end{aligned}$$

Summary

From these results, a complete understanding of the various ways of writing out the time-shift and time-reversal of the output function has been attained. Additionally, a complete understanding of how to write this out using the short-hand notation has

been shown.

$$\begin{aligned} r(T-t) &= \int_{-\infty}^{\infty} f(-\tau)g(T-(t-\tau))\ d\tau = f(-t) \otimes g(T-t) && \text{(A.38)} \\ &= \int_{-\infty}^{\infty} f(T-\tau)g(-(t-\tau))\ d\tau = f(T-t) \otimes g(-t) && \text{(A.39)} \\ &= \int_{-\infty}^{\infty} g(T-\tau)f(-(t-\tau))\ d\tau = g(T-t) \otimes f(-t) && \text{(A.40)} \\ &= \int_{-\infty}^{\infty} g(-\tau)f(T-(t-\tau))\ d\tau = g(-t) \otimes f(T-t) && \text{(A.41)} \end{aligned}$$

and:

$$r(T-t) = r(T_1+T_2-t) = f(T_1-t) \otimes g(T_2-t) = g(T_1-t) \otimes f(T_2-t) \quad \text{(A.42)}$$

A.4.2 Convolving functions when only one of them is time-reversed: $f(t) \otimes g(T-t)$

Typically in a time-reversal acoustics experiment the received signal is time-reversed and sent back through the system. From a systems perspective this means that a non-time-reversed function is convolved with another function that is time-reversed. Using the short-hand notation, this is clearly written as $f(t) \otimes g(T-t)$. Based on the above work, this can be written in integral notation as:

$$g(T-t) \otimes f(t) = \int_{-\infty}^{\infty} g(T-\tau)f(t-\tau)\ d\tau, \quad \text{(A.43)}$$

or

$$f(t) \otimes g(T-t) = \int_{-\infty}^{\infty} f(\tau)g(T-(t-\tau))\ d\tau. \quad \text{(A.44)}$$

A.5 Nested Convolutions

In a time-reversal experiment, an output of a system is recorded, time-reversed, and sent back into the system. Thus the original input to the system 'goes through'

the system twice. Each time it goes through, a convolution is performed. Thus nested convolutions will arise. Knowing that nested convolutions will arise, their integral-notation and convolution-notation will be presented. Suppose a system has an impulse-response of $h(t)$. Let $f(t)$ be the input. Then,

$$f(t) \longrightarrow \boxed{h(t)} \longrightarrow f(t) \otimes_t h(t). \tag{A.45}$$

Here the subscript t is included to make it clear that the independent variable for the convolution is t. For nested convolutions, the independent variable is not always t.

To create a sample nested convolution, one can feed the output back into the system. This results in:

$$\Big(f(t) \otimes_t h(t)\Big) \longrightarrow \boxed{h(t)} \longrightarrow \Big(f(t) \otimes_t h(t)\Big) \otimes_t h(t). \tag{A.46}$$

Using the previously outlined notation:

$$\Big(f(t) \otimes_t h(t)\Big) \otimes_t h(t) = \Big(\int_{\tau=-\infty}^{\infty} f(\tau)h(t-\tau)d\tau\Big) \otimes_t h(t) \tag{A.47}$$

$$= \int_{\theta=-\infty}^{\infty} \Big(\int_{\tau=-\infty}^{\infty} f(\tau)h(\theta-\tau)d\tau\Big)h(t-\theta)d\theta. \tag{A.48}$$

It is important to note that in going from eqn. A.47 to eqn. A.48 the independent variable for the τ-convolution switched from t to θ. This is seen more easily if the outer convolution is performed before the inner convolution in eqn. A.47.

$$\Big(f(t) \otimes_t h(t)\Big) \otimes_t h(t) = \int_{\theta=-\infty}^{\infty} \Big(f(\theta) \otimes_\theta h(\theta)\Big)h(t-\theta)d\theta \tag{A.49}$$

$$= \int_{\theta=-\infty}^{\infty} \Big(\int_{\tau=-\infty}^{\infty} f(\tau)h(\theta-\tau)d\tau\Big)h(t-\theta)d\theta \tag{A.50}$$

Since eqn. A.48 and eqn. A.50 are the same, one can recognize that the order in

which the convolutions are converted to the integral notation does not matter.

Continuing from A.50 and exchanging the order of integration the associative property of convolutions is shown.

$$\Big(f(t) \otimes_t h(t)\Big) \otimes_t h(t) = \int_{\theta=-\infty}^{\infty} \Big(\int_{\tau=-\infty}^{\infty} f(\tau)h(\theta-\tau)d\tau\Big)h(t-\theta)d\theta \tag{A.51}$$

$$= \int_{\tau=-\infty}^{\infty} f(\tau)\Big(\int_{\theta=-\infty}^{\infty} h(\theta-\tau)h(t-\theta)d\theta\Big)d\tau \tag{A.52}$$

$$= \int_{\tau=-\infty}^{\infty} f(\tau)\Big(h(t-\tau) \otimes_t h(t)\Big)d\tau \tag{A.53}$$

$$= f(t) \otimes_t \Big(h(t) \otimes_t h(t)\Big) \tag{A.54}$$

APPENDIX B

Calculation of the Normalization Factor in Multiple-Scattering Time-Reversal Acoustics

M is a normalization factor used to scale the amplitude of the time-reversed signal to be transmitted into the multiple scattering medium. There are multiple ways of doing this [1–3]. Here a common approach is chosen. The signal is normalized so that its absolute magnitude is unity. In experiments, this can be done based on each signal that is time-reversed and retransmitted. However, as Derode *et al.* [1] argue, this value does not change substantially from one realization to the next. As such, it is possible to compute a statistical estimate based on an ensemble of realizations. It is important to determine M as it is used in computing the expectation value and variance (though it cancels out for the SNR).

The estimation begins with the received signal:

$$s(t) = W(t) \cdot (g(t) \otimes_t h(t)). \tag{B.1}$$

If one computes the envelope of $s(t)$ (based on an ensemble) and takes the maximum value of the envelope, then they have computed an estimate for M. Since $s(t)$ is a statistical quantity, the envelope can be estimated as being n standard deviations from the ensemble mean (i.e. zero). The question then becomes, how many standard deviations out does one need to go to include the maximum, without going beyond the maximum? Since the data is modeled as a normal random variable, the

more independent data points that occur around the maximum of the envelope, the more likely it is for one of the data points to be farther from the ensemble mean. For example, if there were 100 independent data points near the maximum of the envelope, then one would want to include 99% of the normal distribution (i.e. 2.5 standard deviations) and if there were 1000 independent data points near the maximum, then one would want to include 99.9% of the normal distribution (i.e. 3.3 standard deviations). Therefore, it is necessary to estimate the number of independent data points near the maximum of the envelope of $s(t)$. The time interval one must move to be part of an independent data set can be estimated as the length of the input function (t_g) plus the duration of the autocorrelation time (t_ρ). Knowing this, one can estimate the number of independent data points by dividing the length of the time-interval over which the envelope near the maximum is constant by the length of the time-interval for independent data points. Thus, if $\sigma(t)$ decays slowly and the window-function is large and $t_g + t_\rho$ is short in time (each relative to each other), then there will be many independent time intervals that may contain a maximum value in eqn. B.1.

The ensemble variance of $s(t)$ is now calculated so that the envelope can be computed.

$$\mathrm{VAR}\{s(t)\} = E\{s^2(t)\} - E^2\{s(t)\} \tag{B.2}$$

Since $h(t)$ is mean-zero, the second term will be zero. Therefore:

$$\begin{aligned} \mathrm{VAR}\{s(t)\} &= E\{s^2(t)\} \\ &= \int_{h(t)=-\infty}^{\infty} \left(W(t) \cdot \int_{\tau=-\infty}^{\infty} g(\tau) h(t-\tau)\, d\tau \right)^2 \cdot f(h(t))\, dh(t). \end{aligned} \tag{B.3}$$

Expanding the square and reordering the integrals and then using eqn. 4.17:

$$\mathrm{VAR}\{s(t)\} = W^2(t) \cdot \int_{\tau_1=-\infty}^{\infty} \int_{\tau_2=-\infty}^{\infty} g(\tau_1)g(\tau_2)\times \\ \sigma(t-\tau_1)\sigma(t-\tau_2)\rho(\tau_1-\tau_2)\; d\tau_2\; d\tau_1. \tag{B.4}$$

Recalling that $\rho(t)$ is the autocorrelation coefficient of the random arrival times $h(t)$, it is non-zero for only a short time t_ρ and on the order of the duration of the acousto-electrical impulse response (i.e. a few tens of microseconds). On the other hand, $\sigma(t)$ is approximated by the envelope of $h(t)$ and thus is a slowly varying function (i.e. a few hundred or thousand microseconds). Thus $\sigma(t)$ is approximately constant when $\rho(t) \neq 0$. Therefore $\sigma(t-\tau_2)\rho(\tau_1-\tau_2) \approx \sigma(t-\tau_1)\rho(\tau_1-\tau_2)$. Using this fact and then rewriting the integrals in traditional convolution notation:

$$\mathrm{VAR}\{s(t)\} = W^2(t) \cdot \Big[\sigma^2(t) \otimes_t \Big(g(t)\Big(g(t) \otimes_t \rho(t)\Big)\Big)\Big]. \tag{B.5}$$

Thus one can estimate M as:

$$M \approx max\left\{n \cdot \sqrt{W^2(t) \cdot \Big[\sigma^2(t) \otimes_t \Big(g(t)\Big(g(t) \otimes_t \rho(t)\Big)\Big)\Big]}\right\}, \tag{B.6}$$

where n is the number of standard deviations one must include, as discussed above.

REFERENCES

[1] A. Derode, A. Tourin, and M. Fink, "Ultrasonic pulse compression with one-bit time reversal through multiple scattering," *Journal of Applied Physics*, vol. 85, pp. 6343–6352, May 1999.

[2] J. White, G. T. Clement, and K. Hynynen, "Transcranial ultrasound focus reconstruction with phase and amplitude correction," *IEEE Transactions on Ultrasonics, Ferroelectrics, and Frequency Control*, vol. 52, pp. 1518–1522, September 2005.

[3] J.-F. Aubry, M. Pernot, F. Marquet, M. Tanter, and M. Fink, "Transcostal high-intensity-focused ultrasound: ex vivo adaptive focusing feasibility study," *Physics in Medicine and Biology*, vol. 53, pp. 2937–2951, 2008.

APPENDIX C

Calculation of the Focused Signal Variance for Multiple-Scattering Time-Reversal Acoustics

The variance of $r(t)$ is computed from:

$$\mathrm{VAR}\{r(t)\} = E\{r^2(t)\} - E^2\{r(t)\}. \tag{C.1}$$

The second term is computed from $E\{r(t)\}$ (eqn. 4.20). The first term is found by substituting in $r(t) = \left(\frac{1}{M}W(T-t)\cdot\left(g(-t)\otimes h(T-t)\right)\right)\otimes h(t)$. This is converted to integral notation using the same steps as was done for the expectation value of $r(t)$.

$$E\{r^2(t)\} \approx \frac{1}{M}E\left\{\left(\left(W(T-t)\cdot\left(g(-t)\otimes_t h(T-t)\right)\right)\otimes_t h(t)\right)^2\right\} \tag{C.2}$$

$$= \frac{1}{M}E\left\{\left(\left(W(T-t)\cdot\int_{\tau=-\infty}^{\infty} g(-\tau)h(T-(t-\tau))\,d\tau\right)\otimes_t h(t)\right)^2\right\} \tag{C.3}$$

$$= \frac{1}{M}E\left\{\left(\int_{\theta_t=-\infty}^{\infty}\left(W(T-\theta_t)\cdot\int_{\tau_\theta=-\infty}^{\infty} g(-\tau_\theta)h(T-(\theta_t-\tau_\theta))\,d\tau_\theta\right)h(t-\theta_t)\,d\theta_t\right)^2\right\} \tag{C.4}$$

The square can now be applied. Note that the two square terms should have independent variables, for instance $(g(-\tau_\theta))^2 \rightarrow g(-\tau_{\theta,1})\cdot g(-\tau_{\theta,2})$. For simplicity the τ and θ subscripts will be dropped so that $(g(-\tau_\theta))^2 \rightarrow g(-\tau_1)\cdot g(-\tau_2)$ where τ_1 and τ_2 are independent. After applying the square, writing the expectation value as

an intergral, rearranging, and converting back to the $E\{\bullet\}$ notation:

$$\begin{aligned} E\{r^2(t)\} \approx & \frac{1}{M^2} \int_{\theta_1=-\infty}^{\infty} \int_{\tau_1=-\infty}^{\infty} \int_{\theta_2=-\infty}^{\infty} \int_{\tau_2=-\infty}^{\infty} W(T-\theta_1)W(T-\theta_2)\times \\ & E\Big\{ h(T-(\theta_1-\tau_1))h(t-\theta_1)h(T-(\theta_2-\tau_2))h(t-\theta_2) \Big\}\times \\ & g(-\tau_1)g(-\tau_2)\; d\tau_2\; d\theta_2\; d\tau_1\; d\theta_1. \end{aligned} \tag{C.5}$$

This can be further simplified by noting that the expectation value of any quadruplet of jointly normal random variables (X_1, X_2, X_3, X_4) is given by [1]:

$$\begin{aligned} E\{X_1X_2X_3X_4\} = & E\{X_1X_2\}E\{X_3X_4\}+ \\ & E\{X_1X_4\}E\{X_2X_3\} + E\{X_1X_3\}E\{X_2X_4\}. \end{aligned} \tag{C.6}$$

Applying this to eqn. C.6 and recalling $E\{x(t_1)\cdot y(t_2)\} = \rho(t_1-t_2)\cdot\sigma_x(t_1)\cdot\sigma_y(t_2)$:

$$\begin{aligned} & E\{h(T-(\theta_1-\tau_1))h(t-\theta_1)h(T-(\theta_2-\tau_2))h(t-\theta_2)\} \\ & \quad = E\{h(T-(\theta_1-\tau_1))h(t-\theta_1)\}\cdot E\{h(T-(\theta_2-\tau_2))h(t-\theta_2)\} + \\ & \quad\quad E\{h(T-(\theta_1-\tau_1))h(t-\theta_2)\}\cdot E\{h(T-(\theta_2-\tau_2))h(t-\theta_1)\} + \\ & \quad\quad E\{h(T-(\theta_1-\tau_1))h(T-(\theta_2-\tau_2))\}\cdot E\{h(t-\theta_1)h(t-\theta_2)\} \end{aligned} \tag{C.7}$$

$$\begin{aligned} & \quad = \sigma(T-(\theta_1-\tau_1))\sigma(t-\theta_1)\sigma(T-(\theta_2-\tau_2))\sigma(t-\theta_2)\times \\ & \quad\quad \Big\{ \rho(T-(t-\tau_1))\rho(T-(t-\tau_2)) + \\ & \quad\quad \rho(T-(\theta_1-\tau_1)-(t-\theta_2))\rho(T-(\theta_2-\tau_2)-(t-\theta_1)) + \\ & \quad\quad \rho((\theta_2-\tau_2)-(\theta_1-\tau_1))\rho(\theta_2-\theta_1) \Big\}. \end{aligned} \tag{C.8}$$

The variance can now be written as three additive terms:

$$\frac{1}{M^2}\int_{\theta_1=-\infty}^{\infty}\int_{\tau_1=-\infty}^{\infty}\int_{\theta_2=-\infty}^{\infty}\int_{\tau_2=-\infty}^{\infty} W(T-\theta_1)W(T-\theta_2)\times$$
$$\sigma(T-(\theta_1-\tau_1))\sigma(t-\theta_1)\sigma(T-(\theta_2-\tau_2))\sigma(t-\theta_2)\times$$
$$\rho(T-(t-\tau_1))\rho(T-(t-\tau_2))\times$$
$$g(-\tau_1)g(-\tau_2)\ d\tau_2\ d\theta_2\ d\tau_1\ d\theta_1 \tag{C.9a}$$

$$\frac{1}{M^2}\int_{\theta_1=-\infty}^{\infty}\int_{\tau_1=-\infty}^{\infty}\int_{\theta_2=-\infty}^{\infty}\int_{\tau_2=-\infty}^{\infty} W(T-\theta_1)W(T-\theta_2)\times$$
$$\sigma(T-(\theta_1-\tau_1))\sigma(t-\theta_1)\sigma(T-(\theta_2-\tau_2))\sigma(t-\theta_2)\times$$
$$\rho(T-(\theta_1-\tau_1)-(t-\theta_2))\rho(T-(\theta_2-\tau_2)-(t-\theta_1))\times$$
$$g(-\tau_1)g(-\tau_2)\ d\tau_2\ d\theta_2\ d\tau_1\ d\theta_1 \tag{C.9b}$$

$$\frac{1}{M^2}\int_{\theta_1=-\infty}^{\infty}\int_{\tau_1=-\infty}^{\infty}\int_{\theta_2=-\infty}^{\infty}\int_{\tau_2=-\infty}^{\infty} W(T-\theta_1)W(T-\theta_2)\times$$
$$\sigma(T-(\theta_1-\tau_1))\sigma(t-\theta_1)\sigma(T-(\theta_2-\tau_2))\sigma(t-\theta_2)\times$$
$$\rho((\theta_2-\tau_2)-(\theta_1-\tau_1))\rho(\theta_2-\theta_1)\times$$
$$g(-\tau_1)g(-\tau_2)\ d\tau_2\ d\theta_2\ d\tau_1\ d\theta_1. \tag{C.9c}$$

It will be seen that eqn. C.9a is equal to $E^2\{r(t)\}$, eqn. C.9b will be called the coherent variance term, and eqn. C.9c will be called the incoherent variance term.

C.1 Term 1

Starting from eqn. C.9a and noting its similarity to $E\{r(t)\}$,

$$\text{Eqn. C.9a} = \left[\frac{1}{M} \int_{\theta=-\infty}^{\infty} \int_{\tau=-\infty}^{\infty} W(T-\theta) g(-\tau) \sigma(T-(\theta-\tau)) \times \right.$$
$$\left. \sigma(t-\theta)\rho(T-(t-\tau))\ d\tau d\theta \right]^2 \tag{C.10}$$

$$= E^2\{r(t)\}. \tag{C.11}$$

This term then cancels with the first term in eqn. C.1.

C.2 Term 2

The goal will be to rewrite eqn. C.9b in traditional convolution notation (i.e. $a(t) \otimes b(t)$), which is both easier to compute and interpret.

$$\text{Eqn. C.9b} = \frac{1}{M^2} \int_{\theta_1=-\infty}^{\infty} \int_{\theta_2=-\infty}^{\infty} W(T-\theta_1) W(T-\theta_2) \sigma(t-\theta_1) \sigma(t-\theta_2) \times$$
$$\left[\int_{\tau_1=-\infty}^{\infty} g(-\tau_1) \sigma(T-(\theta_1-\tau_1)) \rho(T-(\theta_1-\tau_1)-(t-\theta_2))\ d\tau_1 \right] \times$$
$$\left[\int_{\tau_2=-\infty}^{\infty} g(-\tau_2) \sigma(T-(\theta_2-\tau_2)) \rho(T-(\theta_2-\tau_2)-(t-\theta_1))\ d\tau_2 \right]\ d\theta_2\ d\theta_1 \tag{C.12}$$

$$= \frac{1}{M^2} \int_{\theta_1=-\infty}^{\infty} \int_{\theta_2=-\infty}^{\infty} W(T-\theta_1) W(T-\theta_2) \sigma(t-\theta_1) \sigma(t-\theta_2) \times$$
$$\left[g(-\theta_1) \otimes_{\theta_1} \Big(\sigma(T-\theta_1) \rho(T-\theta_1-(t-\theta_2)) \Big) \right] \times$$
$$\left[g(-\theta_2) \otimes_{\theta_2} \Big(\sigma(T-\theta_2) \rho(T-\theta_2-(t-\theta_1)) \Big) \right]\ d\theta_2\ d\theta_1. \tag{C.13}$$

Recalling that $\rho(t)$ is the autocorrelation coefficient of the random arrival times $h(t)$, it is non-zero for only a short time t_ρ and on the order of the duration of the acousto-electrical impulse response (i.e. a few tens of microseconds). On the other hand, $\sigma(t)$ is approximated by the envelope of $h(t)$ and thus is a slowly varying

function (i.e. a few hundreds or thousands of microseconds). Thus over the short time that $\rho(t)$ is non-zero, $\sigma(t)$ is approximately constant. Applying this to the terms in the square brackets above, $\sigma(T-\theta_i)\rho((T-\theta_i)-(t-\theta_j)) \approx \sigma(t-\theta_j)\rho((T-\theta_i)-(t-\theta_j))$. Then $\sigma(t-\theta_j)$ can be pulled out of the θ_i integral. Thus the second term of the variance simplifies to:

$$\frac{1}{M^2}\int_{\theta_1=-\infty}^{\infty}\int_{\theta_2=-\infty}^{\infty} W(T-\theta_1)W(T-\theta_2)\sigma^2(t-\theta_1)\sigma^2(t-\theta_2)\times \left[g(-\theta_1)\otimes_{\theta_1}\rho(T-\theta_1-(t-\theta_2))\right]\times \left[g(-\theta_2)\otimes_{\theta_2}\rho(T-\theta_2-(t-\theta_1))\right]\,d\theta_2\,d\theta_1. \tag{C.14}$$

Unfortunately, the θ-integrals cannot be written in convolution notation due to the mixing of the θ_1's and θ_2's in both ρ's.

To check equation C.14, it can be shown that it simplifies to the corresponding result of Derode *et al.* (term 2 of eqn. A7 in [2]) by letting the window extend to positive and negative infinity (i.e $W(t) = 1\ \forall\ t$), setting $T = 0$, and letting $g(t) \to \delta(t)$.

$$\frac{1}{M^2}\int_{\theta_1=-\infty}^{\infty}\int_{\theta_2=-\infty}^{\infty} W(T-\theta_1)W(T-\theta_2)\sigma^2(t-\theta_1)\sigma^2(t-\theta_2)\times \left[g(-\theta_1)\otimes_{\theta_1}\rho(T-\theta_1-(t-\theta_2))\right]\times \left[g(-\theta_2)\otimes_{\theta_2}\rho(T-\theta_2-(t-\theta_1))\right]\,d\theta_2\,d\theta_1. \tag{C.14$'$}$$

$$= \frac{1}{M^2}\int_{\theta_1=-\infty}^{\infty}\int_{\theta_2=-\infty}^{\infty} \sigma^2(t-\theta_1)\sigma^2(t-\theta_2)\times \left[\delta(-\theta_1)\otimes_{\theta_1}\rho(\theta_2-\theta_1-t)\right]\left[\delta(-\theta_2)\otimes_{\theta_2}\rho(\theta_1-\theta_2-t)\right]\,d\theta_2\,d\theta_1 \tag{C.15}$$

$$= \frac{1}{M^2}\int_{\theta_1=-\infty}^{\infty}\int_{\theta_2=-\infty}^{\infty} \sigma^2(t-\theta_1)\sigma^2(t-\theta_2)\rho(\theta_2-\theta_1-t)\rho(\theta_1-\theta_2-t)\,d\theta_2\,d\theta_1 \tag{C.16}$$

By noting that $\rho(t) = \rho(-t)$, recalling that $\rho(t)$ is non-zero for $|t| < t_\rho$

during which $\sigma(t)$ is constant, and performing the change of variable, $\theta_2 = \theta$ and $\tau = \theta_1 - \theta_2 = \theta_1 - \theta$, eqn. C.16 can be further simplified to match term 2 of eqn. A7 in Derode *et al.* [2].

$$\frac{1}{M^2}\int_{\theta_1=-\infty}^{\infty}\int_{\theta_2=-\infty}^{\infty}\sigma^2(t-\theta_1)\sigma^2(t-\theta_2)\rho(\theta_2-\theta_1-t)\rho(\theta_1-\theta_2-t)\;d\theta_2\;d\theta_1 \quad \text{(C.16}') $$

$$= \frac{1}{M^2}\int_{\theta=-\infty}^{\infty}\int_{\tau=-\infty}^{\infty}\sigma^2(t-\tau-\theta)\sigma^2(t-\theta)\rho(t-\tau)\rho(t+\tau)\;d\tau d\theta \quad \text{(C.17)}$$

$$= \frac{1}{M^2}\int_{\theta=-\infty}^{\infty}\sigma^4(\theta)\;d\theta\;\int_{\tau=-\infty}^{\infty}\rho(t-\tau)\rho(t+\tau)\;d\tau \quad \text{(C.18)}$$

C.3 Term 3

For the final term of the variance, the goal is to again write the result in convolution notation. This is accomplished by reordering the integrals and then writing them in traditional convolution notation, which is most easily done by making τ_2 the innermost integral then working out to the τ_1-, θ_2-, and finally θ_1-integral. These are then converted to traditional convolution notation beginning with the τ_2-integral

and working outwards. The result is:

$$
\begin{aligned}
&\text{Eqn. C.9c} = \\
&\frac{1}{M^2}\int_{\theta_1=-\infty}^{\infty}\int_{\tau_1=-\infty}^{\infty}\int_{\theta_2=-\infty}^{\infty}\int_{\tau_2=-\infty}^{\infty} W(T-\theta_1)W(T-\theta_2)\times \\
&\qquad g(-\tau_1)g(-\tau_2)\sigma(T-(\theta_1-\tau_1))\sigma(t-\theta_1)\sigma(T-(\theta_2-\tau_2))\sigma(t-\theta_2)\times \\
&\qquad\quad \rho((\theta_2-\tau_2)-(\theta_1-\tau_1))\rho(\theta_2-\theta_1)\; d\tau_2\; d\theta_2\; d\tau_1\; d\theta_1
\end{aligned}
\tag{C.19}
$$

$$
\begin{aligned}
&= \frac{1}{M^2}\int_{\theta_1=-\infty}^{\infty} W(T-\theta_1)\sigma(t-\theta_1)\Bigg[\int_{\theta_2=-\infty}^{\infty} W(T-\theta_2)\sigma(t-\theta_2)\rho(\theta_2-\theta_1)\times \\
&\quad \Bigg[\int_{\tau_1=-\infty}^{\infty} g(-\tau_1)\sigma(T-(\theta_1-\tau_1))\times \\
&\quad \Big[\int_{\tau_2=-\infty}^{\infty} g(-\tau_2)\sigma(T-(\theta_2-\tau_2))\rho((\theta_2-\tau_2)-(\theta_1-\tau_1))\; d\tau_2\Big]\; d\tau_1\Bigg]\; d\theta_2\Bigg]\; d\theta_1
\end{aligned}
\tag{C.20}
$$

$$
\begin{aligned}
&= \frac{1}{M^2}\int_{\theta_1=-\infty}^{\infty} W(T-\theta_1)\sigma(t-\theta_1)\Bigg[\int_{\theta_2=-\infty}^{\infty} W(T-\theta_2)\sigma(t-\theta_2)\rho(\theta_2-\theta_1)\times \\
&\quad \Bigg[\int_{\tau_1=-\infty}^{\infty} g(-\tau_1)\sigma(T-(\theta_1-\tau_1))\times \\
&\quad \Big[g(-\theta_2)\otimes_{\theta_2}\Big(\sigma(T-\theta_2)\rho(\theta_2-(\theta_1-\tau_1))\Big)\Big]\; d\tau_1\Bigg]\; d\theta_2\Bigg]\; d\theta_1
\end{aligned}
\tag{C.21}
$$

$$
\begin{aligned}
&= \frac{1}{M^2}\int_{\theta_1=-\infty}^{\infty} W(T-\theta_1)\sigma(t-\theta_1)\Bigg[\int_{\theta_2=-\infty}^{\infty} W(T-\theta_2)\sigma(t-\theta_2)\rho(\theta_2-\theta_1)\times \\
&\quad \Big[g(-\theta_1)\otimes_{\theta_1}\Big\{\sigma(T-\theta_1)\Big[g(-\theta_2)\otimes_{\theta_2}\Big(\sigma(T-\theta_2)\rho(\theta_2-\theta_1)\Big)\Big]\Big\}\Big]\; d\theta_2\Bigg]d\theta_1
\end{aligned}
\tag{C.22}
$$

$$
\begin{aligned}
&= \frac{1}{M^2}\int_{\theta_1=-\infty}^{\infty} W(T-\theta_1)\sigma(t-\theta_1)\Bigg[\sigma(t)\otimes_t\Big\{W(T-t)\rho(t-\theta_1)\times \\
&\quad \Big[g(-\theta_1)\otimes_{\theta_1}\Big\{\sigma(T-\theta_1)\Big[g(-t)\otimes_t\Big(\sigma(T-t)\rho(t-\theta_1)\Big)\Big]\Big\}\Big]\Big\}\Bigg]\; d\theta_1.
\end{aligned}
\tag{C.23}
$$

The final θ_1-integral cannot be converted to convolution notation due to the presence of both θ_1 and $t-\theta_1$ terms in the convolutions. However, again applying the fact that $\rho(t)$ has a small interval over which it is non-zero, the innermost convolution

simplifies via: $\sigma(T-t)\rho(t-\theta_1) \approx \sigma(T-\theta_1)\rho(t-\theta_1)$. Then $\sigma(T-\theta_1)$ can be pulled out of the inner-most convolution, which yields the final form of the third term of the variance as:

$$\frac{1}{M^2}\int_{\theta_1=-\infty}^{\infty} W(T-\theta_1)\sigma(t-\theta_1)\Bigg[\sigma(t)\otimes_t\Bigg\{W(T-t)\rho(t-\theta_1)\times \Bigg[g(-\theta_1)\otimes_{\theta_1}\Big\{\sigma^2(T-\theta_1)\Big[g(-t)\otimes_t\rho(t-\theta_1)\Big]\Big\}\Bigg]\Bigg\}\Bigg]\,d\theta_1. \tag{C.24}$$

As with the second term, this result can be simplified to the corresponding result of Derode *et al.* [2] (term 1 of eqn. A7) by letting the window extend to positive and negative infinity (i.e $W(t) = 1\ \forall\ t$), setting $T = 0$, and letting $g(t) \to \delta(t)$.

$$\frac{1}{M^2}\int_{\theta_1=-\infty}^{\infty} W(T-\theta_1)\sigma(t-\theta_1)\Bigg[\sigma(t)\otimes_t\Bigg\{W(T-t)\rho(t-\theta_1)\times \Bigg[g(-\theta_1)\otimes_{\theta_1}\Big\{\sigma^2(T-\theta_1)\Big[g(-t)\otimes_t\rho(t-\theta_1)\Big]\Big\}\Bigg]\Bigg\}\Bigg]\,d\theta_1 \tag{C.24$'$}$$

$$= \frac{1}{M^2}\int_{\theta_1=-\infty}^{\infty} \sigma(t-\theta_1)\Bigg[\sigma(t)\otimes_t\Bigg\{\rho(t-\theta_1)\times \Bigg[\delta(-\theta_1)\otimes_{\theta_1}\Big\{\sigma^2(-\theta_1)\Big[\delta(-t)\otimes_t\rho(t-\theta_1)\Big]\Big\}\Bigg]\Bigg\}\Bigg]\,d\theta_1 \tag{C.25}$$

$$= \frac{1}{M^2}\int_{\theta_1=-\infty}^{\infty} \sigma(t-\theta_1)\Bigg[\sigma(t)\otimes_t\Big\{\rho(t-\theta_1)\sigma^2(-\theta_1)\rho(t-\theta_1)\Big\}\Bigg]\,d\theta_1 \tag{C.26}$$

$$= \frac{1}{M^2}\int_{\theta_1=-\infty}^{\infty} \sigma(t-\theta_1)\Bigg[\int_{\theta_2=-\infty}^{\infty}\sigma(t-\theta_2)\rho(\theta_2-\theta_1)\sigma^2(-\theta_1)\rho(\theta_2-\theta_1)\,d\theta_2\Bigg]\,d\theta_1 \tag{C.27}$$

$$= \frac{1}{M^2}\int_{\theta_1=-\infty}^{\infty}\int_{\theta_2=-\infty}^{\infty} \sigma^2(-\theta_1)\sigma(t-\theta_1)\sigma(t-\theta_2)\rho^2(\theta_2-\theta_1)\,d\theta_2\,d\theta_1 \tag{C.28}$$

Using the change of variable $\theta_1 = \theta$ and $\theta_2 - \theta_1 = \theta_2 - \theta = \tau$ and recalling that $\rho(t)$ is non-zero for $|t| < t_\rho$, the above result simplifies to term 1 of eqn. A7 in Derode *et*

al. [2].

$$\frac{1}{M^2}\int_{\theta_1=-\infty}^{\infty}\int_{\theta_2=-\infty}^{\infty}\sigma^2(-\theta_1)\sigma(t-\theta_1)\sigma(t-\theta_2)\rho^2(\theta_2-\theta_1)\;d\theta_2\;d\theta_1 \tag{C.28$'$}$$

$$=\frac{1}{M^2}\int_{\theta=-\infty}^{\infty}\int_{\tau=-\infty}^{\infty}\sigma^2(-\theta)\sigma(t-\theta)\sigma(t-\tau-\theta)\rho^2(\tau)\;d\tau d\theta \tag{C.29}$$

$$=\frac{1}{M^2}\int_{\theta=-\infty}^{\infty}\sigma^2(-\theta)\sigma^2(t-\theta)\;d\theta\int_{\tau=-\infty}^{\infty}\rho^2(\tau)\;d\tau \tag{C.30}$$

$$=\frac{1}{M^2}\int_{\theta=-\infty}^{\infty}\sigma^2(\theta)\sigma^2(t+\theta)\;d\theta\int_{\tau=-\infty}^{\infty}\rho^2(\tau)\;d\tau \tag{C.31}$$

C.3.1 Total Variance

Inserting eqns. C.11, C.14, C.24 as $E^2\{r(t)\}$ in eqn. C.1, the final form for the variance is:

$$\begin{aligned}
\mathrm{VAR}\{r(t)\} =& E\{r^2(t)\} - E^2\{r(t)\} \\
=&\left(\frac{1}{M^2}\int_{\theta_1=-\infty}^{\infty}\int_{\theta_2=-\infty}^{\infty}W(T-\theta_1)W(T-\theta_2)\sigma^2(t-\theta_1)\sigma^2(t-\theta_2)\times\right. \\
&\qquad\left[g(-\theta_1)\otimes_{\theta_1}\rho(T-\theta_1-(t-\theta_2))\right]\times \\
&\qquad\left.\left[g(-\theta_2)\otimes_{\theta_2}\rho(T-\theta_2-(t-\theta_1))\right]\;d\theta_2\;d\theta_1\right)+ \\
&\left(\frac{1}{M^2}\int_{\theta_1=-\infty}^{\infty}W(T-\theta_1)\sigma(t-\theta_1)\left[\sigma(t)\otimes_t\left\{W(T-t)\rho(t-\theta_1)\times\right.\right.\right. \\
&\qquad\left.\left.\left.\left[g(-\theta_1)\otimes_{\theta_1}\left\{\sigma^2(T-\theta_1)\left[g(-t)\otimes_t\rho(t-\theta_1)\right]\right\}\right]\right\}\right]\;d\theta_1\Bigg).
\end{aligned} \tag{C.32}$$

REFERENCES

[1] A. Papoulis, *Probability, Random Variables, and Stochastic Processes*. McGraw-Hill Series in Systems Science, McGraw-Hill, Inc., 1984.

[2] A. Derode, A. Tourin, and M. Fink, "Ultrasonic pulse compression with one-bit time reversal through multiple scattering," *Journal of Applied Physics*, vol. 85, pp. 6343–6352, May 1999.

APPENDIX D

Calculation of Simplified Focused Signal Expectation Value for Multiple-Scattering Time-Reversal Acoustics

Applying the assumptions outlined in equation 4.26 to the expectation value $\mathrm{E}\{r(t)\}$ (eqn. 4.20) and beginning with the innermost portion:

$$\Big(W(T-t)\cdot\sigma(T-t)\Big)\otimes\sigma(t) = \int_{-\infty}^{\infty} W(T-\tau)\sigma(T-\tau)\sigma(t-\tau)d\tau \tag{D.1}$$

$$= \int_{T-t_{off}}^{T-t_{on}} u(T-\tau)e^{-\alpha(T-\tau)}u(t-\tau)e^{-\alpha(t-\tau)}d\tau \tag{D.2}$$

$$= \frac{e^{-\alpha t}e^{\alpha T}}{2\alpha}e^{-2\alpha t_{on}}(1-e^{-2\alpha\Delta t}), \tag{D.3}$$

where$\Delta\ t = t_{off} - t_{on}$, is the window width. Equation D.3 is then multiplied by $\rho(T-t)$, which is non-zero only for $t \approx T$. Additionally, since eqn. D.3 is a slowly changing function (on the order of $\frac{1}{\alpha}$), the following approximation can be made:

$$\rho(T-t)\bigg(\Big(W(T-t)\cdot\sigma(T-t)\Big)\otimes\sigma(t)\bigg) \approx \delta(T-t)\bigg(\frac{e^{-\alpha t}e^{\alpha T}}{2\alpha}e^{-2\alpha t_{on}}(1-e^{-2\alpha\Delta t})\bigg) \tag{D.4}$$

$$= \frac{1}{2\alpha}e^{-2\alpha t_{on}}(1-e^{-2\alpha\Delta t})\delta(T-t). \tag{D.5}$$

Equation D.5 is convolved with $g(-t)$ and divided by M to give:

$$E\{r(t)\} \approx \frac{1}{2\alpha M} e^{-2\alpha t_{on}} (1 - e^{-2\alpha \Delta t}) \cdot g(T - t). \tag{D.6}$$

APPENDIX E

Calculation of Simplified Focused Signal Coherent Variance for Multiple-Scattering Time-Reversal Acoustics

The derivations of eqns. 4.28 and 4.29 are now given. They begin by looking at the coherent variance term (eqn. C.14) and recalling the assumptions in eqn. 4.26. In particular, since $g(t) \otimes \rho(t) \approx g(t) \otimes \delta(t) = g(t)$:

$$\begin{aligned}
\mathrm{VAR}_{coherent} = \frac{1}{M^2} \int_{\theta_1=-\infty}^{\infty} \int_{\theta_2=-\infty}^{\infty} & W(T-\theta_1)W(T-\theta_2)\sigma^2(t-\theta_1)\sigma^2(t-\theta_2) \times \\
& \Big[g(-\theta_1) \otimes_{\theta_1} \rho(T-\theta_1-(t-\theta_2)) \Big] \times \\
& \Big[g(-\theta_2) \otimes_{\theta_2} \rho(T-\theta_2-(t-\theta_1)) \Big] \, d\theta_2 \, d\theta_1 \qquad \text{(E.1)} \\
\approx \frac{1}{M^2} \int_{\theta_1=-\infty}^{\infty} \int_{\theta_2=-\infty}^{\infty} & W(T-\theta_1)W(T-\theta_2)\sigma^2(t-\theta_1)\sigma^2(t-\theta_2) \times \\
& g(T-(t-\theta_2)-\theta_1) g(T-(t-\theta_1)-\theta_2) \, d\theta_2 \, d\theta_1. \qquad \text{(E.2)}
\end{aligned}$$

Making the substitutions $\theta_1 - \theta_2 = \tau$, $\theta_2 = \theta$, and eqn. 4.26a ($\sigma(t) = u(t)e^{-\alpha t}$).

$$\begin{aligned}
\mathrm{VAR}_{coherent} \approx & \frac{1}{M^2} \int_{\tau=-\infty}^{\infty} g(T-(t+\tau)) g(T-(t-\tau)) \times \\
& \int_{\theta=-\infty}^{\infty} W(T-(\tau+\theta))W(T-\theta) \times \\
& u((t-(\tau+\theta))e^{-2\alpha(t-(\tau+\theta))} u(t-\theta)e^{-2\alpha(t-\theta)} \, d\theta d\tau \qquad \text{(E.3)}
\end{aligned}$$

The window and Heaviside functions can now be used to place limits on the range of the θ-integral.

$$W(T-\theta) \longrightarrow T - t_{off} \leq \theta \leq T - t_{on} \tag{E.4a}$$

$$W(T-\tau-\theta) \longrightarrow T - \tau - t_{off} \leq \theta \leq T - \tau - t_{on} \tag{E.4b}$$

$$u(t-\tau-\theta) \longrightarrow \theta \leq t - \tau \tag{E.4c}$$

$$u(t-\theta) \longrightarrow \theta \leq t \tag{E.4d}$$

The above limitations divide into two regimes. When $\tau \leq 0$, then the lower limit of the θ-integral is set by $T - \tau - t_{off}$ and the upper limit set by the smaller of $T - t_{on}$ and t. When $\tau \geq 0$, then the lower limit of the θ-integral is set by $T - t_{off}$ and the upper limit set by the smaller of $T - \tau - t_{on}$ and $t - \tau$. Applying this and defining

$G(t,\tau) = g(T-(t+\tau))g(T-(t-\tau))$:

$$\begin{aligned}\mathrm{VAR}_{coherent} \approx \frac{1}{M^2}\int_{\tau=-\infty}^{0} G(t,\tau)\int_{\theta=-T-\tau-t_{off}}^{\min\{T-t_{on},t\}} e^{-2\alpha(t-(\tau+\theta))}e^{-2\alpha(t-\theta)}\,d\theta d\tau \;+ \\ \frac{1}{M^2}\int_{\tau=0}^{\infty} G(t,\tau)\int_{\theta=-T-t_{off}}^{\min\{T-\tau-t_{on},t-\tau\}} e^{-2\alpha(t-(\tau+\theta))}e^{-2\alpha(t-\theta)}\,d\theta d\tau\end{aligned} \tag{E.5}$$

$$\begin{aligned}=&\frac{1}{M^2}\int_{\tau=-\infty}^{0} G(t,\tau)e^{-2\alpha(2t-\tau)}\frac{1}{4\alpha}e^{4\alpha\theta}\Big|_{\theta=-T-\tau-t_{off}}^{\min\{T-t_{on},t\}}\,d\tau \;+ \\ &\frac{1}{M^2}\int_{\tau=0}^{\infty} G(t,\tau)e^{-2\alpha(2t-\tau)}\frac{1}{4\alpha}e^{4\alpha\theta}\Big|_{\theta=-T-t_{off}}^{\min\{T-\tau-t_{on},t-\tau\}}\,d\tau\end{aligned} \tag{E.6}$$

$$=\frac{1}{M^2}\begin{cases}\int_{-\infty}^{0} G(t,\tau)e^{-2\alpha(2t-\tau)}\frac{1}{4\alpha}e^{4\alpha\theta}\Big|_{\theta=-T-\tau-t_{off}}^{t}\,d\tau \;+ & \\ \quad\int_{0}^{\infty} G(t,\tau)e^{-2\alpha(2t-\tau)}\frac{1}{4\alpha}e^{4\alpha\theta}\Big|_{\theta=-T-t_{off}}^{t-\tau}\,d\tau & \text{if } t < T-t_{on}, \\ \int_{-\infty}^{0} G(t,\tau)e^{-2\alpha(2t-\tau)}\frac{1}{4\alpha}e^{4\alpha\theta}\Big|_{\theta=-T-\tau-t_{off}}^{T-t_{on}}\,d\tau \;+ & \\ \quad\int_{0}^{\infty} G(t,\tau)e^{-2\alpha(2t-\tau)}\frac{1}{4\alpha}e^{4\alpha\theta}\Big|_{\theta=-T-t_{off}}^{T-\tau-t_{on}}\,d\tau & \text{if } t \geq T-t_{on}\end{cases} \tag{E.7}$$

$$=\frac{e^{-4\alpha t}}{4\alpha M^2}\begin{cases}\int_{-\infty}^{0} G(t,\tau)e^{2\alpha\tau}(e^{4\alpha t}-e^{4\alpha(T-\tau-t_{off})})\,d\tau \;+ & \\ \quad\int_{0}^{\infty} G(t,\tau)e^{2\alpha\tau}(e^{4\alpha(t-\tau)}-e^{4\alpha(T-t_{off})})\,d\tau & \text{if } t < T-t_{on}, \\ \int_{-\infty}^{0} G(t,\tau)e^{2\alpha\tau}(e^{4\alpha(T-t_{on})}-e^{4\alpha(T-\tau-t_{off})})\,d\tau \;+ & \\ \quad\int_{0}^{\infty} G(t,\tau)e^{2\alpha\tau}(e^{4\alpha(T-\tau-t_{on})}-e^{4\alpha(T-t_{off})})\,d\tau & \text{if } t \geq T-t_{on}.\end{cases} \tag{E.8}$$

Note that the input signal is finite. If the signal duration is $t \in [0, t_g]$, then $g(T-(t+\tau))g(T-(t-\tau))$ is non-zero only when $0 \leq T-(t+\tau) \leq t_g$ and $0 \leq T-(t-\tau) \leq t_g$. Rewriting and combining these inequalities yields $-t_g/2 \leq \tau \leq t_g/2$ and $T-t_g \leq t \leq T$. The first can be applied to the limits of the τ integral. Doing so, and making the assumption that $\frac{1}{\alpha} \gg t_g$ so that $e^{\alpha\tau} \approx 1$ in the

integrals:

$$\mathrm{VAR}_{coherent} \approx \frac{e^{-4\alpha t}}{4\alpha M^2} \begin{cases} (e^{4\alpha t} - e^{4\alpha(T-t_{off})}) \displaystyle\int_{-t_g/2}^{0} G(t,\tau)\, d\tau + & \\ \quad (e^{4\alpha t} - e^{4\alpha(T-t_{off})}) \displaystyle\int_{0}^{t_g/2} G(t,\tau)\, d\tau & \text{if } t \le T - t_{on} \\ (e^{4\alpha(T-t_{on})} - e^{4\alpha(T-t_{off})}) \displaystyle\int_{-t_g/2}^{0} G(t,\tau)\, d\tau + & \\ \quad (e^{4\alpha(T-t_{on})} - e^{4\alpha(T-t_{off})}) \displaystyle\int_{0}^{t_g/2} G(t,\tau)\, d\tau & \text{if } T - t_{on} \le t. \end{cases} \tag{E.9}$$

Defining $\kappa_1 = \displaystyle\int_{-t_g/2}^{t_g/2} G(t,\tau)\, d\tau$ and simplifying the exponential terms yields:

$$\mathrm{VAR}_{coherent} \approx \frac{\kappa_1}{4\alpha M^2} \begin{cases} e^{4\alpha(T-t)} e^{-4\alpha t_{on}} (e^{-4\alpha(T-t_{on}-t)} - e^{-4\alpha\Delta t}) & \text{if } t \le T - t_{on} \\ e^{4\alpha(T-t)} e^{-4\alpha t_{on}} (1 - e^{-4\alpha\Delta t}) & \text{if } T - t_{on} \le t. \end{cases} \tag{E.10}$$

If $\frac{1}{\alpha} \gg t_g$ is weakly violated so that only $\frac{1}{\alpha} > t_g$ holds, i.e. for a moderatley long input function, the impact would be that κ_1 would also have an $e^{\alpha\tau}$ in it, providing a modulation to the value. The modulation would change the specific shape of the result, but not the basic trends it follows as parameters are changed. Thus these can be used to determine the quantitative value of the coherent variance for short input function ($t_g \ll \tau_\sigma$) and the qualitative trends for moderately long pulses.

Now $T - t_g \le t \le T$ is applied to the intervals of the piecewise function. If $t_g > t_{on}$:

$$\mathrm{VAR}_{coherent} \approx \frac{\kappa_1}{4\alpha M^2} \begin{cases} 0 & \text{if } t < T - t_g \text{ or } T < t \\ e^{4\alpha(T-t)} e^{-4\alpha t_{on}} (e^{-4\alpha(T-t_{on}-t)} - e^{-4\alpha\Delta t}) & \text{if } T - t_g \le t \le T - t_{on} \\ e^{4\alpha(T-t)} e^{-4\alpha t_{on}} (1 - e^{-4\alpha\Delta t}) & \text{if } T - t_{on} \le t < T. \end{cases} \tag{E.11}$$

If the duration of the input function is less than window turn on time ($t_g \leq t_{on}$), then:

$$\mathrm{VAR}_{coherent} \approx \frac{\kappa_1}{4\alpha M^2} \begin{cases} 0 & \text{if } t < T - t_g \text{ or } T < t \\ e^{4\alpha(T-t)} e^{-4\alpha t_{on}} (1 - e^{-4\alpha \Delta t}) & \text{if } T - t_g \leq t < T. \end{cases} \tag{E.12}$$

APPENDIX F

Calculation of Simplified Focused Signal Incoherent Variance for Multiple-Scattering Time-Reversal Acoustics

The incoherent variance term (eqn. C.24) will now be studied under the aforementioned assumptions (eqn. 4.26). First, it is assumed that $g(t) \otimes \rho(t) \approx g(t)$.

$$\begin{aligned}
\mathrm{VAR}_{incoherent} = \frac{1}{M^2} \int_{\theta_1=-\infty}^{\infty} W(T-\theta_1)\sigma(t-\theta_1) \Bigg[\sigma(t) \otimes_t \Big\{ W(T-t)\rho(t-\theta_1) \times \\
\Big[g(-\theta_1) \otimes_{\theta_1} \Big\{ \sigma^2(T-\theta_1) \Big[g(-t) \otimes_t \rho(t-\theta_1) \Big] \Big\} \Big] \Big\} \Bigg] \, d\theta_1 \qquad \text{(F.1)} \\
\approx \frac{1}{M^2} \int_{\theta_1=-\infty}^{\infty} W(T-\theta_1)\sigma(t-\theta_1) \Bigg[\sigma(t) \otimes_t \Big\{ W(T-t)\rho(t-\theta_1) \times \\
\Big[g(-\theta_1) \otimes_{\theta_1} \Big\{ \sigma^2(T-\theta_1) g(-t+\theta_1) \Big\} \Big] \Big\} \Bigg] \, d\theta_1 \qquad \text{(F.2)} \\
\approx \frac{1}{M^2} \int_{\theta_1=-\infty}^{\infty} W(T-\theta_1)\sigma(t-\theta_1) \Bigg[\sigma(t) \otimes_t \Big\{ W(T-t)\rho(t-\theta_1) \times \\
\Big[g(-\theta_1) \otimes_{\theta_1} \Big\{ u(T-\theta_1) e^{-2\alpha T} e^{2\alpha\theta_1} g(-t+\theta_1) \Big\} \Big] \Big\} \Bigg] \, d\theta_1 \qquad \text{(F.3)}
\end{aligned}$$

For the inner portion of the above equation (assuming $e^{-\alpha t}$ is approximately constant over the duration of $g(t)$):

$$g(-\theta_1) \otimes_{\theta_1} (u(T-\theta_1) e^{2\alpha\theta_1} g(-t+\theta_1)) \approx e^{2\alpha\theta_1} \Big(g(-\theta_1) \otimes_{\theta_1} (u(T-\theta_1) g(-t+\theta_1)) \Big). \qquad \text{(F.4)}$$

When $e^{-\alpha t}$ is not approximately constant over t_g, then one must return to the equations of section 4.2. Looking at the convolution:

$$(g(-\theta_1) \otimes_{\theta_1} (u(T-\theta_1)g(-t+\theta_1)) = \int_{-\infty}^{\infty} u(T-\tau)g(\tau-t)g(\theta_1+\tau)d\tau. \qquad \text{(F.5)}$$

Note that $u(T-\tau)$ serves to limit the range of integration to $\tau < T$. Also note that $g(\theta_1+\tau)$ limits τ to $-\theta_1 \leq \tau \leq t_g - \theta_1$. Additionally, note that the outermost portion of the θ_1-integral for the incoherent term of the variance contains the term $W(T-\theta_1)$, which limits the non-zero range of θ_1 to $T-t_{off} \leq \theta_1 \leq T-t_{on}$. Applying this to the limits of τ obtained from $g(\theta_1+t)$, yields $t_{on} - T \leq \tau \leq t_g + t_{off} - T$. As long as $t_g + t_{off} - T < T$, then $g(\theta_1+T)$ limits τ more severely than $u(T-\tau)$, in which case $u(T-\tau)$ is superfluous. First, note that the largest t_{off} can be is T. Assuming this worst case, then it is required that the duration of $g(t)$ to be less than T for $u(T-\tau)$ to be superfluous. Making this reasonable restriction:

$$g(-\theta_1) \otimes_{\theta_1} (u(T-\theta_1)e^{2\alpha\theta_1}g(-t+\theta_1)) \approx e^{2\alpha\theta_1}\Big(g(-\theta_1) \otimes_{\theta_1} g(-t+\theta_1)\Big). \qquad \text{(F.6)}$$

Thus:

$$\begin{aligned} W(T-t)\rho(t-\theta_1)\cdot e^{-2\alpha T}\Big(g(-\theta_1) \otimes_{\theta_1} (u(T-\theta_1)e^{2\alpha\theta_1}g(-t+\theta_1))\Big) \\ \approx e^{-2\alpha T}e^{2\alpha\theta_1}\ \kappa_2(\theta_1-t)\ \rho(t-\theta_1), \end{aligned} \qquad \text{(F.7)}$$

where $\kappa_2(\theta_1) = g(-\theta_1) \otimes_{\theta_1} g(\theta_1)$ when $\rho(t-\theta_1)$ falls within the window $W(T-t)$ and 0 when it is outside of the window. If the amplitude of the envelope of $\kappa_2(\theta_1)$ (and correspondingly $g(\theta_1)$) is approximately constant over the duration of $\rho(\theta_1)$, then $\kappa_2(\theta_1-t)\cdot\rho(t-\theta_1) \approx \kappa_2(0)\cdot\rho(t-\theta_1)$. Assuming that $\rho(t-\theta_1)$ is within the

window:

$$\begin{aligned}
\mathrm{VAR}_{incoherent} &\approx \frac{1}{M^2} \cdot \int_{\theta_1=-\infty}^{\infty} W(T-\theta_1)\sigma(t-\theta_1)\times \\
&\qquad \left[\sigma(t) \otimes_t \left(e^{-2\alpha T} e^{2\alpha\theta_1}\ \kappa_2(0)\ \rho(t-\theta_1)\right)\right]\ d\theta_1 \\
&= \frac{1}{M^2} \cdot \int_{\theta_1=-\infty}^{\infty} W(T-\theta_1)\sigma(t-\theta_1)\times \\
&\qquad \kappa_2(0)\ e^{-2\alpha T} e^{2\alpha\theta_1}\left[\sigma(t) \otimes_t \rho(t-\theta_1)\right]\ d\theta_1 \\
&= \frac{1}{M^2} \cdot \int_{\theta_1=-\infty}^{\infty} \kappa_2(0)\ e^{-2\alpha T} e^{2\alpha\theta_1} W(T-\theta_1)\sigma(t-\theta_1)\sigma(t-\theta_1)\ d\theta_1
\end{aligned} \tag{F.8}$$

$$\approx \frac{1}{M^2} \cdot \kappa_2(0)\ e^{-2\alpha T} e^{-2\alpha t} \int_{\theta_1=T-t_{off}}^{T-t_{on}} u(t-\theta_1) e^{4\alpha\theta_1}\ d\theta_1. \tag{F.9}$$

As before, the Heaviside function can be used to limit the bounds of the integral. This must be done in a piecewise manner to account for $t \leq T - t_{on}$ and $t \geq T - t_{on}$.

$$\mathrm{VAR}_{incoherent} \approx \quad \frac{\kappa_2(0)}{4\alpha M^2} e^{2\alpha(T-2t_{on}-t)} \begin{cases} (e^{-4\alpha(T-t_{on}-t)} - e^{-4\alpha\Delta t}) & \text{if } t < T - t_{on} \\ (1 - e^{-4\alpha\Delta t}) & \text{if } t \geq T - t_{on} \end{cases} \tag{F.10}$$

If the duration of $g(t)$ had not been short relative to α, eqn. F.6 would change to:

$$g(-\theta_1) \otimes_{\theta_1} (u(T-\theta_1) e^{2\alpha\theta_1} g(-t+\theta_1)) \approx \Big(g(-\theta_1) \otimes_{\theta_1} (e^{2\alpha\theta_1} g(-t+\theta_1))\Big). \tag{F.11}$$

The impact of this would be to redefine κ_2, thus changing the amplitude of $\kappa_2(0)$. Again, this only changes the quantitative result for the incoherent variance. The qualitative trend does not change for moderately long input pulses.